Chapter 2 Radiative Processes and Remote Sounding

2.1. Introduction

In any planetary atmosphere, the character of the circulation depends strongly on the magnitude and distribution of the net diabatic heating rate. In the earth's troposphere, the net diabatic heating rate is dominated by the imbalance between two large terms: transfer of heat from the surface, and thermal emission of radiation to space. Latent heat is a major component of the flux from the surface to the atmosphere, and clouds play a major role in the emission of radiation to space.

From the tropopause to the mesopause, the situation is much simpler. Net heating depends almost exclusively on the imbalance between local absorption of solar ultraviolet radiation and infrared radiative loss. In this region, ozone is the dominant absorber and carbon dioxide is the dominant emitter. Infrared emission by ozone and water vapor and solar absorption by water vapor, molecular oxygen, carbon dioxide, and nitrogen dioxide play secondary roles (Fig. 2.1). The distribution of the radiative sources and sinks due to these gases exerts a zero-order control on the large-scale seasonally varying mean temperature and zonal wind fields of the middle atmosphere. Infrared radiative emission also provides an important mechanism for damping dynamically forced temperature variations. These radiative processes will be described in this chapter.

Satellite observations of emitted, transmitted, and scattered radiation can be used to diagnose the global distributions of temperature and constituent concentrations throughout the middle atmosphere. Such observations have provided much of the basic data bearing on the dynamical state and transport processes in this region. Principles and applications of these

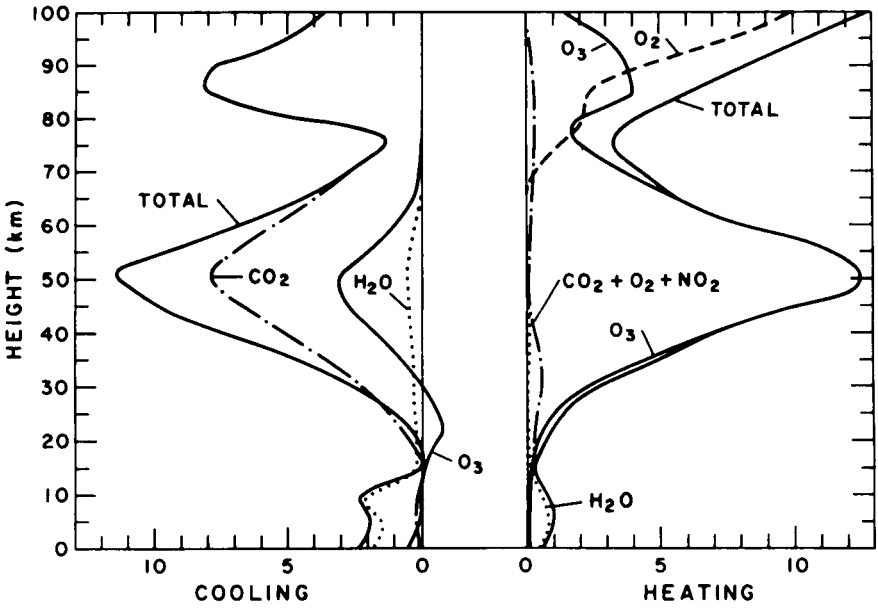

Fig. 2.1. Vertical distribution of heating due to absorption of solar radiation (right) and cooling due to emission of infrared radiation (left). [From London (1980), with permission.]

techniques to the middle atmosphere are considered in the last section of this chapter. In the future, satellite measurements of emitted radiance should also be useful for the direct determination of wind velocities.

2.2 Fundamentals

Calculation of the distribution of radiative sources and sinks requires the solution of the radiative transfer problem. This is essentially a problem of careful bookkeeping. The physics enters with the consideration of the actual processes of interaction between radiation and matter. In this section, the concepts and basic formalism of radiative transfer theory are introduced.

2.2.1 Radiative Transfer Quantities and the Equation of Transfer

Figure 2.2 illustrates the geometry of electromagnetic radiation crossing a plane surface S whose unit normal vector is $\hat{\mathbf{n}}$. Radiant energy flux contained in a conical bundle of infinitesimal solid angle $d\Omega$ in the direction of unit vector $\hat{\mathbf{\Omega}}$ is shown. The flux of energy per unit area of S in the

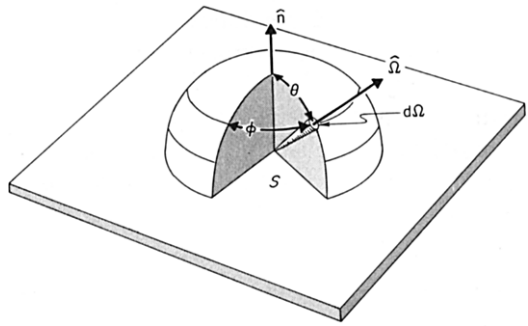

Fig. 2.2. Geometry of radiation crossing a plane surface S with unit normal $\hat{n}$. Radiance in the solid angle cone $d\Omega$ in the direction $\hat{\mathbf{\Omega}}$ is described in terms of the spherical coordinates θ and ϕ.

bundle is $L(\hat{\mathbf{\Omega}})\, d\Omega$, where $L(\hat{\mathbf{\Omega}})$, the *radiance*, is the fundamental radiative transfer quantity. Its units are $\mathrm{W\,m^{-2}\,sr^{-1}}$.

The contribution of the radiant flux in this bundle to the total flux across S in the direction of $\hat{\mathbf{n}}$ is $(\hat{\mathbf{n}} \cdot \hat{\mathbf{\Omega}}) L(\hat{\mathbf{\Omega}})\, d\Omega$, and the total flux across S into the half-space above S (2π steradians) is the *flux density* F, given by

$$F = \int_{2\pi} (\hat{\mathbf{n}} \cdot \hat{\mathbf{\Omega}}) L(\hat{\mathbf{\Omega}})\, d\Omega = \int_0^{2\pi} \int_0^{\pi/2} L(\phi, \theta) \cos\theta \sin\theta\, d\theta\, d\phi, \tag{2.2.1}$$

as expressed in terms of the azimuth and zenith angles ϕ and θ (see Fig. 2.2). Radiant energy impinging on S is called *irradiance*, while radiant energy emitted from S is called *emittance*. In this chapter this distinction will generally be avoided, and either quantity will be referred to as flux density. Units of F are $\mathrm{W\,m^{-2}}$.

The *net flux* F_n is the difference between flux density crossing S in the direction $\hat{\mathbf{n}}$ and that crossing in the opposite direction, $-\hat{\mathbf{n}}$. For example, if S is horizontal,

$$F_n = F_\uparrow - F_\downarrow \tag{2.2.2}$$

where $F_\uparrow$ and $F_\downarrow$ are flux densities in the upward and downward directions. For a Cartesian coordinate system, three values of F_n correspond to net flux values across the three coordinate planes of that system. These are the components in those coordinates of a vector, the *net flux vector* $\mathbf{F_n}$.

Because of the spectral dependences of radiation and its interaction with matter, it is necessary to consider *monochromatic* radiance and flux density. Spectral dependence is expressed in terms of frequency ν, wavelength λ,

or wave number λ^{-1}. Spectral dependence in the microwave is usually expressed in terms of frequency (Hz), while at infrared, visible, and ultraviolet wavelengths it is usually expressed in terms of wavelength (cm or nm) or wave number (cm^{-1}). In the following development we shall use frequency exclusively, but monochromatic quantities can be easily expressed in terms of any of the spectral variables with the aid of the speed of light c, where

$$c = \nu\lambda \doteq 3 \times 10^8 \text{ m s}^{-1}. \tag{2.2.3}$$

Monochromatic radiance L_ν and monochromatic flux density F_ν are given by

$$L_\nu = \frac{dL}{d\nu}, \qquad F_\nu = \frac{dF}{d\nu}. \tag{2.2.4}$$

Units of L_ν are $\text{W m}^{-2}\,\text{sr}^{-1}\,(\text{s}^{-1})^{-1}$ and units of F_ν are $\text{W m}^{-2}\,(\text{s}^{-1})^{-1}$.

The rate of decrease (extinction) or increase of monochromatic radiance along a length element ds in the direction $\hat{\boldsymbol{\Omega}}$ is linear in the amount of absorbing matter. Extinction is also linear in the monochromatic radiance. These facts are expressed in the *radiative transfer equation*

$$\frac{dL_\nu(\hat{\boldsymbol{\Omega}})}{ds} = -k_\nu \rho_a [L_\nu(\hat{\boldsymbol{\Omega}}) - J_\nu(\hat{\boldsymbol{\Omega}})]. \tag{2.2.5}$$

The density of the radiatively active gas ρ_a and two quantities k_ν and J_ν appear in this equation. These quantities characterize the interaction between radiation and matter. They depend on the local properties of the medium. The *extinction coefficient* k_ν, whose units are $\text{m}^2\,\text{kg}^{-1}$, describes the extinction of L_ν along ds, while the *source function* J_ν describes the rate of increase.

Energy removed from L_ν by extinction can either increase the internal energy of matter at the point of extinction or can be immediately scattered at some angle to the incident beam, thereby providing an input to monochromatic radiance at the same frequency in a different direction. Thus k_ν can be expressed as the sum of an *absorption coefficient* a_ν and a *scattering coefficient* s_ν,

$$k_\nu = a_\nu + s_\nu. \tag{2.2.6}$$

The ratio of scattered energy to total energy lost by extinction at a point in the medium is the *single scattering albedo* $\bar{\omega}_\nu$,

$$\bar{\omega}_\nu \equiv s_\nu / k_\nu, \qquad (1 - \bar{\omega}_\nu) \equiv a_\nu / k_\nu. \tag{2.2.7}$$

Scattering contributes to emission of radiation in the direction of the scattered photons, and thereby contributes to the source function. The total

scattering contribution to the source function from a volume element in the direction $\hat{\Omega}$, $J_{\nu,s}(\hat{\Omega})$, is an integral over all incident angles $\hat{\Omega}'$ filling 4π steradians,

$$J_{\nu,s}(\hat{\Omega}) = \frac{\bar{\omega}_\nu}{4\pi} \int_{4\pi} L_\nu(\hat{\Omega}') P_\nu(\hat{\Omega}, \hat{\Omega}')\, d\Omega'. \tag{2.2.8}$$

The function $P_\nu(\hat{\Omega}, \hat{\Omega}')$ describes the angular distribution of the scattered radiation and also depends on the local properties of matter as well as the frequency; $P_\nu(\hat{\Omega}, \hat{\Omega}')$ is the *phase function*, and according to Eq. (2.2.8), it is normalized such that

$$\frac{1}{4\pi} \int_{4\pi} P_\nu(\hat{\Omega}, \hat{\Omega}')\, d\Omega' = 1. \tag{2.2.9}$$

By itself, scattering does not change the internal energy of matter, but emission of radiation can also take place at the expense of the internal energy of the matter in a volume element. In order to describe this *thermal emission* it is necessary to distinguish between *local thermodynamic equilibrium* (*LTE*), the condition under which *Kirchhoff's Law* applies, and the condition under which Kirchhoff's Law fails (*non-LTE*). For the most important radiatively active gases, LTE holds for pressures greater than about 0.1 mb but begins to fail at lower pressures.

Under LTE conditions with no scattering ($\bar{\omega}_\nu = 0$), Kirchhoff's Law states that the source function is equal to the *Planck function* B_ν,

$$J_\nu = B_\nu(T) = \frac{2h\nu^3}{c^2} (e^{h\nu/k_b T} - 1)^{-1}, \tag{2.2.10}$$

where h and k_b are the Planck and Boltzmann constants. Note that B_ν is independent of direction; that is, it is *isotropic*. The integral of B_ν over all frequencies is the *blackbody radiance* $B(T)$,

$$B(T) = \int_0^\infty B_\nu(T)\, d\nu = \frac{\sigma}{\pi} T^4, \tag{2.2.11}$$

where $\sigma = 5.67 \times 10^{-8}\ \mathrm{W\,m^{-2}\,K^{-4}}$, the Stefan–Boltzmann constant.

When LTE holds but scattering occurs ($\bar{\omega}_\nu \neq 0$), Kirchhoff's Law takes the more general form

$$J_\nu(\hat{\Omega}) = (1 - \bar{\omega}_\nu) B_\nu + \frac{\bar{\omega}_\nu}{4\pi} \int_{4\pi} L_\nu(\hat{\Omega}') P_\nu(\hat{\Omega}, \hat{\Omega}')\, d\Omega'. \tag{2.2.12}$$

The source function for non-LTE conditions will be discussed in Section 2.6.

There is a useful integral form of the radiative transfer equation. As illustrated in Fig. 2.3, radiance at a position s along a path in the direction

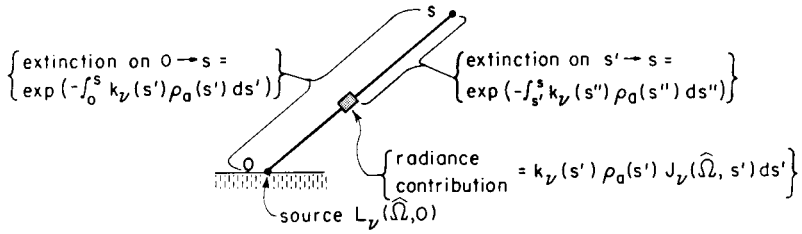

Fig. 2.3. Contributions to radiance at s from the path 0 to s.

of $\hat{\mathbf{\Omega}}$ is given by

$$L_\nu(\hat{\mathbf{\Omega}}, s) = L_\nu(\hat{\mathbf{\Omega}}, 0) \exp\left[-\int_0^s k_\nu(s')\rho_a(s')\, ds'\right] + \int_0^s k_\nu(s')\rho_a(s')J_\nu(\hat{\mathbf{\Omega}}, s') \exp\left[-\int_{s'}^s k_\nu(s'')\rho_a(s'')\, ds''\right] ds'. \tag{2.2.13}$$

The quantity $\int_{s'}^s k_\nu(s'')\rho_a(s'')\, ds''$ is called the *optical path* between s' and s. Equation (2.2.13) is the formal solution of the radiative transfer equation, Eq. (2.2.5). In accordance with the linear character of the problem, it expresses the fact that radiance $L_\nu(\hat{\mathbf{\Omega}}, s)$ is composed of contributions from boundary radiance $L_\nu(\hat{\mathbf{\Omega}}, 0)$ exponentially attenuated by the optical path length between 0 and s plus infinitesimal radiance contributions from volume elements at positions s' along the path, given by

$$k_\nu(s')\rho_a(s')J_\nu(\hat{\mathbf{\Omega}}, s')\, ds'.$$

Each such contribution is attenuated exponentially by the matter contributing to the optical path between s' and s, and these contributions are integrated along the path.

2.2.2 *Plane-Parallel Atmosphere Approximation*

In atmospheric radiative transfer theory, two approximations are usually made. (1) The curvature of level surfaces due to the sphericity of the planet is negligible. (2) Properties of the medium and the radiation field depend only on the vertical coordinate. Together, these conditions comprise the *plane-parallel atmosphere approximation.*

When the plane-parallel atmosphere approximation holds, the net flux vector is vertical and it is appropriate to express the angular dependence of the radiation field in terms of polar coordinates (θ, ϕ) referenced to the

local vertical so that θ is the *zenith angle* (measured from the vertical). Moreover, radiance is independent of azimuth ϕ. It follows from Eq. (2.2.1) that flux density in the upward direction is given by

$$F_{\uparrow}(z^*) = 2\pi \int_0^{\pi/2} L(\theta, z^*) \cos\theta \sin\theta \, d\theta = 2\pi \int_0^1 L(\mu, z^*)\mu \, d\mu, \tag{2.2.14a}$$

where $\mu \equiv \cos\theta$.

Flux density in the downward direction is given by

$$F_{\downarrow}(z^*) = 2\pi \int_{\pi}^{\pi/2} L(\theta, z^*) \cos\theta \sin\theta \, d\theta = 2\pi \int_0^1 L(-\mu, z^*)\mu \, d\mu. \tag{2.2.14b}$$

Note the use of the argument $-\mu$ to indicate downward radiance.

For plane-parallel atmosphere problems involving monochromatic radiation, the vertical coordinate z^* can be replaced by the *optical depth* $\tau_\nu(z^*)$. This is the optical path along the vertical between height z^* and the top of the atmosphere,

$$\tau_\nu(z^*) = \int_{z^*}^{\infty} k_\nu(z^{*\prime})\rho_a(z^{*\prime}) \, dz^{*\prime}. \tag{2.2.15a}$$

The notation τ_ν with subscript ν explicitly denotes the frequency dependence of the optical depth, which arises from the frequency dependence of k_ν. Optical depth can also be expressed in terms of the log-pressure vertical coordinate z:

$$\tau_\nu(z) = \int_z^{\infty} k_\nu(z')\rho_{a0}(z') \, dz' \tag{2.2.15b}$$

where $\rho_{a0}(z) = \rho_a(z)[T(z)/T_s] = \rho_a(z)[\rho_0(z)/\rho(z)]$ is the basic absorber density scaled to the reference temperature T_s used to define the reference scale height H [see Eq. (1.1.8)]. Note that $\rho_{a0}(z) = m_a(z)\rho_0(z)$, where m_a is the mass mixing ratio of the absorbing gas and $\rho_0(z) = \rho_s e^{-z/H}$ is the basic density in the log-pressure coordinate system, as defined in Section 3.1.1.

Solar radiation in a plane-parallel atmosphere is conveniently separated into radiation in the solar beam, *direct solar radiation*, and radiation scattered by the atmosphere, *diffuse solar radiation*. Direct solar radiation consists of a very large radiance in a very small solid angle. Outside the atmosphere on a surface normal to the direction of the solar radiation stream $\hat{\mathbf{\Omega}}_0$, direct solar radiation contains a monochromatic flux density $S_{0\nu}$. The spectral integral of $S_{0\nu}$ is usually referred to as the *solar constant* S_0, although this

term is inappropriate since S_0 is known to exhibit some variability in time. At level z within the atmosphere, the monochromatic flux of direct solar radiation across a level surface and incident at zenith angle $\theta_0 = \cos^{-1} \mu_0$ is

$$S_\nu(z) = \mu_0 S_{0\nu} e^{-\tau_\nu(z)/\mu_0}. \tag{2.2.16}$$

The source function given by Eq. (2.2.12) can be rewritten to explicitly display the contributions to scattered radiance by the direct solar radiation and the diffuse radiation. The angular dependence of the direct solar radiation can be approximated by a delta function, and it follows from Eq. (2.2.16) that

$$J_\nu(\hat{\mathbf{\Omega}}) = (1 - \bar{\omega}_\nu) B_\nu + \frac{\bar{\omega}_\nu}{4\pi} \int_{4\pi} L_\nu(\hat{\mathbf{\Omega}}') P_\nu(\hat{\mathbf{\Omega}}, \hat{\mathbf{\Omega}}')\, d\Omega'$$

$$+ \frac{\bar{\omega}_\nu S_{0\nu}}{4\pi} P_\nu(\hat{\mathbf{\Omega}}, \hat{\mathbf{\Omega}}_0) e^{-\tau_\nu/\mu_0}. \tag{2.2.17}$$

In Eq. (2.2.17), $L_\nu(\hat{\mathbf{\Omega}}')$ corresponds to diffuse radiance alone, and $J_\nu(\hat{\mathbf{\Omega}})$ contributes only to diffuse radiance. In most applications, spectral overlap between solar and thermal radiation can be neglected so the first term on the right side of Eq. (2.2.17) can be ignored at wavelengths shorter than about 4 μm while the last term can be neglected at longer wavelengths.

The formal solution to the problem of determining the diffuse monochromatic radiance in a plane parallel atmosphere can now be stated with the aid of the integral form of the radiative transfer equation [Eq. (2.2.13)] and suitable boundary conditions at the bottom and top of the atmosphere. In terms of optical depth, radiance in the upward direction is

$$L_\nu[\mu, \tau_\nu(z)] = L_\nu[\mu, \tau_\nu(0)] \exp\{-\mu^{-1}[\tau_\nu(0) - \tau_\nu(z)]\}$$

$$+ \int_{\tau_\nu(z)}^{\tau_\nu(0)} \mu^{-1} J_\nu[\mu, \tau_\nu(z')] \exp\{-\mu^{-1}[\tau_\nu(z') - \tau_\nu(z)]\}\, d\tau_\nu(z'). \tag{2.2.18}$$

The radiance at the lower boundary $L_\nu[\mu, \tau_\nu(0)]$ depends on the monochromatic *emissivity* ε_ν of the surface, which is the ratio of the radiance emitted at the expense of the internal energy of the boundary to that of a blackbody at the same temperature. According to Kirchhoff's Law, the monochromatic reflectivity of an opaque surface is $(1 - \varepsilon_\nu)$. For an isotropically reflecting surface it follows that the boundary radiance $L_\nu[\mu, \tau_\nu(0)]$ required for Eq. (2.2.18) is the isotropic radiance

$$L_\nu[\tau_\nu(0)] = \varepsilon_\nu B_\nu[\tau_\nu(0)] + (1 - \varepsilon_\nu) \bar{L}_\nu[-\mu, \tau_\nu(0)]$$

$$+ (1 - \varepsilon_\nu) \mu_0 S_{0\nu} e^{-\mu_0^{-1} \tau_\nu(0)}, \tag{2.2.19}$$

where $\bar{L}_\nu[-\mu, \tau_\nu(0)] \equiv 2\int_0^1 L_\nu[-\mu, \tau_\nu(0)]\mu\, d\mu$ is the angular mean of L_ν. For thick clouds and most surface materials, $\varepsilon_\nu \approx 1$ at thermal infrared wavelengths ($\lambda \gtrsim 4\ \mu$m), and the reflected contributions can often be neglected. Moreover, as in Eq. (2.2.17), B_ν can be neglected for $\lambda \lesssim 4\ \mu$m while $S_{0\nu}$ can be neglected for $\lambda \gtrsim 4\ \mu$m. At visible as well as infrared wavelengths it is often assumed that ε_ν is isotropic, but this assumption can lead to serious errors for near-infrared and visible wavelengths over some surfaces, particularly at low sun angles.

The upper boundary condition for diffuse radiation is

$$L_\nu(-\mu, \tau_\nu = 0) = 0, \tag{2.2.20}$$

so that the radiative equation for downward radiance is simply

$$L_\nu[-\mu, \tau_\nu(z)] = \int_0^{\tau_\nu(z)} \mu^{-1} J_\nu[-\mu, \tau_\nu(z')] \times \exp\{-\mu^{-1}[\tau_\nu(z) - \tau_\nu(z')]\}\, d\tau_\nu(z'). \tag{2.2.21}$$

2.2.3. *Effect of Atmospheric Sphericity*

In contrast to the troposphere, where horizontal inhomogeneities are often very large, the conditions for validity of the plane-parallel atmosphere approximation are generally well satisfied in the middle atmosphere except for direct solar radiation at large zenith angles ($\theta \gtrsim 80°$). At these large solar zenith angles, a correction must be applied to the expression for the direct solar radiation [Eq. (2.2.16)] to account for the sphericity of level surfaces.

Because the atmosphere is spherical, μ_0 varies along the path. The geometry is depicted in Fig. 2.4 for paths for which $\theta(z^*) < \pi/2$ and $\theta(z^*) > \pi/2$. In the former case, τ_ν in Eq. (2.2.15a) should be replaced by $\tau_{\nu,\mathrm{cor}}$:

$$\tau_{\nu,\mathrm{cor}}(z^*) = \mu_0(z^*) \int_{z^*}^{\infty} k_\nu(z^{*\prime})\rho_a(z^{*\prime})\, dz^{*\prime}/\mu_0(z^{*\prime}), \tag{2.2.22}$$

where $\mu_0(z^{*\prime})$ varies along the path as indicated in Fig. 2.4. Because of the sphericity, solar radiation can reach the upper atmosphere when $\theta(z^*) > \pi/2$ provided that $\theta(z^*) < \theta_{\mathrm{cutoff}}(z^*)$, and a straightforward modification of Eq. (2.2.22) is required in this case. Closed-form expressions employing tabulated functions known as *Chapman functions* can be used to evaluate the integrals in Eq. (2.2.22) in the special case of a constituent with a constant absorption coefficient whose density varies exponentially with height.

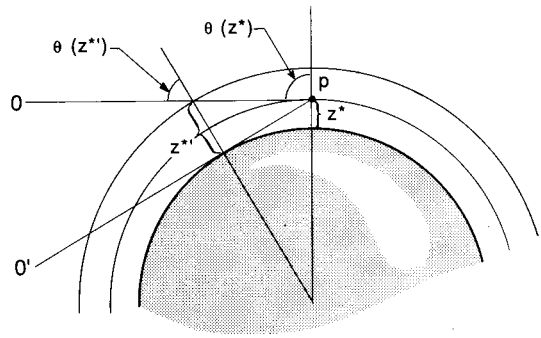

Fig. 2.4. Effect of spherical planetary shape on the geometry of direct solar radiation, shown with greatly exaggerated atmospheric thickness. Path $\overline{OP}$ corresponds to $\theta < \pi/2$; path $\overline{O'P}$ corresponds to $\theta > \pi/2$. In the latter case an observer at P sees the sun below the horizontal. The angle $\theta_{\text{cutoff}}(z^*)$ is the zenith angle at which $\overline{O'P}$ just intersects the horizon.

2.3 Gaseous Absorption Spectra

Solar photons are absorbed in the stratosphere and mesosphere primarily at ultraviolet wavelengths (0.1–0.4 μm) and to a lesser extent at visible (0.4–0.7 μm), near-infrared (0.7–4 μm), and X-ray wavelengths. The absorbed energy produces electronic, vibrational and rotational excitation, molecular dissociation, and ionization, but the energy used for ionization is of only minor importance for the total energy budget of the middle atmosphere. At altitudes below about 60 km, these processes are closely balanced by local recombination and collisional deexcitation so that most of the absorbed energy is *thermalized*—that is, it is realized locally as heat. In contrast, molecular collisions in the thermosphere and to some extent in the upper mesosphere are too infrequent to insure local thermalization of all absorbed energy (see Section 2.6). Dissociation and ionization occur primarily in continuous spectra, but excitation of electronic, vibrational, and rotational energy takes place in spectrally complex bands composed of large numbers of lines. In some cases, dissociation or ionization can also arise from absorption in complex spectral bands provided these are at wavelengths shorter than the threshold wavelength for dissociation or ionization.

Molecular absorption of thermal infrared radiation at wavelengths between 4 and 17 μm excites vibrational and rotational energy, producing *vibration-rotation* bands, which invariably have a complex structure. Positions of some important vibration-rotation bands are shown in Fig. 2.5. At wavelengths longer than 17 μm, absorption arises predominantly from transitions in molecular rotational energy, producing rotational lines and bands. In order to calculate diabatic heating rates, it is necessary to know

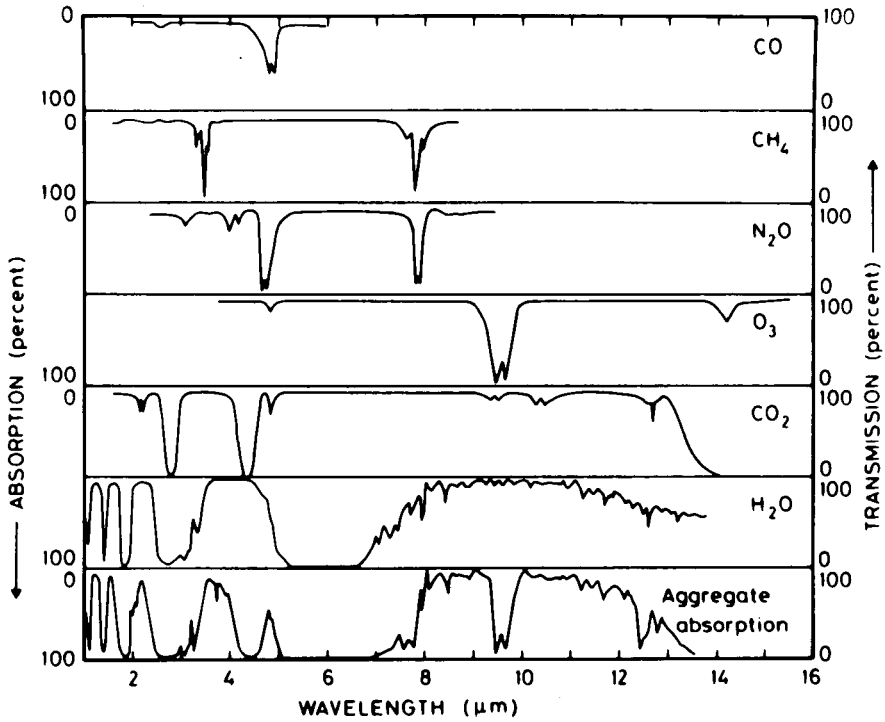

Fig. 2.5. Schematic spectra depicting the most important gaseous absorption features for infrared radiative transfer in the middle atmosphere. Absorptions correspond approximately to a normal incidence path through the atmosphere. [From Handbook of Geophysics and Space Environment, Air Force Cambridge Research Laboratory (1965), with permission.]

the strength, shape, and positions of the spectral lines responsible for absorption. The processes controlling these spectral characteristics are described here.

2.3.1 Molecular Energy Levels and Transitions: The Spectrum of O_2

Although many of the molecules of interest are polyatomic, the most important characteristics of molecular spectra can be illustrated by considering the simpler properties of diatomic molecules. Figure 2.6 is a schematic potential energy diagram of a diatomic molecule, AB. The potential energy versus internuclear distance is shown for the ground electronic state (X) and the first electronically excited state (A). For each of these states, potential energy first decreases and then increases with internuclear distance, corresponding to electrical forces that are repulsive at close range and attractive at longer range on either side of a stable equilibrium point.

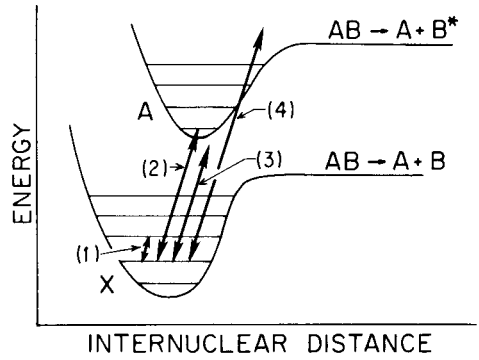

Fig. 2.6. Schematic potential energy diagram for a diatomic molecule showing four types of transitions.

At large separations, potential energy becomes independent of distance. The dissociation threshold for the X state corresponds to dissociation into two ground-state atoms, while the threshold for the A state corresponds to dissociation into one or more electronically excited atoms. The horizontal lines represent the vibrational energy levels or substates of each electronic state. As these energy levels increase, the vibrational oscillation energies increase until the dissociation threshold is reached.

The transitions indicated by the slanting arrows in Fig. 2.6 represent (1) absorption of a photon to produce a transition from the second to the third vibrational energy level of the X state,[1] (2) absorption producing a transition from the second vibrational energy level of the X state to the first level of the A state, (3) absorption producing photodissociation to two ground-state atoms, and (4) dissociation producing one excited state and one ground state atom. Note that the energy changes associated with the dissociations are continuous; in contrast, the discrete energy changes associated with transitions between vibrational energy levels produce discrete spectral bands.

The vibrational energy levels in turn contain further internal structure: each is divided into a number of rotational energy levels whose spacing is too small to be shown in Fig. 2.6. Hence, transitions such as (1) or (2) are multiple and are associated with a series of spectral lines.

These relationships between the energy levels and spectra are illustrated in Fig. 2.7, which shows the potential energy diagram and the ultraviolet absorption spectrum of O_2. These O_2 spectral features are important for the energetics of the mesosphere and for photochemistry in both stratosphere and mesosphere. The ordinate in Fig. 2.7b is the *cross section* σ_ν, which is

[1] For molecules with identical nuclei, like O_2 and N_2, photon absorption does not occur for this type of transition.

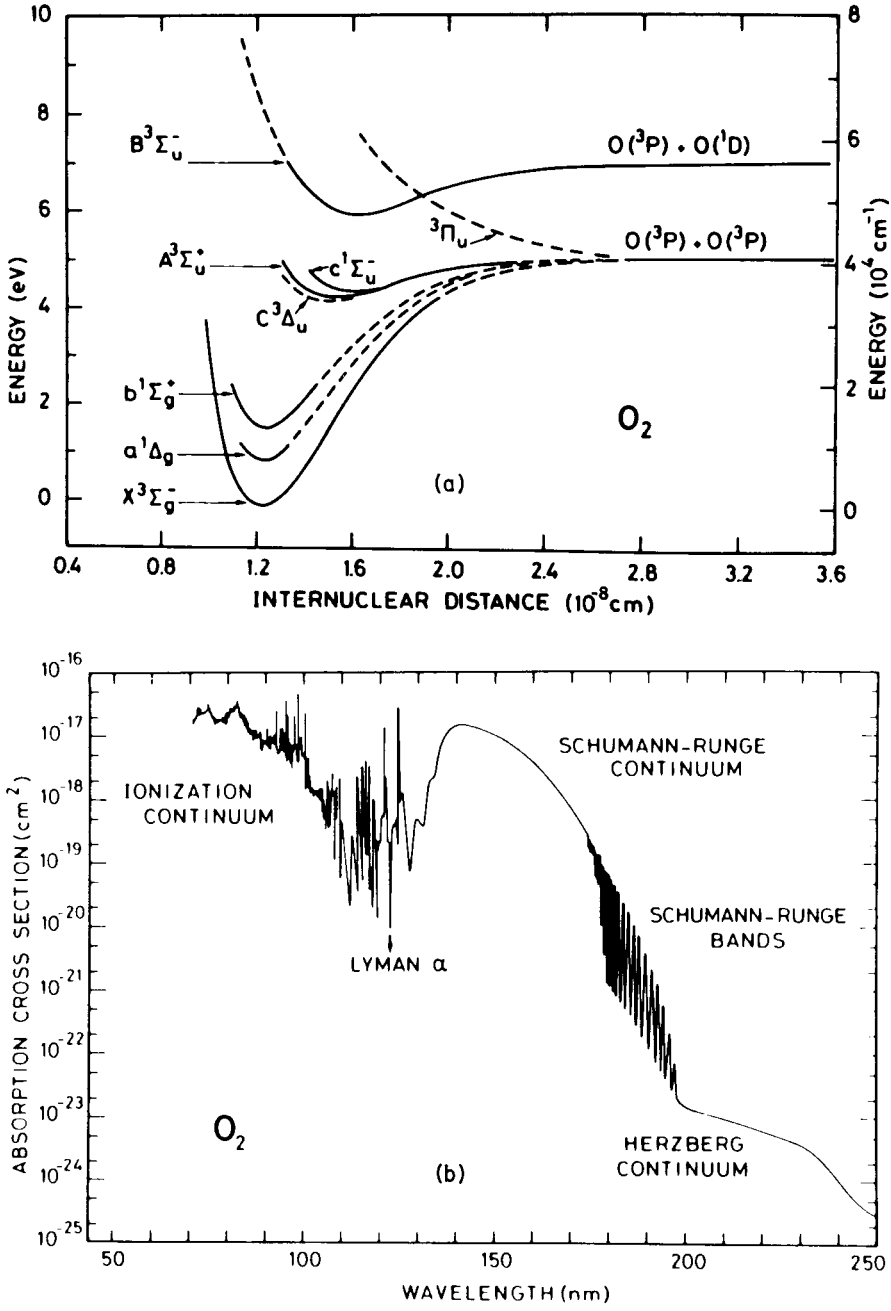

Fig. 2.7. (a) Simplified potential-energy diagram for O_2. [From Gilmore (1964), with permission.] (b) Ultraviolet spectrum of O_2. [From Brasseur and Solomon (1984). Copyright © 1984 by D. Reidel Company, Dordrecht, Holland.]

related to the absorption coefficient by

$$\sigma_\nu = M_a a_\nu \tag{2.3.1}$$

where M_a is the mass of the absorbing molecule. In Fig. 2.7a the potential-energy curves for the electronic energy levels of O_2 are shown, together with their *term symbols.* Vibrational as well as rotational levels are omitted for clarity. The term symbol specifies the electronic configuration and indicates the ordinal number of the level or *term* in a series of terms having the same *multiplicity* (series X, A, B, ..., or series X, a, b, ...). The multiplicity, indicated by the superscript preceding the Greek letter, is determined by the net electronic spin with integer quantum number S. It is $(2S + 1)$, the number of substates distinguished by different spin orientations.

The Greek letter in the term symbol corresponds to the net orbital angular momentum quantum number in the sequence $\Sigma, \Pi, \Delta, \ldots$, analogous to atomic orbital angular momentum quantum number symbols S, P, D, ... The subscripts and superscripts that follow indicate terms whose wave functions are symmetric or antisymmetric upon reflection (+, −), or have even parity (g) or odd parity (u).

Term symbols provide more than convenient shorthand labels for the terms: they also display information on *allowed* and *forbidden* transitions. Allowed transitions can occur if there is a change of the dipole moment between the two participating terms. Such *electronic dipole transitions* have relatively large cross sections. In addition, other types of change in the electronic configuration of the molecule can be associated with absorption or emission of radiation, for example, *electronic quadrupole* or *magnetic dipole* changes. However, cross sections for such transitions are typically smaller than electronic dipole transitions by six orders of magnitude or more. Such transitions are included in the category of forbidden transitions.

Selection rules, derived from the quantum-mechanical theory of the terms, distinguish between allowed and forbidden transitions. Examples of selection rules are: spin change in a transition is forbidden; total angular momentum quantum number changes other than $0, \pm 1$ are forbidden. A more detailed discussion of term symbols and selection rules can be found in Brasseur and Solomon (1984).

The forbidden transition $X\,^3\Sigma_g^- \rightarrow A\,^3\Sigma_u^+$ produces very weak absorption bands between 260 and 242 nm. Dissociation to two ground-state oxygen atoms ($O\,^3P$) takes place at 242 nm (corresponding to an energy of 8.99×10^{-19} J or 5.58 eV). At this wavelength, the bands terminate in a weak continuum, which extends to still shorter wavelengths. These features comprise the *Herzberg bands* and *continuum.*

The allowed transition $X\,^3\Sigma_g^- \rightarrow B\,^3\Sigma_u^-$ is responsible for the strong bands between 200 and 175 nm, the *Schumann–Runge bands.* These bands termi-

nate in the *Schumann–Runge continuum*, which extends to shorter wavelengths and corresponds to the dissociation

$$O_2 \rightarrow O(^3P) + O(^1D)$$

in which one oxygen atom emerges in the excited ^1D state. Molecules in the upper term of the Schumann–Runge bands, the $B\,^3\Sigma_u^-$ state, can undergo a spontaneous transition to the $^3\Pi_u$ state, but the latter has no potential energy minimum so that it is unstable and rapidly dissociates to two oxygen atoms in the ^3P ground state. As a result of this process, known as *predissociation*, the lifetime of O_2 molecules in the $B\,^3\Sigma_u^-$ state is exceptionally short.

Figure 2.8 shows the detailed structure of the Schumann–Runge bands and illustrates the rotational line structure of the vibrational bands. The vibrational levels involved in the transitions are indicated in the figure. For example, 1–0 corresponds to rotational lines in the transition between the first excited vibrational level of the B state and the ground vibrational level of the X state. This important band system shows a high degree of regularity as well as complexity. The regular appearance of the system at longer wavelengths arises from the regularity of the spacing of vibrational and rotational energy levels. At the shorter wavelengths, the number of lines from incommensurably overlapping bands becomes so great that complexity appears to be winning out. Between 56,000 and 57,000 cm^{-1}, the spectrum has a disordered, almost random appearance.

2.3.2 Line and Band Strength

The *strength* S of a spectral line or band is defined as

$$S = \int \sigma_\nu \, d\nu \tag{2.3.2}$$

where the integration is over the entire line or band. The cross section σ_ν is usually expressed in the units cm^2, so that the corresponding units for S are $cm^2\,s^{-1}$. We turn now to a discussion of the factors controlling the strengths of lines and bands in a band system such as that shown in Fig. 2.8.

First, line or band strength for absorption is proportional to the ratio of the number density of molecules in the lower state of the transition, n_l, to the total number density of molecules of the absorbing gas, n_a. At thermodynamic equilibrium at temperature T, this ratio is given by the *Boltzmann factor*,

$$n_l / n_a = \frac{g_l \, e^{-E_l / k_b T}}{\sum_j g_j \, e^{-E_j / k_b T}}, \tag{2.3.3}$$

where E_l is the energy of level l and the summation is over all energy levels.

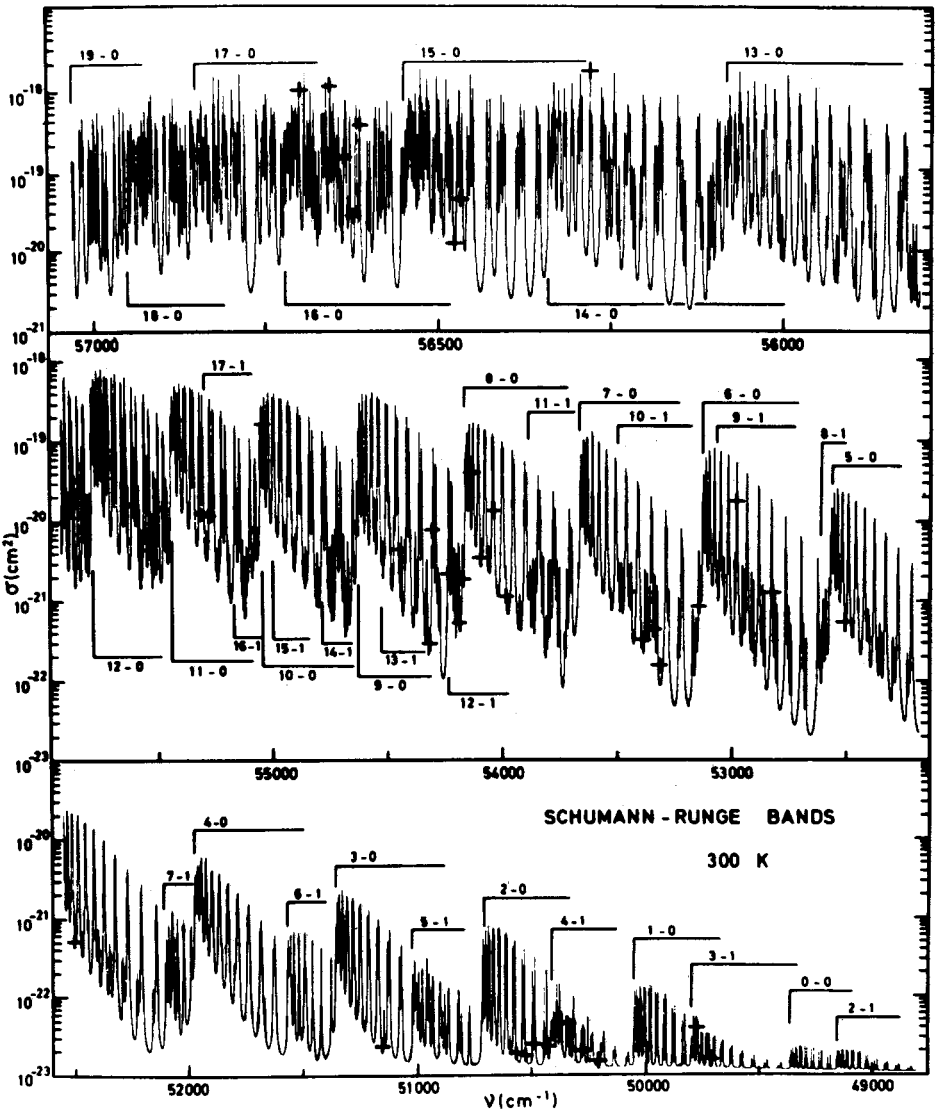

Fig. 2.8. Calculated spectrum of the Schumann–Runge band system shown with a few measured data points (+). [From Kockarts (1971). Copyright © 1971 by D. Reidel Publishing Company, Dordrecht, Holland.]

The integers g_l and g_j are *degeneracies*, the number of distinct states having energies E_l or E_j. For example, there are $2J + 1$ quantum-mechanically distinct orientations possible for a molecule whose angular momentum quantum number is J, and the corresponding degeneracy is $g_J = 2J + 1$. The denominator on the right side of Eq. (2.3.3) is the *partition function*, which gives the proper normalization, the summation over all states. It depends weakly on T, but not on the quantum numbers of energy level l.

The effect of the Boltzmann factor can be seen in the spectrum of Fig. 2.8 in two ways. First, within each vibrational band, the rotational quantum numbers of both the upper and lower states of each transition increase as the transitions progress from the strongest lines, near the short-wavelength edges of each band, toward weaker lines at longer wavelengths. Higher rotational quantum numbers for the lower states of each transition correspond to greater rotational energies of the lower state, and therefore, according to the Boltzmann distribution [Eq. (2.3.3)], to fewer molecules available for absorption. Second, vibrational bands corresponding to a transition whose lower state is an excited state have far fewer molecules available for absorption than bands corresponding to absorption from the ground vibrational level. Neglecting degeneracy , the ratio n_l/n_a is proportional to

$$e^{-E_l/k_b T} = e^{-h\nu_l/k_b T}$$

where $E_l = h\nu_l$ is the vibrational energy of the excited lower level. For typical vibrational transitions of diatomic molecules, the energy difference between adjacent vibrational levels gives $h\nu_l/k_b T \gtrsim 5$ at 273 K, so the number density ratios are typically $\lesssim 0.01$. Comparing representative bands with lower-state quantum numbers 0 and 1 in Fig. 2.8, for example the 2–0 and 2–1 bands, it can be seen that the strengths of corresponding lines within the two bands typically have ratios $\sim 100:1$, and this is primarily due to the differences in populations of the energy levels as expressed by the Boltzmann factors.

The important consequence of these population effects is that absorption band structure is strongly temperature dependent through the factor $h\nu_l/k_b T$. Because this factor is large for vibrational transitions, the relative strengths of bands with different lower-state vibrational quantum numbers are extremely sensitive to temperature. On the other hand, differences in energy between rotational levels are much smaller, so the temperature sensitivity of the ratios of line strengths within a band is much less, although the overall envelope of the rotational lines within a single vibrational band is controlled by temperature.

The changes in the electronic configuration of the molecule in vibrational transitions or in combined electronic and vibrational transitions also

influence the band strengths through a factor called the *oscillator strength*, which can be evaluated from calculations based on the quantum-mechanical description of the molecule. The relative oscillator strengths of vibrational bands within an electronic transition, such as the O_2 Schumann–Runge band system, are governed by the *Franck–Condon rule*, which states that the oscillator strength increases as the correspondence between the configurations of the upper and lower vibrational states increases. Together with the Boltzmann distribution, the oscillator strength controls the relative strengths of vibrational bands in a system such as the Schumann–Runge bands and is responsible for the general increase in strength toward shorter wavelengths shown in Fig. 2.8.

2.3.3 Line Shape and Line Width

Absorption lines have finite spectral width as a consequence of one or more of the following factors: finite lifetime Δt of the upper state, which leads to an uncertainty in the energy ΔE through the uncertainty principle

$$\Delta E\, \Delta t \geqq h/2\pi,$$

finite lifetime due to perturbation by molecular collisions, and Doppler frequency shifts due to relative thermal motions of the molecules. For a single line of strength S, the absorption cross section can be expressed in the form

$$\sigma_\nu = Sf(\nu - \nu_0) \tag{2.3.4}$$

where $f(\nu - \nu_0)$ is a shape factor giving the relative cross section at a point displaced by $(\nu - \nu_0)$ frequency units from the line center ν_0. The function $f(\nu - \nu_0)$ is normalized so that $\int_{-\infty}^{\infty} f(\nu - \nu_0)\, d\nu = 1$.

The simplest model for the effect of finite lifetime is the *Lorentz line shape*,

$$f(\nu - \nu_0) = (\alpha_L/\pi)[(\nu - \nu_0)^2 + \alpha_L^2]^{-1} \tag{2.3.5}$$

where $\alpha_L = (2\pi\bar{t})^{-1}$ and $\bar{t}$ is the mean time between major perturbations of the excited state. The frequency at which $|\nu - \nu_0| = \alpha_L$ is the half-power point for the line, and α_L is called the *Lorentz half-width.*

Line broadening produced by finite lifetime of the upper state is called *natural broadening.* In this case, $\bar{t}$ is proportional to the mean lifetime of the upper state, the inverse of the molecular emission probability. For the O_2 Schumann–Runge bands, the mean lifetime in the upper state for some vibrational bands is $\sim 10^{-9}$ s and the corresponding Lorentz half-width (in wave number units) is ~ 1 cm^{-1}. Natural broadening is a significant broadening mechanism for these bands in the mesosphere and upper stratosphere. In contrast, typical lifetimes for upper states of vibration–rotation transitions

in the infrared are ~0.1 s, and natural broadening is completely negligible compared with collisional broadening for these bands.

Broadening due to collisions, or *pressure broadening*, is a complex process, but it is usual to approximate each collision as an encounter that truncates the wave function corresponding to the state of the molecule by producing a large sudden phase shift. In this approximation, the "phase shift" approximation, the Lorentz line shape is a good approximation, with $\bar{t}$ the mean time between collisions. When typical kinetic theory values are used to represent molecular collisions,

$$\alpha_L \approx 0.07(p/p_s)(T_s/T)^{1/2} \quad \text{cm}^{-1}, \tag{2.3.6}$$

where $p_s = 1000$ mb and $T_s = 273$ K. At these reference pressure and temperature values, the Lorentz half-width usually falls in the range 0.05–0.11 cm^{-1}.

The Lorentz profile gives a good approximation to the shapes of pressure-broadened lines and is generally applicable at pressures typical of the middle stratosphere or greater, but there are some limitations. (1) There are significant variations in α_L from gas to gas, from band to band for the same gas, and in some cases even between rotational lines in the same band. Line width is also a function of the type of colliding molecule, or *broadening gas.* (2) Temperature dependence varies with the particular transition, but the actual temperature dependence is often stronger than that given by Eq. (2.3.6). The form $T^{-0.7}$ is more representative than $T^{-0.5}$. (3) Departures from the Lorentz shape occur at large distances from the line centers ($|\nu - \nu_0| \gg \alpha_L$). These extended wings can be important in the relatively transparent regions of the spectrum. Departures from the Lorentz shape in the extended wings are very difficult to measure and are a major source of uncertainty in atmospheric radiative transfer.

Even without pressure or natural broadening, finite line widths would arise because of molecular motion along the line of sight. This motion gives rise to the Doppler line shape

$$f(\nu - \nu_0) = (\pi\alpha_D)^{-1/2} \exp[-(\nu - \nu_0)^2/\alpha_D^2] \tag{2.3.7}$$

where

$$\alpha_D \equiv u_m \nu_0/c, \qquad u_m \equiv (2k_b T/M_a)^{1/2},$$

and M_a is the molecular mass. According to this definition, the spectral interval from line center to the half-power point (half-width) is $(\ln 2)^{1/2}\alpha_D$, not α_D.

When both Lorentz and Doppler broadening are important, the shape factor is given by the convolution integral of the Doppler and Lorentz

shapes:

$$f(\nu - \nu_0, \alpha_D, y) = \alpha_D^{-1} \pi^{-3/2} y \int_{-\infty}^{\infty} \frac{e^{-x^2}\, dx}{y^2 + [x - (\nu - \nu_0)/\alpha_D]^2} \quad (2.3.8)$$

where $y = \alpha_L/\alpha_D$, and $x = u/u_m$. This is the *Voigt line shape*, applicable when $\alpha_L \lesssim \alpha_D$. In particular, it is applicable to the Schumann-Runge bands in the upper stratosphere and mesosphere, since $\alpha_D \cong 6 \times 10^{-2}\ \text{cm}^{-1}$, comparable to the Lorentz half-width for natural broadening of some of the lines in these bands. For lines of vibration-rotation bands in the thermal infrared, $\alpha_D \approx 5 \times 10^{-4}\ \text{cm}^{-1}$, and it follows from Eq. (2.3.6) that the Doppler and pressure-broadened half-widths for lines in these bands become comparable at altitudes of 30–40 km.

Figure 2.9 compares Doppler and Lorentz profiles when the half-widths are equal. The Doppler profile is concentrated near the center but falls off rapidly in the wings, while the Lorentz profile has very broad wings. The Voigt profile resembles the Doppler profile near the line center and the Lorentz profile in the line wings. Because line wings are often of great importance in atmospheric radiative transfer, the effects of the Lorentz profile are often important well above the altitude at which the Doppler and pressure-broadened half-widths are equal. At these altitudes, the Doppler profile underestimates the absorption coefficient in the line wings, but the Lorentz profile underestimates the spectral width of the regions near

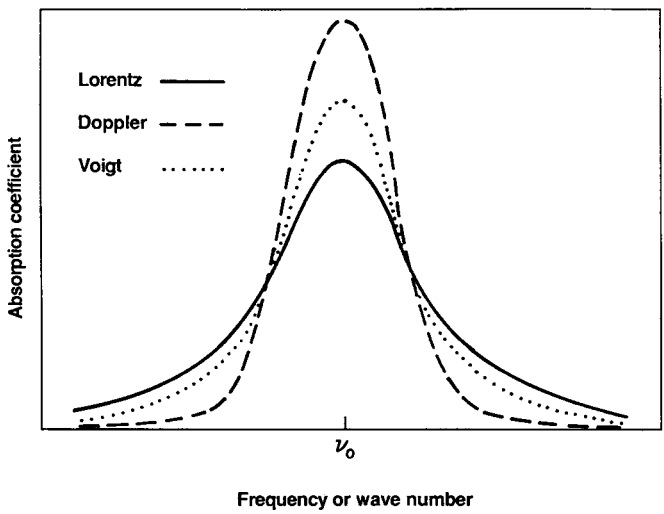

Fig. 2.9. Lorentz and Doppler line shapes for approximately equal half-widths and intensities. The corresponding Voigt profile is also shown.

the centers of strong absorption lines, since the Lorentz half-width continues to decrease with decreasing pressure.

Both the Doppler profile and the pressure-broadened Lorentz profile depend on temperature. However, the temperature dependence of line shape is usually of secondary importance compared with the temperature dependence of line and band strength.

2.3.4 Structure of Vibration-Rotation Bands

2.3.4.a Energy Levels

For a rigid rotating dipole, the energy levels E_J are given by

$$E_J \equiv BJ(J+1), \tag{2.3.9}$$

where B, the *rotational constant*, is inversely proportional to the moment of inertia of the dipole. The selection rule for a radiative transition is

$$\Delta J = \pm 1. \tag{2.3.10}$$

The absorption spectrum corresponds to $\Delta J = +1$ and has the following characteristics. There is an absorption line corresponding to the transition $J = 0 \rightarrow J = 1$ at frequency $\nu = 2B/h$ or wave number $2B/hc$. Another line corresponding to $J = 1 \rightarrow J = 2$ occurs at frequency $4B/h$, etc. Thus, a series of lines occurs with uniform frequency spacing $2B/h$. The relative strengths of these lines are approximately proportional to the Boltzmann factor with degeneracy $(2J + 1)$,

$$S(J) \approx (2J+1)e^{-BJ(J+1)/k_bT}. \tag{2.3.11}$$

The most important modifications to this simple model of a rigidly rotating dipole arise from the following factors:

1. *Nonrigidity of the oscillator.* At high rotation rates, the dipole separation and moment of inertia increase as a result of centrifugal stretching. The effect is to decrease line separations at large J values, and it may cause the progression of line positions with increasing J to reverse and produce a "band head," or sharp limit on the band.

2. *Complexity of the oscillator.* Linear molecules have a single moment of inertia and behave much like this simple model. For nonlinear molecules there are moments of inertia about two or three axes, and rotational energy levels must be described by two or three quantum numbers. This leads to a far more complicated spectrum such that the spacing of individual rotational lines associated with changes of all of the rotational quantum numbers may appear quite random.

Despite these complexities, typical rotational line spacings are of order $2B/hc$ in wave numbers, or 0.1–1 cm^{-1}. There is considerable variation between bands, however, and line spacings are generally smaller for heavier molecules.

Molecules with permanent electric dipole moments, such as H_2O and O_3, have strong pure rotation spectra. Linear symmetric molecules such as CO_2, O_2, and N_2 have no electric dipole moment in the ground vibrational state and hence no electronic dipole rotational spectra. O_2 and N_2 lack dipole moments even when vibrating; consequently they have no vibrational or rotational features involving electronic dipole radiation.

To a first approximation, the lower vibrational energy levels of a molecule correspond to those of a linear harmonic oscillator and are uniformly spaced at levels $E_v = (v + \frac{1}{2})h\nu_0$ where $v = 0, 1, 2, \ldots$ is the *vibrational quantum number* and ν_0 is the fundamental frequency of the oscillator. The selection rule for dipole radiation for this simple oscillator is $\Delta v = \pm 1$ and the relative oscillator strengths for bands with upper-state quantum number v is proportional to v. In practice, anharmonicities of various kinds lead to departures from uniform spacing of the levels, to violations of the selection rule, and to weak "overtone" bands for which $|\Delta v| \geq 2$.

In a vibration–rotation transition, the selection rule for dipole radiation associated with a rotational energy change for a linear molecule such as CO_2 is either $\Delta J = 0, \pm 1$ or $\Delta J = \pm 1$. Such bands exhibit either two or three subbands corresponding to the two or three possibilities for ΔJ. The subband with $\Delta J = +1$ in absorption is called the *R branch* and lines on the short-wavelength end of the band. The band with $\Delta J = -1$ in absorption, called the *P branch*, falls on the long wavelength end. The band with $\Delta J = 0$, if it occurs, falls in the middle and is called the *Q branch*. A schematic spectrum of a linear molecule with an unresolved strong Q branch and with the ideal uniform line spacing $2B/h$ in the P and R branches is shown in Fig. 2.10.

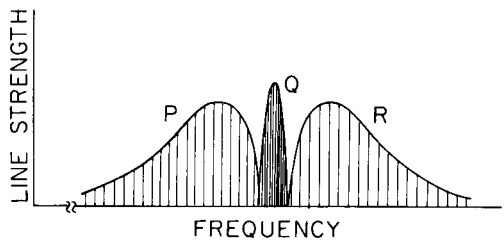

Fig. 2.10. Schematic vibration rotation band for a linear molecule showing the relationships between lines in the P, Q, and R branches.

2.3.4.b *Infrared Spectrum of CO_2*

Carbon dioxide is linear and symmetric in the ground state and has no pure rotational spectrum. The vibrational spectrum has three modes: symmetric stretching (ν_1), bending (ν_2), and asymmetric stretching (ν_3). Because of the symmetry of the ν_1 mode, transitions involving only ν_1 levels do not radiate, but the transition energy for ν_1 is very close to twice the transition energy for ν_2. As a result there is a strong interaction between ν_1 and ν_2, called *Fermi resonance*, and combined transitions involving changes in both ν_1 and ν_2 quantum numbers take place readily. Moreover, although there is no angular momentum about the molecular axis in the ground state, there is a contribution to this component of angular momentum in the excited ν_2 (bending) states. As a result of this, and of the Fermi resonant interaction with ν_1 for quantum numbers $v_2 \geqq 2$, these excited ν_2 energy levels split, and an additional angular momentum quantum number l is needed to represent these states. The vibrational state of CO_2 is described by the

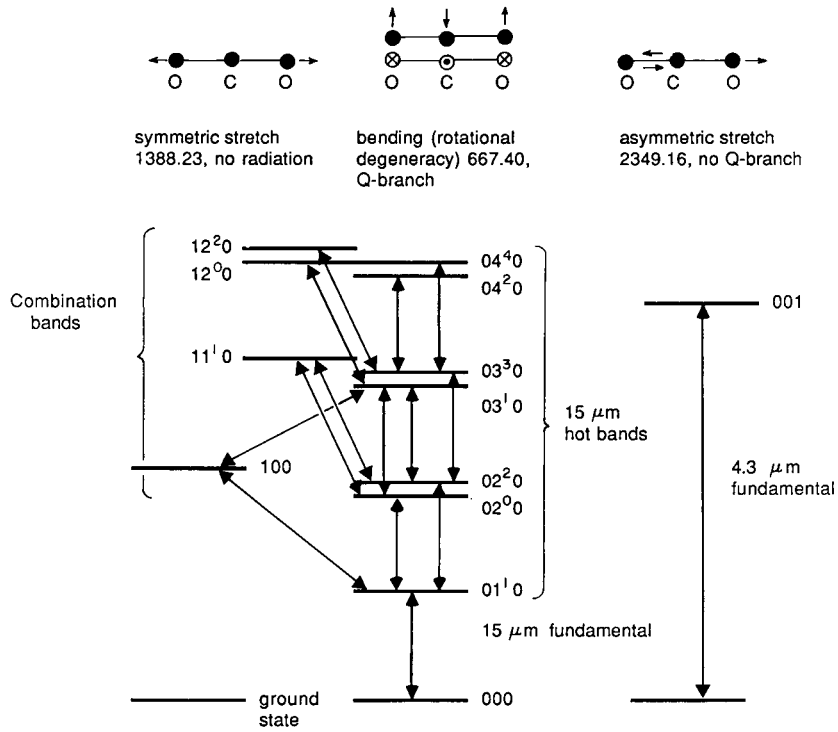

Fig. 2.11. Energy levels and vibrational transitions for CO_2. Note the large number of transitions corresponding to hot bands in the 15-μm region (667 cm^{-1}).

notation $(v_1\ v_2^l\ v_3)$; for example, 03^10 corresponds to $v_1 = 0$, $v_2 = 3$, $v_3 = 0$, and $l = 1$.

These energy levels are illustrated in Fig. 2.11, together with some of the allowed transitions producing bands in the 15-μm region. The transition 01^10-000 is the *fundamental* band. *Combination* bands such as 11^10-02^00 and 100-01^10 and *upper-state* bands such as 02^20-03^10 are together referred to as *hot bands*, since their strengths in absorption depend on molecular populations in excited states. As a consequence, intensities of these bands increase rapidly with temperature. The most important implication of Fig. 2.11 is that there are many CO_2 vibration-rotation bands in the 15-μm region, each with a slightly different central wave number, and each bearing a general resemblance to the schematic spectrum shown in Fig. 2.10. Strengths of all of these bands except the fundamental are very sensitive to temperature. This picture is further complicated by the occurrence of bands of minor isotopes of CO_2 in the same spectral region. The most important isotopic bands are the fundamentals of $^{13}C^{16}O^{16}O$ and $^{12}C^{18}O^{16}O$ with fractional concentrations of 0.0111 and 0.0020 relative to $^{12}C^{16}O^{16}O$. These isotopic bands are more important to the energetics of the mesosphere

Table 2.1

Band Intensities at 296 K for the 15-μm CO_2 Bands[a]

Isotopic species	Transition	Band center		Molecular band intensity[b]	Lower-state energy
		cm^{-1}	μm		
$^{12}C^{16}O^{16}O$	00^00-01^10	667.38	15.0	8.26×10^{-18}	0.0
	01^10-02^00	618.03	16.2	1.44×10^{-19}	667.38
	01^10-02^20	667.75	15.0	6.48×10^{-19}	667.38
	01^10-10^00	720.81	13.9	1.85×10^{-19}	667.38
	02^00-11^10	791.45	12.6	1.12×10^{-21}	1285.41
	02^00-03^10	647.06	15.5	2.22×10^{-20}	1285.41
	02^20-03^10	597.34	16.7	5.21×10^{-21}	1335.13
	02^20-03^30	668.12	15.0	3.82×10^{-20}	1335.13
	02^20-11^10	741.73	13.5	7.90×10^{-21}	1335.13
	10^00-03^10	544.29	18.4	2.72×10^{-22}	1388.19
	10^00-11^10	688.67	14.5	1.49×10^{-20}	1388.19
	03^30-04^40	668.47	15.0	2.00×10^{-21}	2003.24
$^{13}C^{16}O^{16}O$	00^00-01^10	648.48	15.4	8.60×10^{-20}	0.0
$^{12}C^{18}O^{16}O$	00^00-01^10	662.37	15.1	3.30×10^{-20}	0.0

[a] Data from Rothman and Young (1981) and Rothman *et al.* (1983). These authors use a different nomenclature for the energy levels than that used here which follows Goody (1964).

[b] Band intensities correspond to $S = \int \sigma_\nu\, d(\nu/c)$, in centimeters per molecule, and are reckoned with respect to the total number of CO_2 molecules, all isotopes.

than their concentrations would suggest. That is because their optical depths are sufficiently small even in the centers of the strongest lines that they can efficiently emit radiation to space (see Section 2.5). Table 2.1 lists properties of some of the important 15-μm CO_2 bands. Ramanathan *et al.* (1985) have found it necessary to include some 44 individual 15-μm bands in their investigations of climatic change effects of increasing CO_2 concentration.

Figure 2.12 shows spectra of CO_2 in the 15-μm region at low resolution. In addition to the P and R branches of the fundamental and some of the hot bands, Q branches of 02^20-03^10, 01^10-02^00, 02^00-03^10, 01^10-10^00, and 02^20-11^10 can be clearly identified with the help of the data in Table 2.1. Some of these are blended with the Q branches of the ν_2 fundamentals of $^{13}C^{16}O^{16}O$ and $^{12}C^{18}O^{16}O$.

A spectrum at much higher resolution is shown in Fig. 2.13. Note the unresolved Q branches, the apparently regular P branch in the bottom panel,

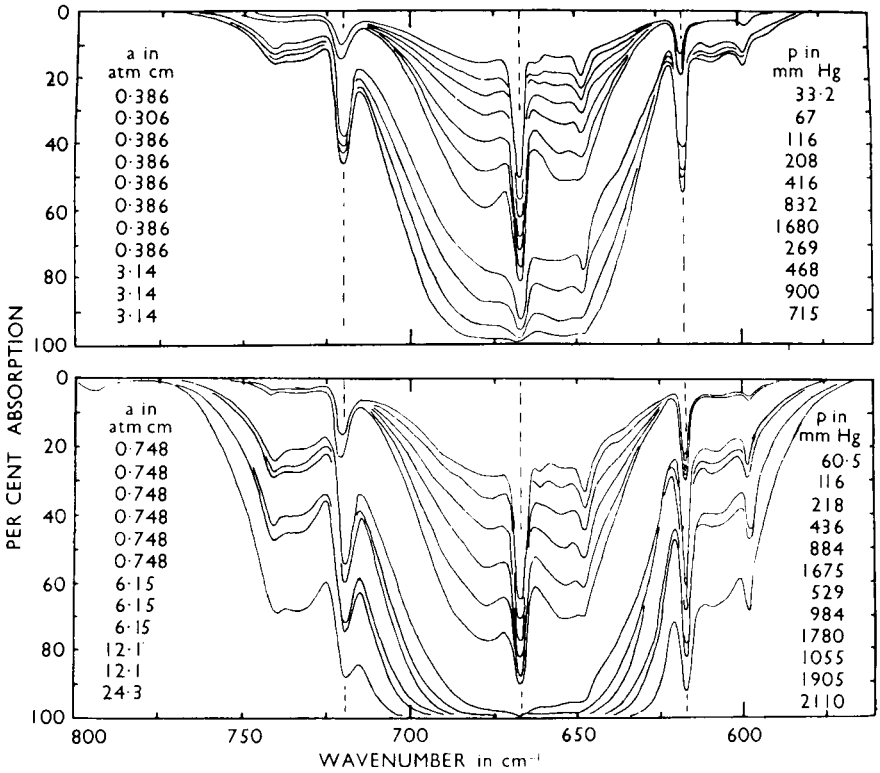

Fig. 2.12. Low-resolution laboratory absorption spectra of CO_2 at various combinations of optical path and pressure. Note the appearance of several Q branches as sharp absorption spikes. [From Burch *et al.* (1960), with permission.]

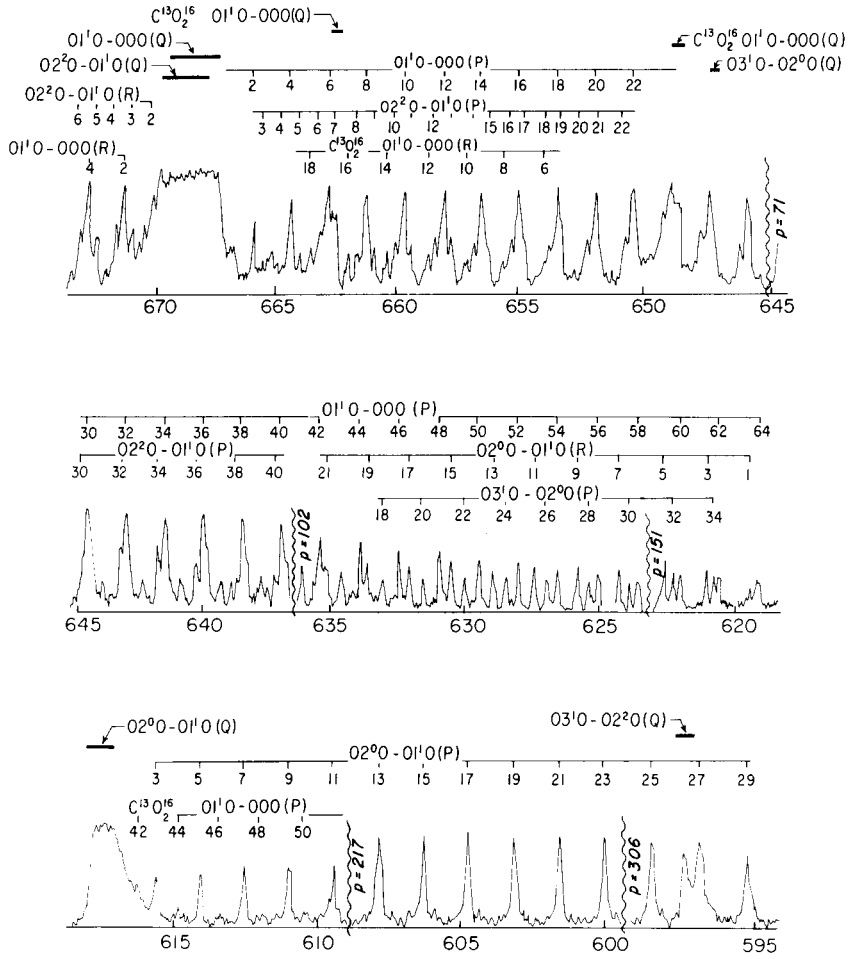

Fig. 2.13. Moderately high-resolution absorption spectrum of part of the 15-μm band of CO_2. Note that lines with odd J values are missing in the 01^10–000 and 03^10–02^00 transitions, while lines with even J values are missing from the 02^00–01^10 transition because of the high degree of symmetry of $^{12}C^{16}O_2$ and $^{13}C^{16}O_2$. Data have been replotted from Madden *et al.* (1957).

and the overlapping P and R branches in the top two panels. A significant feature of the spectrum is the absence of rotational lines corresponding to odd J values for transitions whose lower state has $l = 0$ (e.g., 000, 02^00). Because of the high degree of nuclear symmetry for $^{12}C^{16}O^{16}O$, antisymmetric rotational levels for these vibrational states are missing.

2.3.4.c Infrared Spectrum of H_2O

The thermal infrared bands of H_2O are comparable in strength to those of CO_2, but the H_2O concentration is nearly two orders of magnitude smaller throughout most of the middle atmosphere (~5 ppmv compared with 340 ppmv). Consequently, H_2O has a relatively minor influence on thermal infrared exchange, but it is not totally negligible.

Water vapor is nonlinear and asymmetric. It has a dipole moment in the ground state and a strong rotational band extending from the 15-μm spectral region toward longer wavelengths. This is the most important water-vapor band for thermal radiative exchange in the atmosphere. Of the vibration–rotation bands, only the ν_2 fundamental at 6.3 μm influences thermal radiative exchange in the middle atmosphere, and then only at relatively high temperatures. A number of other bands, including higher-overtone bands, occur in the near-infrared and visible spectral regions. They are responsible for absorption of solar radiation and significant heating in the troposphere, but because of the low water-vapor concentration they make only a minor contribution to heating in the middle atmosphere.

Because water vapor is nonlinear, it has three angular momentum components, in contrast to one for a linear molecule in the ground state, and as a consequence its spectrum is relatively complex. The most important consequence of this structure is that the H_2O rotation levels are split into $2J + 1$ sublevels, where J is the quantum number for total angular momentum. These sublevels are irregularly spaced, and for the larger values of J, sublevels for different J values overlap. The result is a spectrum with a random appearance of line positions and intensities, as illustrated in Fig. 2.14. Although the spectrum of water vapor has been studied for many years, the band parameters are not as accurately known as those for CO_2.

2.3.4.d Infrared Spectrum of Ozone

With mixing ratios ranging up to 15 ppmv and a strong thermal infrared spectrum, ozone is intermediate in importance to CO_2 and H_2O for infrared energy exchange in the middle atmosphere. It is also asymmetric, and it has a dipole moment in the ground state and a pure rotational spectrum. However, the important bands for thermal radiative exchange are the vibration–rotation bands. Strong ν_1 and ν_3 fundamentals at 1110 and 1045 cm^{-1} together with hot bands and minor isotopic bands in the same spectral region comprise the important 9.6-μm band system. The ν_2 fundamental at 701 cm^{-1} overlies the CO_2 15-μm band system and is at most of very minor significance for heating-rate calculations, but it has to be taken

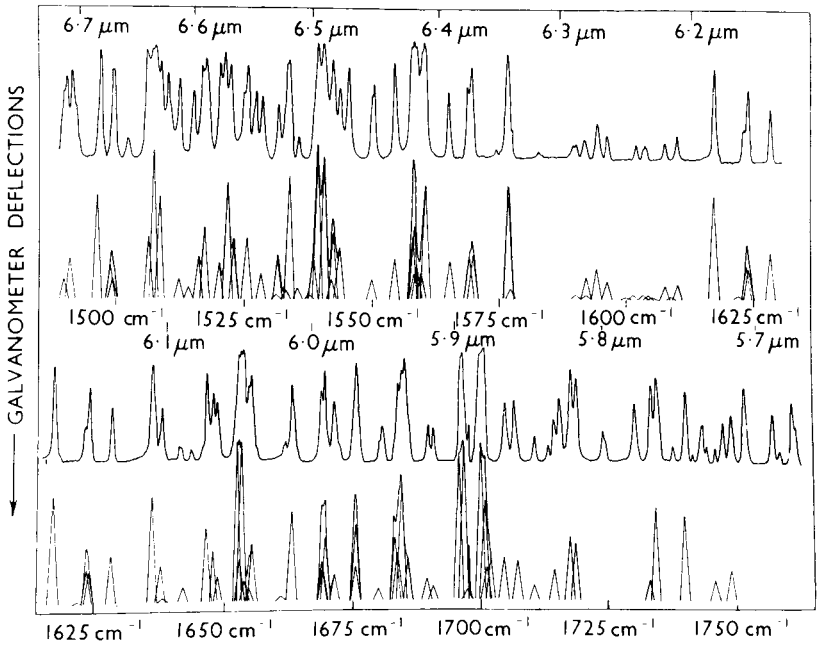

Fig. 2.14. Comparison between theoretical (triangles) and observed spectrum for H_2O in the 6.3-μm region. [From Nielsen (1941), with permission.]

into account in the calculation of accurate 15-μm band transmission functions for remote sensing purposes.

Because of the molecular asymmetry and the occurrence of hot and isotopic bands in the same spectral interval, the structure of the 9.6-μm band is very complex. Line positions and line strengths are rather randomly distributed, but average line spacings are smaller than those in the CO_2 or water-vapor bands. Spectroscopic parameters for O_3 are the least well known of the three gases, but because the contribution of ozone to the middle atmosphere cooling rate is generally less than one-third as large as that for CO_2, uncertainty in ozone spectroscopic parameters should make a relatively small contribution to net heating rate error.

2.3.4.e Other Gases

Minor contributions to the net heating of the atmosphere are made by infrared bands of methane (mixing ratio $\lesssim$1.6 ppmv), N_2O (mixing ratio $\lesssim$0.4 ppmv), HNO_3 (mixing ratio $\lesssim$0.01 ppmv), and the chlorofluoromethanes, $CFCl_3$ and CF_2Cl_2 (mixing ratios $\sim$1 ppbv). In combination, plausible increases in these gases could enhance the "greenhouse

effect" due to enhanced downward infrared radiation from the atmosphere by an amount comparable to that expected from doubling of the CO_2 concentration (see Section 12.3). At present, in the middle atmosphere, these gases contribute no more than a few hundredths of a degree per day to net heating. Since CH_4, N_2O, and $CFCl_3$ and CF_2Cl_2 have absorption bands in the relatively transparent atmospheric "window" region between 7 and 12 μm, so that these gases exchange radiation primarily with the warm underlying troposphere and surface, their main effect is to warm the extreme lower stratosphere and the tropopause region.

2.4 Transmission Functions

Exchange of radiation within the atmosphere and between the atmosphere and its surroundings is described by *transmission functions.* It is necessary to distinguish between *monochromatic* and spectrally averaged or *band* transmission functions and between *parallel beam* and *flux* transmission functions. The former describe the exchange of radiance and the latter describe the exchange of flux between isotropically emitting surfaces or layers. It is also useful to distinguish between transmission functions in the laboratory for which absorption and extinction coefficients are constant along optical paths and transmission functions in the atmosphere where absorption and extinction coefficients vary because of varying temperature and pressure along optical paths. In this and the following three sections, only gaseous absorption and emission (but no scattering) are considered, so that $\bar{\omega}_\nu = 0$ and $a_\nu = k_\nu$.

2.4.1 Definitions

The *monochromatic parallel beam transmission function* $T_\nu(s_1, s_2)$ appeared in Eq. (2.2.13) as the fraction of the monochromatic radiance leaving a point s_1 that reaches point s_2,

$$T_\nu(s_1, s_2) = \exp\left[-\int_{s_1}^{s_2} k_\nu(s)\rho_a(s)\, ds\right]. \tag{2.4.1}$$

For the laboratory path at pressure p and temperature T, the extinction coefficient can be removed from the integration, and Eq. (2.4.1) can be expressed in the form

$$T_\nu(p, T, u) = \exp[-k_\nu(p, T)u(s_1, s_2)] \tag{2.4.1'}$$

where

$$u(s_1, s_2) = \int_{s_1}^{s_2} \rho_a \, ds \tag{2.4.2}$$

is the optical mass between points s_1 and s_2. For a plane-parallel atmosphere, Eqs. (2.4.1) can be written in terms of the optical depth [Eq. (2.2.15b)],

$$T_\nu(s_1, s_2) = T_\nu(z_1, z_2, \mu) = \exp[-\mu^{-1} \Delta\tau_\nu(z_1, z_2)], \tag{2.4.1''}$$

where $\Delta\tau_\nu(z_1, z_2) = |\tau_\nu(z_2) - \tau_\nu(z_1)|$. Note that $\mu^{-1} \Delta\tau_\nu(z_1, z_2)$ is positive for both upward and downward paths.

Calculation of the exchange of thermal radiation requires integration over the infrared spectrum. This integration involves thousands of absorption lines, each with a rapidly varying profile. On the other hand, the source function is generally a slowly varying function of frequency [e.g., the Planck function of Eq. (2.2.10)], so that it is convenient to work with a spectrally integrated transmission function. This quantity, the *band transmission function* $\bar{T}_r$, is defined by

$$\bar{T}_r = \Delta\nu_r^{-1} \int_{\Delta\nu_r} T_\nu \, d\nu, \tag{2.4.3}$$

where $\Delta\nu_r$ is a spectral band width. This is usually taken to be wide enough to encompass many lines but narrow enough that spectral variations of the source function are small. Just as for the monochromatic transmission function, the functional dependences of the band transmission functions for laboratory and atmospheric cases are

$$\bar{T}_r(\text{lab}) = \bar{T}_r(p, T, u)$$

and

$$\bar{T}_r(\text{atmos}) = \bar{T}_r(z_1, z_2, \mu).$$

Two useful quantities that are closely related to $\bar{T}_r$ are the *band absorptivity*

$$\bar{A}_r = 1 - \bar{T}_r \tag{2.4.4}$$

and the *equivalent width* (expressed in frequency units),

$$W_r = \Delta\nu_r(1 - \bar{T}_r) = \int_{\Delta\nu_r} [1 - T_\nu] \, d\nu. \tag{2.4.5}$$

The latter is most often used in describing laboratory data, in which case

$$W_r = W_r(p, T, u).$$

Equivalent width is also known as the *integrated absorptance*. It can be applied either to a single isolated line or to a complete band such as the

9.6-μm band of O_3 or the 15-μm band of CO_2. The relationship between $W_r(p, T, u)$ and u for fixed p and T is called the *curve of growth.*

The *flux transmission function,* applicable to a plane-parallel atmosphere, is the μ-weighted angular average of Eq. (2.4.3),

$$\bar{T}_f(z_1, z_2) = \int_0^1 \mu \bar{T}_r(z_1, z_2, \mu)\, d\mu \cdot \left(\int_0^1 \mu\, d\mu \right)^{-1}$$

$$= 2 \int_0^1 \mu \bar{T}_r(z_1, z_2, \mu)\, d\mu. \tag{2.4.6}$$

For an isotropically radiating horizontal surface, this gives the fraction of the flux in band $\Delta\nu_r$ that reaches level z_2 after leaving level z_1 (or vice versa). The angular integration can be carried out explicitly,

$$\bar{T}_f(z_1, z_2) = \frac{2}{\Delta\nu_r} \int_{\Delta\nu_r} d\nu \int_0^1 \exp[-\Delta\tau_\nu(z_1, z_2)/\mu] \cdot \mu\, d\mu,$$

or, with the substitution $\eta \equiv \mu^{-1}$,

$$\bar{T}_f(z_1, z_2) = \frac{2}{\Delta\nu_r} \int_{\Delta\nu_r} E_3[\Delta\tau_\nu(z_1, z_2)]\, d\nu, \tag{2.4.7}$$

where $E_n(x)$ is the nth exponential integral,

$$E_n(x) = \int_1^\infty e^{-\eta x}\, d\eta/\eta^n. \tag{2.4.8}$$

We turn now to methods for evaluating transmission functions in the atmosphere from spectroscopic or laboratory data.

2.4.2 *Line-by-Line Integration*

The central problem is to carry out the spectral integration implied by Eq. (2.4.3), (2.4.5), or (2.4.7). Straightforward integration over the spectrum is the most accurate approach, but it is also extremely time consuming. For a bandwidth $\Delta\nu_r$ of 20 cm^{-1}, several hundred lines would have to be taken into account for the 15-μm CO_2 or 9.6-μm O_3 bands. This would imply several thousand spectral integration steps, which would have to be repeated 15–20 times to cover each relevant subband of width $\Delta\nu_r$ and for each pair of levels participating in the exchange. Since transmission functions depend on temperature and pressure, this process would have to be repeated for each atmospheric profile having a different temperature-pressure and/or absorbing gas-pressure relationship.

This is obviously an expensive process even for a very fast computer, but it is not prohibitive for limited calculations, and it can be used to provide benchmarks for approximate methods. It has the advantage that spectral variations are accurately evaluated and at the same time the effects of pressure and temperature on line strength and line width along the varying atmospheric paths can be accurately taken into account. Moreover, with the aid of a table or an efficient algorithm for obtaining the exponential integral, precise angular integration can also be incorporated in the calculation by using Eq. (2.4.7). The full Voigt line shape or accurate approximations to it can be readily used, the choice of approximation depending on the desired accuracy and the acceptable degree of complexity of the calculation. The accuracy of this approach is limited by the accuracy of the spectroscopic line parameters.

Fels and Schwarzkopf (1981) have carried out such a calculation for the 15-μm bands of carbon dioxide and have tabulated transmission functions between pairs of levels on a closely spaced grid between the surface and the upper mesosphere. For CO_2 the composition is uniform, but varying temperature profiles have to be taken into account. This was done by calculating transmission functions for a standard atmosphere temperature profile $T_0(p)$ and for "warm" and "cold" profiles, $T_0(p) + 25$ K and $T_0(p) - 25$ K. They were able to show that quadratic interpolation of transmission functions between these three sets of transmission functions using the mass-weighted mean temperature between the two endpoint levels of the transmission function provides a very accurate approximation to the exact flux transmission function for the entire 15-μm band system, provided that the actual temperature profile lies within the limits $T_0(p) + 25$ K and $T_0(p) - 25$ K. These tabulated values also incorporate a weighting factor to account for the spectral variation of the Planck function over the 15-μm band. Fels and Schwarzkopf have also carried out this calculation for higher CO_2 concentrations, since these may be relevant in the future.

2.4.3 Band Models

Because the concentrations of water vapor and ozone vary, no line-by-line method that is generalizeable to arbitrary temperature and composition profiles has been applied to these gases. This is one reason for considering a simplified transmission-function computation based on approximating the structure of vibration-rotation bands by specific models. Another advantage of this approach is that it makes clear the limiting behavior of transmission functions in important asymptotic regimes. Four specific issues will be dealt with in turn: treatment of the spectral integration along paths at

constant pressure and temperature for Lorentz lines, treatment of varying pressure and temperature along the path, angular integration, and treatment of the transition to the Doppler line shape.

Consider first the absorptivity for a single line along a path at constant pressure and temperature $\bar{A}_1$ over an interval $\Delta\nu_r$ that is symmetric about the line center. This absorptivity is

$$\bar{A}_1 = \frac{1}{\Delta\nu_r}\int_{\Delta\nu_r}[1 - e^{-k_\nu u}]\,d\nu$$

$$= \frac{1}{\Delta\nu_r}\int_{\Delta\nu_r}\{1 - \exp[-\tilde{S}f(\nu)u]\}\,d\nu \tag{2.4.9}$$

where $f(\nu)$ is the line-shape factor normalized to unity with line-center frequency set equal to zero and $\tilde{S}$ is the line strength referenced to absorber mass rather than to absorber number as in Eqs. (2.3.2) ($\tilde{S} \equiv S/M_a = \int k_\nu\,d\nu$). If the lines in the band are sufficiently well separated that their overlapping contributions to absorption are negligible, Eq. (2.4.9) can be approximated by

$$\bar{A}_1 \simeq \frac{1}{\delta}\int_{-\infty}^{\infty}\{1 - \exp[-\tilde{S}f(\nu)u]\}\,d\nu \tag{2.4.10}$$

where δ is the mean spacing between lines. Above about 25 km, this isolated line approximation is sufficiently accurate for the P and R branches of CO_2 and for water vapor. It is also adequate for CO_2 Q branches and the O_3 9.6-μm band above about 40 km.

When $f(\nu)$ is the Lorentz line shape, the integral in Eq. (2.4.10) can be expressed in a closed form, known as the *Ladenberg-Reiche* function,

$$\bar{A}_1(y, \hat{u}) = \hat{u}e^{-\hat{u}}[I_0(\hat{u}) + I_1(\hat{u})] \tag{2.4.11}$$

where

$$y = \alpha_L/\delta, \qquad \hat{u} = \frac{\tilde{S}u}{2\pi\alpha_L} \tag{2.4.12}$$

and I_0 and I_1 are modified Bessel functions. The isolated line absorptivity, $\bar{A}_1$, has useful asymptotic limits that can be derived without reference to Eq. (2.4.11). For sufficiently small $\hat{u}$, the exponential in Eq. (2.4.10) can be replaced by the first two terms in its power series expansion, so that

$$\bar{A}_1 \to \frac{\tilde{S}u}{\delta}\int_{-\infty}^{\infty} f(\nu)\,d\nu = \tilde{S}u/\delta = 2\pi y\hat{u} \qquad \text{as} \quad \hat{u} \to 0. \tag{2.4.13}$$

This *weak line limit* is valid for any line shape provided that absorption is sufficiently weak in the line center. On the other hand, if the line is fully

absorbed, or *saturated*, in the line center and for some spectral distance on either side of the center, most of the contribution to $\bar{A}_1$ comes from the line wings for which the Lorentz profile can be approximated by $f(\nu) \approx \alpha_L/\pi\nu^2$. Substitution of this expression into Eq. (2.4.10) leads to the *strong line limit*,

$$\bar{A}_1 \to 2y(2\pi\hat{u})^{1/2} = \frac{2}{\delta}(\tilde{S}u\alpha_L)^{1/2}. \tag{2.4.14}$$

The Ladenberg-Reiche formula interpolates between these two asymptotic regimes.

Next consider the mean absorptivity for a band containing an array of nonoverlapping lines whose strength distribution is described by the density function $\hat{Q}(\tilde{S})$ such that $\hat{Q}(\tilde{S})\,d\tilde{S}$ represents the probability that a line selected at random from the array has strength between $\tilde{S}$ and $\tilde{S} + d\tilde{S}$. It follows that the average absorptivity of the band is

$$\bar{A}_{sl} \approx \frac{1}{\delta}\int_{-\infty}^{\infty}\int_{0}^{\infty} \hat{Q}(\tilde{S})[1 - e^{-\tilde{S}f(\nu)u}]\,d\tilde{S}\,d\nu. \tag{2.4.15}$$

Equation (2.4.15) can be evaluated in closed form for the Lorentz line shape and some reasonably realistic line strength distributions. Absorptivities $\bar{A}_{sl}$ also have weak and strong limits, but mean absorptivities for the cases with distributed line strengths approach the strong line limit more slowly than the isolated single line absorptivity $\bar{A}_1$ because line arrays include very weak lines, which are slow to saturate.

When line overlap is important, the monochromatic transmission function for the overlapping lines is the product of the monochromatic transmission functions for the individual lines. Thus, for n overlapping lines.

$$T_\nu = \prod_{i=1}^{n} e^{-k_{\nu,i}u} = \exp\left[-\sum_{i=1}^{n} k_{\nu,i}u\right]. \tag{2.4.16}$$

A widely used model for incorporating the effects of line overlap into the evaluation of absorptivity is the *random model*. It is assumed that line centers are randomly distributed over the band width $\Delta\nu_r$, that the probability of any line being centered at a particular position in the interval is independent of the probability that any other line is at any other position in the interval, and that the line strength probability distribution for any line is independent of the strengths of all other lines. With these assumptions, Eq. (2.4.16) can be evaluated for any line shape, and the result is the general random model,

$$\bar{T}_n = \left(1 - \frac{W_{sl}}{n\delta}\right)^n, \tag{2.4.17}$$

where $W_{sl} \equiv \bar{A}_{sl}\delta$ is the average single-line equivalent width from Eqs.

(2.4.15). Equation (2.4.17) is usually applied in the limit $n \to \infty$, in which case

$$\bar{T}_n \to \bar{T}_r(\text{random}) = e^{-W_{sl}/\delta}. \tag{2.4.18}$$

Note that for strongly overlapping lines W_{sl}/δ may exceed unity.

Two distributions of line strength that are reasonable representations of actual line strength distributions for some bands are

$$\hat{Q}(\tilde{S}) = \frac{1}{\sigma} e^{-\tilde{S}/\sigma} \tag{2.4.19}$$

and

$$\tilde{Q}(\tilde{S}) = \tilde{S}^{-1} e^{-\tilde{S}/\sigma}, \tag{2.4.20}$$

where σ is a constant characterizing the distribution. Equation (2.4.20) is singular at the origin and so can be useful for representing a band with a relatively large number of very weak lines. With $\hat{u} \equiv \sigma u/2\pi\alpha_L$, the first of these leads to the *Goody model*,

$$\bar{T}_r(\hat{u}, y) = \exp[-2\pi y\hat{u}(1 + 2\hat{u})^{-1/2}], \tag{2.4.21}$$

while the second leads to the *Malkmus model*,

$$\bar{T}_r(\hat{u}, y) = \exp\{-2\pi y[(1 + 2\hat{u})^{1/2} - 1]\}. \tag{2.4.22}$$

These transmission functions have the following asymptotic limits. (1) If $\hat{u}$ is small, $\bar{T}_r \to e^{-2\pi y\hat{u}} = e^{-\sigma u/\delta}$ in both cases. In this limit, absorption is very weak in the centers of the lines of average strength and the transmission function has the same form as for spectrally uniform (gray) absorption with absorption coefficient σ/δ. If in addition $2\pi y\hat{u} \ll 1$, the lines are well separated and $\bar{T}_r \to 1 - 2\pi y\hat{u} = 1 - \sigma u/\delta$, the isolated weak line limit for a line of strength σ. (2) If $\hat{u}$ is large, $\bar{T}_r \to e^{-\pi y(2\hat{u})^{1/2}}$ for the Goody model and $\bar{T}_r \to e^{-2\pi y(2\hat{u})^{1/2}}$ for the Malkmus model. If in addition $y^2\hat{u} \ll (2\pi)^{-2}$, the lines are well separated and $\bar{T}_r(\text{Goody}) \to 1 - \pi y(2\hat{u})^{1/2}$ and $\bar{T}_r(\text{Malkmus}) \to 1 - 2\pi y(2\hat{u})^{1/2}$. These expressions correspond to the square-root regime of the isolated strong line.

Equations (2.4.21) and (2.4.22) are best thought of as physically motivated expressions for the band transmission function, which can be optimized in applications by fitting to characteristics of any particular spectral interval $\Delta\nu_r$ as determined from laboratory data or from calculations based on the fundamental spectroscopic parameters.

The Goody model applied to 10-cm^{-1} band intervals provides an excellent representation of transmission in the 6.3-μm and rotation bands of water vapor. Since the 9.6-μm band of ozone and particularly the 15-μm band system of CO_2 are less random, they are more difficult to represent with random models, but the Malkmus model has been shown by Kiehl and

Ramanathan (1983) to give an excellent representation of transmission in these bands, provided it is applied to narrow spectral intervals ($\sim 5\ \mathrm{cm}^{-1}$ in width).

The random models are most useful when applied to relatively narrow spectral divisions of a band. Whole-band absorptivity formulations are also available and can be used to provide transmission functions with accuracies of 10% or better for H_2O, O_3, CO_2, CH_4, and N_2O. One widely used form for such models that is particularly useful for weak bands is the exponential sum fit. In this approximation, the equivalent width is represented by

$$W_r(u) = \Delta\nu_r\left[1 - \sum_{i=1}^{n} f_i e^{-\tau_i}\right], \tag{2.4.23a}$$

$$\tau_i = \left(\frac{k_i}{f_i}\right)\left(\frac{\tilde{S}u}{\Delta\nu_r}\right); \tag{2.4.23b}$$

constrained by

$$\sum_{i=1}^{n} f_i = \sum_{i=1}^{n} k_i = 1, \tag{2.4.23c}$$

where the model parameters k_i, f_i, $\tilde{S}$, and $\Delta\nu_r$ are obtained by fitting laboratory data. Note that in the weak absorption limit Eq. (2.4.23a) gives $W_r(u) \to \tilde{S}u$.

A whole band equivalent width formulation that is more appropriate to strong bands has been widely used in the stratospheric calculations by Cess and Ramanathan and their collaborators. The equivalent width W_r is represented by

$$W_r = 2A_0(T)\ln\left(1 + \sum_{i=1}^{n} \xi_i^{1/2}\right) \tag{2.4.24a}$$

where

$$\xi_i = \frac{4\alpha_{\nu i}\tilde{S}_i u}{A_0(T)\delta} \tag{2.4.24b}$$

and the summation is over n overlapping bands of strengths $\tilde{S}_i$ with lines of Lorentz half-width $\alpha_{\nu i}$ and mean spacing δ in the spectral interval. The effective band width parameter $A_0(T)$ is determined by comparing W_r with laboratory data. Note that in the limit $\xi_i \to 0$, the dependence on half-width, band intensity, and optical path corresponds to the nonoverlapping strong line limit.

Water vapor is a special case because its absorption covers such broad spectral intervals. In this case, it is convenient to define an *emissivity* ε_1

appropriate for laboratory situations,

$$\varepsilon_l(p, T, u) = \int_0^\infty B_\nu(T)[1 - T_\nu(p, T, u)]\, d\nu/(\sigma T^4/\pi),$$

and the corresponding *flux emissivity*,

$$\varepsilon_f(p, T, z_1, z_2) = 2\pi \int_0^1 \mu\, d\mu \int_0^\infty B_\nu(T)[1 - T_\nu(z_1, z_2, \mu)]\, d\nu/\sigma T^4$$

$$= 2\int_0^1 \varepsilon_l[\tilde{p}, \tilde{T}, \tilde{u}(\mu)]\mu\, d\mu, \tag{2.4.25}$$

where $\tilde{p}$, $\tilde{T}$, and $\tilde{u}$ are appropriate mean values for the slant path at angle $\cos^{-1}\mu$ between z_1 and z_2. Such expressions are particularly useful for water vapor because the temperature dependence arising from the Planck function through the factor $T^{-4}B_\nu(T)$ is quite small. Water vapor has strong absorptions on both extremes of the Planck function, the rotation and 6.3-μm bands, so that there is a high degree of cancellation between the opposing temperature dependences of the two bands. The resulting small temperature dependence of ε_f makes it possible to carry out surprisingly accurate flux calculations using simple expressions of the form

$$F_\uparrow(z) = \int_0^1 \sigma T^4\, d\varepsilon_f(z', z), \tag{2.4.26}$$

with the convention that T corresponds to the surface temperature for values of ε_f such that $\varepsilon_f(z', z) > \varepsilon_f(0, z)$. However, when this formulation is used, it is necessary to take overlapping bands such as the 15-μm CO_2 band into account.

2.4.4 Treatment of Pressure and Temperature Variations along the Path

All of the models discussed above are applicable directly to parallel-beam transmission along a constant-pressure and constant-temperature path for the Lorentz line shape. Along vertical paths, the actual line shape is not Lorentz. It is a composite of high- and low-pressure Lorentz lines with broad high-pressure wings and a narrow low-pressure line center (Fig. 2.15). Approximate treatments of the variation of temperature and pressure along the atmospheric paths depend on the type of band model. For one-parameter models, such as Eq. (2.4.23), a scaling approximation can be employed.

In scaling approximations, pressure and temperature dependences are arbitrarily assumed to be separable from frequency dependence,

$$k_\nu(p, T) = \phi(p, T)\psi(\nu).$$

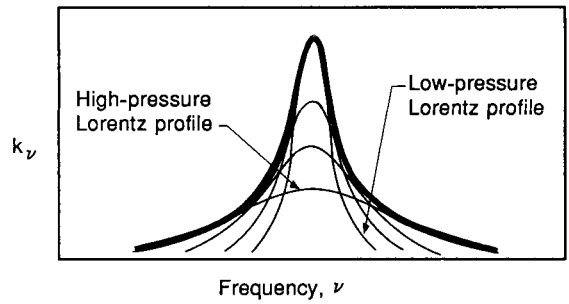

Fig. 2.15. Schematic composite showing how an actual line profile over a variable pressure path forms as a composite of the individual Lorentz profiles. The atmospheric line profile is not Lorentz in general; it is more sharply peaked because of low-pressure contributions, with broader wings due to high-pressure contributions.

Then

$$\Delta\tau_\nu = \int \psi(\nu)\phi(p, T)\, du = \psi(\nu) \int \phi(p, T)\, du$$

$$= k_\nu(p_r, T_r) \int [\phi(p, T)/\phi(p_r, T_r)]\, du = k_\nu(p_r, T_r)\tilde{u},$$

where

$$\tilde{u} \equiv \int [\phi(p, T)/\phi(p_r, T_r)]\, du$$

is a scaled absorber mass and p_r and T_r are reference pressure and temperature. Spectral integration can then be carried out at (p_r, T_r), or the laboratory transmission function measured at (p_r, T_r) can be used. Atmospheric transmission over path $\Delta\tau_\nu$ is then a function of the single parameter $\tilde{u}$, and we have the equivalence

$$\bar{T}_r(\tilde{u}, \text{atmosphere}) \leftrightarrow \bar{T}_r(u, p_r, T_r, \text{laboratory}). \tag{2.4.27}$$

Pressure dependence is frequently represented by a power law, so that

$$\phi(p, T) = \bar{S}(T)(p/p_r)^n$$

where $\bar{S}$ is a mean line strength for the interval and the empirical exponent n is determined from laboratory measurements at varying pressures. With this approximation,

$$\tilde{u} = \int \frac{\bar{S}(T)}{\bar{S}(T_r)}(p/p_r)^n\, du. \tag{2.4.28}$$

In the weak line limit, absorption is independent of pressure so that $n \approx 0$ is appropriate for weak absorption. In the strong line limit, absorption is proportional to the square root of the product of pressure and absorber mass so that $n \approx 1$ is appropriate for this limit, and in general $0 \lesssim n \lesssim 1$. The scaling approximation works fairly well for the troposphere, but it is a poor approximation if important contributions to radiative exchange are distributed over more than about two scale heights.

The random models are two-parameter models depending on an optical path parameter $\hat{u}$ and a line-width parameter y. For these models, there is a more satisfactory approximation, the *Curtis-Godson approximation.* In this approximation, the equivalence

$$\bar{T}_r(\tilde{u}, \tilde{p}, \text{atmosphere}) \leftrightarrow \bar{T}_r(u, p, T, \text{laboratory}) \tag{2.4.29}$$

is made. The equivalent width in the denominator of the Lorentz line shape [Eq. (2.3.5)] is replaced by a suitable mean value $\tilde{\alpha}$, so that, from Eq. (2.4.16),

$$\bar{T}_r \approx \frac{1}{\Delta\nu_r}\int_{\Delta\nu_r} d\nu \exp\left[-\int du \frac{\sum S_i\alpha_i}{\pi(\nu^2 + \tilde{\alpha}^2)}\right].$$

This expression, which varies from the exact expression only by the replacement of α by $\tilde{\alpha}$ in the denominator, is accurate in the strong line limit since $\tilde{\alpha}$ is neglected in the frequency integration in this case. The choice of $\tilde{\alpha}$ is then determined by requiring that this approximation provide an exact match to the weak limit,

$$\bar{T}_r(\text{weak}) \to 1 - \frac{1}{\Delta\nu_r}\int du \sum S_i.$$

Thus,

$$1 - \frac{1}{\Delta\nu_r}\int du \int_{\Delta\nu_r} \frac{\sum S_i\alpha_i}{\pi(\nu^2 + \tilde{\alpha}^2)}\, d\nu = 1 - \frac{1}{\Delta\nu_r}\int du \frac{\sum S_i\alpha_i}{\tilde{\alpha}}$$

$$= 1 - \frac{1}{\Delta\nu_r}\int du \sum S_i,$$

so that

$$\tilde{\alpha} = \int [\textstyle\sum(S_i\alpha_i)]\, du \Big/ \int (\textstyle\sum S_i)\, du.$$

Since $\alpha_i \approx (p/p_r)\alpha_r$ where α_r is the Lorentz width at standard pressure, and $\sum S_i = n\bar{S}(T)$, the path length and pressure in any two-parameter representation can be replaced by their Curtis-Godson means:

$$\tilde{p} = \frac{1}{\tilde{u}}\int p[\bar{S}(T)/\bar{S}(T_r)]\, du \tag{2.4.30a}$$

$$\tilde{u} = \int [\bar{S}(T)/\bar{S}(T_r)]\, du. \tag{2.4.30b}$$

If the temperature dependence is neglected, the Curtis-Godson mean pressure is just the absorber mass weighted mean pressure. The Curtis-Godson approximation has been shown to be very accurate for absorbing gases whose concentration decreases monotonically with height. It is less accurate but still useful in the case of ozone, whose concentration increases with height in the troposphere and lower stratosphere.

2.4.5 *Angular Integration*

Next, consider the problem of converting the parallel-beam band transmission functions derived from band models into flux transmission functions. This can be done straightforwardly by evaluating the integrand of Eq. (2.4.6) at Gaussian quadrature points and carrying out the Gaussian integration. At each quadrature point, one simply replaces $\tilde{u}$ evaluated from Eq. (2.4.28) or (2.4.30b) with $\tilde{u}/\mu$. Convergence of the integration is rapid, and good accuracy can be achieved with only a small number ($\sim$2) of Gaussian points. However, a simpler approach is to take advantage of the fact that diffuse radiance for a plane-parallel atmosphere is at least approximately equivalent to direct beam radiance at some intermediate value of μ. In fact, heating rates in the troposphere and stratosphere can be calculated with an accuracy of $\sim$1% with the approximation

$$\bar{T}_f(\tilde{p}, \tilde{u}) \simeq \bar{T}_r(\tilde{p}, \tilde{u}/\bar{\mu}), \tag{2.4.31}$$

where

$$\bar{\mu} \approx \tfrac{3}{5}.$$

The reason for the surprising accuracy of this "diffuse flux factor approximation" for heating rate can be understood by returning to the exponential integral form of the flux transmission function of Eq. (2.4.7). It will be shown in Section 2.5 that the band heating rate at level z depends on the derivative of $\bar{T}_f$, $\partial \bar{T}_f(z, z')/\partial z$, or

$$\begin{aligned} \frac{\partial \bar{T}_f}{\partial z} &= \pm \frac{2\rho_{a0}(z)}{\Delta \nu_r} \int_{\Delta \nu_r} k_\nu(z) \frac{dE_3(\Delta \tau_\nu)}{d(\Delta \tau_\nu)}\, d\nu \\ &= \pm \frac{2\rho_{a0}(z)}{\Delta \nu_r} \int_{\Delta \nu_r} k_\nu(z) E_2(\Delta \tau_\nu)\, d\nu, \end{aligned} \tag{2.4.32}$$

where the sign depends on whether $\Delta \tau_\nu$ increases ($-$) or decreases ($+$) with z. The ν-dependence of the two factors in the integrand of Eq. (2.4.32) is

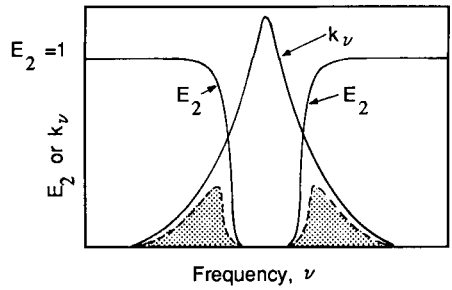

Fig. 2.16. Factors in the integrand of $\int \kappa_\nu E_2(\Delta\tau_\nu)\, d\nu$. Only the shaded areas contribute to the integral, and hence to $d\bar{T}_i/dz$.

depicted in Fig. 2.16 for a single line that is strong enough to be saturated in the center. Near the line center $E_2 \approx 0$, and in the far wings $k_\nu \approx 0$. Consequently, contributions to the integrand come only from the fairly narrow intervals in which $\Delta\tau_\nu \approx 1$. For any value of $\Delta\tau_\nu$, a quantity $\bar{\mu}^{-1}$ can be found such that

$$2E_3(\Delta\tau_\nu) = \exp(-\bar{\mu}^{-1}\Delta\tau_\nu),$$

where $1.5 \leq \bar{\mu}^{-1} \leq 2$. For $\Delta\tau_\nu = 1$, $\bar{\mu}^{-1} \approx \frac{5}{3}$. Thus, the accuracy and widespread applicability of the diffuse flux factor approximation stems from the fact that exchange in the strong bands of interest is dominated by spectral intervals in which $\Delta\tau_\nu \approx 1$. For very weak bands, the lines may be unsaturated near the centers and this may not be the case; instead, exchange may be dominated by smaller values of $\Delta\tau_\nu$, and a larger value of $\bar{\mu}^{-1}$ would be appropriate. For such bands, Gaussian quadrature may be used. Alternatively, where an exponential sum fit to whole band absorptivity is used, the diffuse flux factor can be used with great accuracy with $\bar{\mu}^{-1}$ given by

$$\bar{\mu}^{-1} = 1.5 + \frac{0.5}{1 + 4\tau_i + 10\tau_i^2} \tag{2.4.33a}$$

with τ_i obtained from Eq. (2.4.23b),

$$\tau_i = \sum_j \left(\frac{k_i}{f_i}\right)_j \left(\frac{\tilde{S}u}{\Delta\nu_r}\right)_j, \tag{2.4.33b}$$

where the summation is over all gases overlapping in the interval $\Delta\nu_r$ (Ramanathan *et al.*, 1985).

2.4.6 Voigt Line-Shape Effects

The treatment up to this point is applicable to Lorentz lines. It is also applicable to any line shape in the weak line limit, since transmission

functions are independent of line shape in this limit. In the upper stratosphere and mesosphere, the transition to the Doppler line shape has a strong influence on transmission functions and net heating rates. The exact Voigt line shape can be used for line-by-line integrations. When band models are employed, however, approximate treatments of the Voigt line shape are needed. Fortunately, Voigt effects are important only where line overlap is negligible, so that it is sufficient to consider Voigt shape effects for isolated lines.

Consider the behavior of an isolated Voigt line on constant-pressure-constant-temperature paths as a function of two parameters, $\hat{u} = \tilde{S}u/2\pi\alpha_L$ and $d = 2\alpha_L/\tilde{\alpha}_D$, where $\tilde{\alpha}_D = (\ln 2)^{1/2}\alpha_D$ is the Doppler half-width. Since the Voigt shape resembles the Doppler shape in the line center for $d < 1$, the maximum line-center strength is $\sim(\pi\tilde{\alpha}_D)^{-1}\tilde{S}u/(\ln 2)^{1/2}$. If this is sufficiently small, the weak line approximation applies and $\bar{A}_l \approx \tilde{S}u/\delta$. On the other hand, if the line is saturated throughout the Doppler line core region, only the Lorentz wings influence the transmission and $\bar{A}_l \approx 2(\tilde{S}u\alpha_L)^{1/2}/\delta$. Between these regimes, if d is sufficiently small that the line has a definite Doppler core, the "shoulders" and wings of the Doppler core dominate transmission. Since $f(\nu)$ falls off rapidly in the Doppler wings, the growth of $\bar{A}_l$ with $\hat{u}$ is relatively slow in this regime. Despite this relatively slow growth of absorption in the Doppler regime, the principal effect of the Voigt shape on atmospheric absorption and net heating rate is to increase the rate of change of absorption and the heating rate over values that would be obtained in the corresponding low pressure Lorentz regime. This is because the Lorentz line continues to narrow and strengthen in the line center as the pressure drops, so that absorption for a strong Lorentz line remains in the strong line regime even at very low pressure if the Voigt shape is neglected. In contrast, the transition to the weak line regime at low pressure does occur for Voigt lines because of the finite lower limit to line half-width and the corresponding maximum strength at line center, and $\bar{A}_l$ varies much more rapidly with absorber mass in the weak line regime than in the strong line regime.

Several approximate methods of incorporating the Lorentz-Doppler transition into band models have been suggested. One approach is to incorporate a smooth transition from Lorentz equivalent width W_L to Doppler equivalent width W_D. An interpolation formula suggested by Rodgers and Williams (1974) for this purpose is

$$W = \left[W_L^2 + W_D^2 - \frac{2W_L W_D}{(\tilde{S}u)^2} \right]^{1/2} \tag{2.4.34}$$

Alternatively, Ramanathan (1976) has suggested that W_L be used when $dW_L/du > dW_D/du$ and that W_D be used otherwise. Fels (1979) has shown

that the line shape

$$
\begin{aligned}
f(\nu) &= C, \qquad |\nu| < |\nu_0| \qquad \text{(core)},\\
f(\nu) &= \alpha_L/\pi\nu^2, \qquad |\nu| > |\nu_0| \qquad \text{(wings)},\\
\nu_0 &= \varepsilon\alpha_L + \beta\alpha_D, \qquad (\varepsilon, \beta \text{ are constants } \sim 1)\\
C &= \frac{1}{2\nu_0} - \frac{\alpha_L}{\pi\nu_0^2},
\end{aligned}
\tag{2.4.35}
$$

might be used to approximate the behavior of isolated lines in the Voigt regime. This approximation reduces to the correct weak line limit and mimics the effect of strong line regimes that depend on the value of α_L/α_D. It can also be easily incorporated into random band models. Figure 2.17 shows the behavior of equivalent width for emission of radiation to space using the Goody random model and Eq. (2.4.35). The overlapping Lorentz, nonoverlapping strong line, weak line, and Doppler regimes can be clearly distinguished. Because actual band transmission functions involve the integrated effects of lines with a wide range of strengths, approximate treatments such as Eqs. (2.4.34) and (2.4.35), which are asymptotically

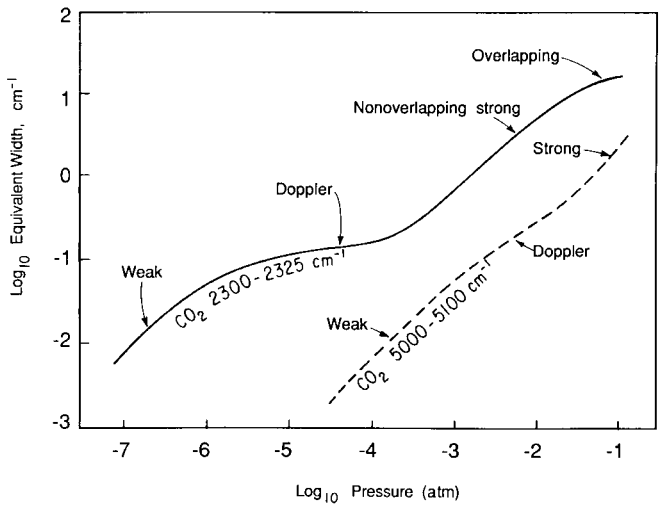

Fig. 2.17. Log-log plot of equivalent width versus pressure for the path between the indicated pressure level and space for a strongly absorbing spectral interval (CO_2, 2300-2325 cm^{-1}) and a weakly absorbing interval (CO_2, 5000-5100 cm^{-1}). The Goody random model with the Curtis-Godson approximation and the Fels approximation to the Voigt line shape have been used. Note the linear behavior in both weak and nonoverlapping strong line limits. Heating rate per unit mass due to solar absorption in these bands is proportional to W/p times the slope of these curves.

correct in weak and strong line limits, generally produce accuracies of ~20% or better in heating-rate calculations.

2.5 Infrared Radiative Exchange and Radiative Damping

In a plane-parallel atmosphere, consider the upward and downward flux densities integrated over a band of width $\Delta\nu_r$ [$F_{r\uparrow}(z)$ and $F_{r\downarrow}(z)$] at a log-pressure level z in an atmosphere bounded below by a surface radiating as a blackbody at $z = 0$, and unbounded above. If the band is sufficiently narrow that the Planck function is essentially constant over the band and, moreover, if $\bar{\omega}_\nu = 0$ for the entire band, if surface emissivity is unity, and if local thermodynamic equilibrium prevails, it follows from Eqs. (2.4.1″), (2.4.3), (2.2.18), (2.2.21), and (2.4.6) that

$$F_{r\uparrow}(z) = \pi B_r(0_-)\bar{T}_f(0, z) + \pi \int_0^z B_r(z') \frac{\partial \bar{T}_f(z, z')}{\partial z'} dz' \tag{2.5.1}$$

and

$$F_{r\downarrow}(z) = -\pi \int_z^\infty B_r(z') \frac{\partial \bar{T}_f(z, z')}{\partial z'} dz', \tag{2.5.2}$$

where $B_r(z)$ is the Planck function integrated over the interval $\Delta\nu_r$. Note that $\partial \bar{T}_f(z, z')/\partial z' < 0$ in Eq. (2.5.2), so that $F_{r\downarrow}(z) > 0$. The notation $B_r(0_-)$ is used to distinguish the Planck function at the surface from that of the immediately adjacent atmosphere, allowing for the possibility of a temperature discontinuity at the surface.

The heating rate per unit mass of air due to band r, $h_r(z)$, is given by

$$h_r(z) = -\rho^{-1} \frac{dF_{n,r}}{dz^*} = -\rho_0^{-1} \frac{dF_{n,r}}{dz}, \tag{2.5.3}$$

where $F_{n,r} = F_{r\uparrow} - F_{r\downarrow}$ is the net upward flux in the band. In this equation $\rho(z)$ is the air density and $\rho_0(z)$ is the basic density in the log-pressure coordinate system [see Section 3.1.1 and the discussion following Eq. (2.2.15)]. It follows that

$$h_r(z) = -[\pi/\rho_0(z)]\left\{ B_r(0_-) \frac{d\bar{T}_f(0, z)}{dz} + \int_0^z B_r(z') \frac{\partial^2 \bar{T}_f(z, z')}{\partial z\, \partial z'} dz' + \int_z^\infty B_r(z') \frac{\partial^2 \bar{T}_f(z, z')}{\partial z\, \partial z'} dz' - B_r(z) \left[\frac{\partial \bar{T}_f(z, z')}{\partial z'} \right]_{z'=z_-}^{z'=z_+} \right\}, \tag{2.5.4}$$

the last term giving the contribution due to the jump in $\partial \bar{T}_f(z, z')/\partial z'$ at $z' = z$.

2.5.1 *Exchange Integral Formulation*

Equation (2.5.4) can be rearranged to give

$$h_r(z) = [\pi/\rho_0(z)]\left\{-B_r(z)\frac{d\bar{T}_f(z,\infty)}{dz} - [B_r(0_-) - B_r(z)]\frac{d\bar{T}_f(z,0)}{dz}\right.$$
$$- \int_0^z [B_r(z') - B_r(z)]\frac{\partial^2 \bar{T}_f(z,z')}{\partial z\,\partial z'}\,dz'$$
$$\left. - \int_z^\infty [B_r(z') - B_r(z)]\frac{\partial^2 \bar{T}_f(z,z')}{\partial z\,\partial z'}\,dz'\right\}. \tag{2.5.5}$$

The four terms in this "exchange integral formulation" of the heating-rate equation represent the contributions to infrared heating at z due to the possible exchanges of photons between levels. The first term represents "exchange" with space. Since downward flux from space can be neglected, this term always contributes to *cooling*. The second term corresponds to exchange with the underlying surface. Since $d\bar{T}_f(z,0)/dz < 0$, it contributes to heating if $B_r(0_-) > B_r(z)$. Similarly, the last two terms represent contributions due to exchanges with underlying and overlying layers and contribute to heating wherever $B_r(z') > B_r(z)$. Note that $\partial^2 T_f/\partial z\,\partial z'$ is always negative or zero.

The essence of the exchange problem is expressed by the factor $\partial \bar{T}_f(z,z')/\partial z$. It is often convenient to express the exchange integral formulation in terms of a corresponding function that has been normalized to lie in the range 0–1. This normalization yields the function

$$\Gamma_r(z,z') = \frac{\Delta\nu_r}{2\rho_{a0}(z)\tilde{S}_r(z)}\left|\frac{\partial \bar{T}_f(z,z')}{\partial z}\right|$$
$$= \frac{1}{\tilde{S}_r(z)}\int_0^1 d\mu \int_{\Delta\nu_r} k_\nu(z)\exp[-\Delta\tau_\nu(z,z')/\mu]\,d\nu$$
$$= \frac{1}{\tilde{S}_r(z)}\int_{\Delta\nu_r} k_\nu(z)E_2[\Delta\tau_\nu(z,z')]\,d\nu. \tag{2.5.6}$$

The term $\Gamma_r(z,z')$ represents the probability that a photon emitted in band r between z and $z + dz$ will escape to level z' before being reabsorbed, and for this reason it is appropriately called the *escape function*. Note that, unlike $T_r(z,z')$, Γ_r is not symmetric in z and z', so that the order of its arguments is important. Examples of $\Gamma_r(z,z')$ are shown in Fig. 2.18. The term $\Gamma_r(z,z')$ decays monotonically away from z with an extremely sharp peak and a first-order discontinuity at z. For a gas whose concentration does not increase with height, $\Gamma_r(z,z')$ decreases more rapidly above than below z. As illustrated in Fig. 2.18, it generally has a small but finite value as $z \to \infty$,

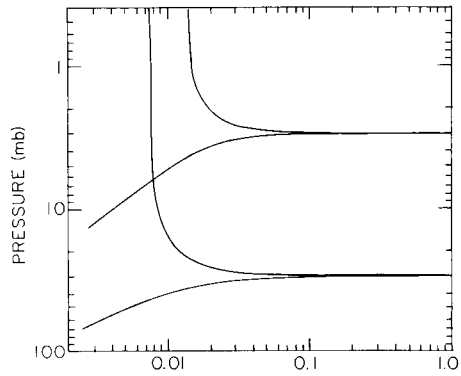

Fig. 2.18. Escape functions $\Gamma_r(z, z')$ for the 15-μm band of CO_2 centered at the 30 and 3 mb levels. [From Leovy (1984).]

corresponding to the probability of photon escape to space. In terms of Γ_r, Eq. (2.5.5) can be rewritten in the compact Stieltjes integral form,

$$h_r(z)\{[2\pi m_a(z)\tilde{S}_r(z)]^{-1}\,\Delta\nu_r\} = \int_{\substack{0\\ z'<z}}^{1} [B_r(z') - B_r(z)]\,d\Gamma_r(z, z')$$

$$+ \int_{\substack{0\\ z'>z}}^{1} [B_r(z') - B_r(z)]\,d\Gamma_r(z, z'), \tag{2.5.7}$$

where m_a is the absorber mass mixing ratio, and it is understood that $B_r(z') = B_r(0_-)$ for $\Gamma_r(z, z') \leq \Gamma_r(z, 0)$ in the first integral and $B_r(z') = 0$ for $\Gamma_r(z, z') \leq \Gamma_r(z, \infty)$ in the second integral, so that the boundary terms are incorporated in the integrals.

2.5.2 Approximations for the Exchange Integrals

It is evident that, because of the sharply peaked character of the escape function and the absence of radiation returned from space, the dominant contribution to $h_r(z)$ will often be the radiation-to-space term,

$$h_r(z) \approx 2\pi m_a(z)S_r(z)\,\Delta\nu_r^{-1}B_r(z)\Gamma_r(z, \infty)$$

$$= [\pi/\rho_0(z)]B_r(z)\frac{d\bar{T}_f}{dz}(z, \infty). \tag{2.5.8}$$

Rodgers and Walshaw (1966) have shown that, except close to the lower boundary, or in regions of large curvature of the vertical profile of $B_r(z)$,

Eq. (2.5.8) is a remarkably accurate approximation for both water vapor and CO_2. Thus, under a wide range of circumstances, the exchange terms can be neglected and $h_r(z)$ can be represented by Eq. (2.5.8). This approximation is called the *cool-to-space approximation.* Suppose that the necessary conditions for validity of this equation hold (sufficient distance from the lower boundary and sufficiently small temperature-profile curvature), and a dynamical disturbance produces a small local perturbation T' from an equilibrium temperature T_e. The temperature T_e may have been maintained by a balance between nonradiative as well as radiative terms. If the curvature of the vertical T' profile is sufficiently small, and if T' itself is small enough to permit linearization of the Planck function, then

$$\left(\frac{\partial T'}{\partial t}\right)_{\text{rad}} \approx -\frac{\pi}{\rho_0(z)c_p}\left\{\sum_r \left(\frac{dB_r}{dT}\right)_{T=T_e}\left[\frac{d\bar{T}_f(z,\infty)}{dz}\right]\right\} T' \equiv -K_{\text{rad}}(z, T_e)T', \tag{2.5.9}$$

where the summation over r includes all relevant spectral bands. This simple approximation is known as the *Newtonian cooling approximation,* and $K_{\text{rad}}(z, T_e)$ is the *Newtonian cooling coefficient.*

Unfortunately, above the stratopause, the radiation-to-space approximation breaks down for the 15-μm bands of CO_2, and net cooling or heating due to these bands is the small difference between cooling due to radiation to space and heating due to exchange with underlying layers (Fig. 2.19). At these altitudes, the CO_2 bands have become sufficiently transparent that mesospheric layers can "see" the distant warm stratopause.

Nevertheless, the applicability and simplicity of the cool-to-space approximation, which depends only on the *local* source function, suggest

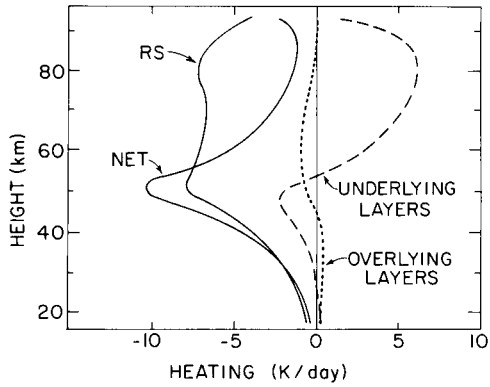

Fig. 2.19. Contributions of radiation to space (RS) and exchanges with underlying and overlying layers to the net cooling of the tropical middle atmosphere. [From Leovy (1984).]

the substitution of a Taylor-series expansion of B_r in the integrals of Eq. (2.5.7) in order to obtain more accurate local approximations in terms of B_r and its derivatives. The result is

$$h_r(z) = 2\pi m_a(z)\tilde{S}_r(z)\,\Delta\nu_r^{-1}\left\{-B_r(z)\Gamma_r(z,\infty) + [B_r(0_-) - B_r(z)]\Gamma_r(z,0) + \sum_{m=1}^{\infty}\frac{1}{m!}[(-1)^m l_{d,r}^m + l_{u,r}^m]\frac{d^m B_r}{dz^m}\right\} \tag{2.5.10a}$$

where

$$l_{d,r}^m = \int_{\Gamma_r(z,0)}^{1} |z' - z|^m\, d\Gamma_r(z,z'), \qquad l_{u,r}^m = \int_{\Gamma_r(z,0)}^{1} (z' - z)^m\, d\Gamma_r(z,z') \tag{2.5.10b}$$

are the mth moments of effective radiation lengths downward and upward from level z in band r.

If the atmosphere is sufficiently opaque both upward and downward that both radiation to space and radiation to the underlying surface can be neglected, the summation in Eq. (2.5.10a) converges rapidly. Moreover, the first moments $l_{d,r}^1$ and $l_{u,r}^1$ may be approximately equal and tend to cancel each other. In this case, the most important term in the series is

$$\tfrac{1}{2}[l_{d,r}^2 + l_{u,r}^2]\frac{d^2 B_r}{dz^2} \approx \tfrac{1}{2}[l_{d,r}^2 + l_{u,r}^2]\frac{dB_r}{dT}\frac{d^2 T}{dz^2}$$

[neglecting a term containing $(d^2B_r/dT^2)(dT/dz)^2$], and the total infrared net heating rate due to r radiatively active bands is approximately

$$h(z) \equiv \sum_r h_r(z) \approx \pi m_a(z)\left\{\sum_r \tilde{S}_r(z)\,\Delta\nu_r^{-1}[l_{d,r}^2 + l_{u,r}^2]\frac{dB_r}{dT}\right\}\frac{d^2 T}{dz^2}. \tag{2.5.11}$$

Equation (2.5.11) corresponds to the "diffusion approximation" to the radiative heating rate. Its contribution is important if the atmosphere is very opaque upward and downward and local curvature of the vertical temperature profile is large, for example, near inversion bases and tops, and near the tropopause or mesopause.

In the case of radiative exchange by CO_2 in the mesosphere, the upward and downward effective radiation lengths $l_{d,r}^1$and $l_{u,r}^1$ are very different. Since $[1 - \Gamma_r(z,\infty)]$ is small in the mesosphere, $l_{d,r}^1 > l_{u,r}^1$, and the first derivative term in the series of Eq.(2.5.10a) cannot be neglected. This is why the term corresponding to exchange with underlying layers is so large in the mesosphere in Fig. 2.19.

Another limiting regime occurs if the atmosphere is opaque upward, but transparent downward, and there is a substantial temperature difference between level z and the lower boundary. In this case, the contribution of exchange with the underlying surface can be of equal or greater magnitude than radiation to space, so that, approximately,

$$h(z) \approx -2\pi m_a(z) \sum_r (\tilde{S}_r(z)\Delta\nu_r^{-1}\{B_r(z)\Gamma_r(z,\infty) - [B_r(0_-) - B_r(z)]\Gamma_r(z,0)\}). \tag{2.5.12}$$

This approximation applies to radiative transfer by ozone in the 9.6-μm band in the lowest part of the stratosphere. Since there is very little ozone below the lower stratosphere, the second term in Eq. (2.5.12) is dominant there. It produces a net heating, since generally $B_r(0_-) > B_r(z)$ for z in the lower stratosphere. However, this heating rate is very sensitive to the effective radiative temperature of the lower boundary, and hence to the height, emissivity, and coverage of clouds in the troposphere. Above about 25 km, the atmosphere begins to become more transparent upward than downward in the 9.6-μm band, with the result that cooling to space [the first term in Eq. (2.5.12)] dominates and the band heating rate becomes negative.

In practical calculations of h_r, the integrals in Eq. (2.5.4) are represented by quadratures. The term $B_r(z')$ is represented by an interpolation formula with the general form

$$B_r(z') = \sum_j a_j(z', z_j) B_r(z_j),$$

where the quantities $a_j(z', z_j)$ are suitable interpolation functions for the discrete set of levels z_j whose values increase with j. Then

$$\begin{aligned} h_r(z_i) &= \sum_j R_{ij}(z_i, z_j) B_r(z_j) \\ &= \left\{ \sum_j R_{ij} B_r(z_i) + \sum_{j<i} R_{ij}[B_r(z_j) - B_r(z_i)] \right. \\ &\quad \left. + \sum_{j>i} R_{ij}[B_r(z_j) - B_r(z_i)] \right\}, \end{aligned} \tag{2.5.13}$$

where

$$R_{ij}(z_i, z_j) = [\pi/\rho_0(z_j)] \int a_j(z', z_j) \frac{\partial^2 \bar{T}_f(z_i, z')}{\partial z \, \partial z'} dz'.$$

The quantities R_{ij} are elements of a square matrix called the *Curtis matrix*. The first form of Eq. (2.5.13) corresponds to Eq. (2.5.4), and the second to the exchange form of Eq. (2.5.5), with the first term corresponding to

radiation to space, the second to exchange with the underlying layers and the ground, and the third to exchanges with overlying layers. Curtis matrices have been applied to the 15-μm CO_2 bands and used to calculate middle atmosphere cooling rates by several investigators. As a consequence of the sharply peaked character of the escape functions, particularly close attention must be paid to the quadrature treatment of the Planck-function profile in evaluating contributions to R_{ij} from layers adjacent to the one for which heating is being calculated. Quadrature errors are likely to be largest in the mesosphere, where exchange with underlying layers is important.

The Curtis matrix elements give directly the heating rate response to a unit Planck-function change in any other layer. By expressing B_r in the perturbation form,

$$B_r(T) = B_r(T_e) + \left(\frac{dB_r}{dT}\right)_{T_e} \delta T, \tag{2.5.14}$$

one can also assess quite directly the radiative damping rate for small temperature perturbations of arbitrary shape (Fig. 2.20). In general, damping rate decreases with increasing vertical scale of temperature perturbations, reaching its smallest value when the entire atmospheric column is perturbed by the same amount. The damping rate per kelvin of temperature perturbation in this case is the Newtonian cooling coefficient.

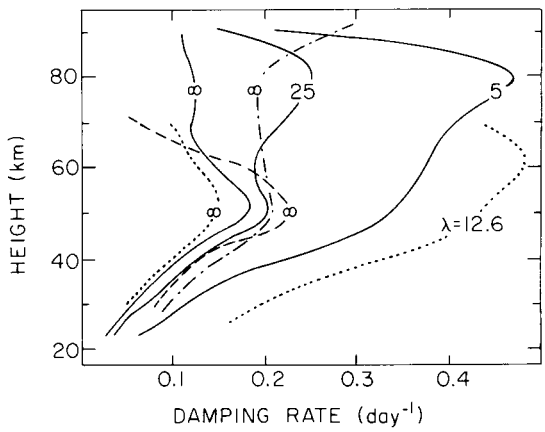

Fig. 2.20. Damping rates for the 15-μm band for temperature perturbations from the standard atmosphere: Wehrbein and Leovy (1982, thin solid), Dickinson (1973, dashed), Fels (1982, dotted), Apruzese *et al.* (1982, dash-dot). Curves are for radiation to space (∞) and for 5- and 25-km "boxcar" temperature perturbations. Also shown is the damping for a sinusoidal disturbance of vertical wavelength λ = 12.6 km. [From Leovy (1984), with permission.]

An empirical estimate of the Newtonian cooling coefficient has been obtained by Ghazi *et al.* (1985) by combining observed temperature and ozone fluctuations with corresponding detailed calculations of heating rate. They inferred a vertical profile of K_{rad} with a maximum of 0.15 $(day)^{-1}$ between 40 and 45 km, generally similar to the dotted curve marked (∞) in Fig. 2.20. They also found that temperature correlated ozone fluctuations arising from temperature-dependent photochemistry contribute an additional effective temperature damping rate of as much as 0.12 $(day)^{-1}$ in the lower mesosphere.

2.5.3 Fourier Representation of Radiative Damping

An alternative and more widely applicable approach to the problem of scale dependent radiative damping follows a suggestion of Spiegel (1957). Small temperature perturbations, linearized with respect to the Planck function as in Eq. (2.5.14), can be expanded in Fourier series in the spatial coordinates in order to derive a perturbation heating rate as a function of wave number. This approach has been applied specifically to a plane-parallel atmosphere by Sasamori and London (1966), and subsequently justified by Fels (1982), who demonstrated that conditions for its validity correspond to those of an extended form of the *WKBJ* approximation. Specifically, the basic state properties must vary slowly in the vertical in comparison with m^{-1}, the local inverse vertical wave number. Moreover, it is necessary that $m^{-1} < 2H$, where H is the scale height. These conditions are satisfied for most internal gravity waves and the diurnal tidal modes in the middle atmosphere.

The scale-dependent radiative damping time $\tau_R(m, z)$ is defined by

$$\frac{\partial \hat{T}(m, z)}{\partial t} \approx -\tau_R(m, z)^{-1} \hat{T}(m, z) \tag{2.5.15}$$

where $\hat{T}$ is the complex Fourier amplitude of the component of the temperature perturbation with vertical wave number m. The dependence on height indicated in Eq. (2.5.15) is in the slowly varying sense of the *WKBJ* approximation. Inverse damping time τ_R^{-1} assumes a particularly simple form when the wavelength is short, so that the *WKBJ* approximation is well satisfied and the boundary terms can be neglected.

Fels (1984) has calculated τ_R^{-1} for the 15-μm CO_2 band using Eq. (2.5.15) for disturbances of short vertical wavelength in the mesosphere and using a slightly more general expression that accounts for boundary effects and line overlap for stratospheric disturbances. His results for the standard atmosphere temperature profile are shown in Fig. 2.21. For O_3, the maximum

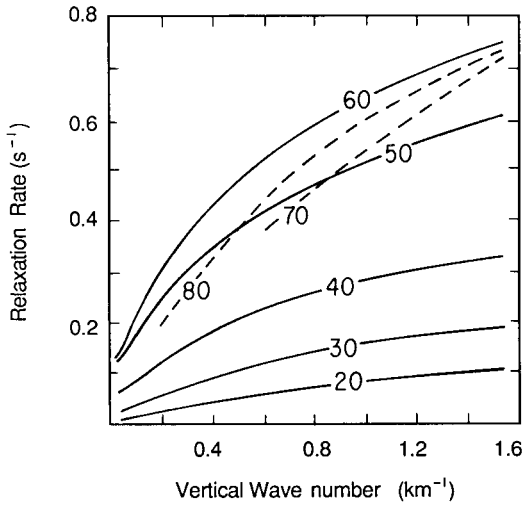

Fig. 2.21. Dependence of radiative damping rates at several altitudes (given in km) on vertical wavelength. The solid curves have been replotted from Fels (1984), and the dashed curves are from Fels (1982).

damping rate is reached near the stratopause. In the upper stratosphere and mesosphere, damping due to O_3 infrared exchange is independent of wavelength for moderate and short wavelengths above the stratopause. This behavior corresponds to the *optically thin limit* in which ozone is essentially transparent for distances comparable to these short wavelengths. For CO_2, which is much more opaque, damping rate increases with increasing m, rapidly at first, and then more slowly, and for fixed m it reaches a maximum in the lower mesosphere. In this limit,

$$\tau_R^{-1} \to \frac{4\pi\rho_a}{c_p\rho}(dB_r/dT)\sum_i S_i.$$

In the CO_2 calculations shown in Fig. 2.21, Fels has taken departures from local thermodynamic equilibrium into account at 70 and 80 km using the two-level model formulation that will be described in the next section. Non-LTE effects are largely responsible for the upward decrease in damping rate above a lower mesosphere maximum.

2.6. Departure from Local Thermodynamic Equilibrium

If local thermodynamic equilibrium (LTE) prevailed at all altitudes, unimpeded radiation to space in the centers of the strong Doppler lines of the ν_2 fundamental of CO_2 would cool the atmosphere very strongly.

In the optically thin limit, the heating rate (in $K\,s^{-1}$) is given approximately by the radiation-to-space term from Eq. (2.5.8),

$$h_r(z)/\rho \approx -\frac{2\pi m_a}{c_p} B_r(z)\tilde{S}_r\Gamma_r(z,\infty)\,\Delta\nu_r^{-1}$$

$$\approx -\frac{2\pi m_a}{c_p} B_r(z)\tilde{S}_r\,\Delta\nu_r^{-1},$$

since $\Gamma_r(z,\infty) \to 1$ as $z \to \infty$. Using the CO_2 mixing ratio and the ν_2 fundamental band strength from Table 2.1, this rate of cooling exceeds 100 K day^{-1} at typical lower-thermosphere temperatures. These large hypothetical cooling rates do not occur because below the altitude at which the optically thin limit is reached, the rate of collisional transfer from kinetic to vibrational energy limits energy loss. As a result, excited vibrational levels at these altitudes are not populated according to the Boltzmann distribution, Kirchhoff's Law breaks down, and the source function departs strongly from the Planck function. Cooling rates at and above the mesopause are smaller than this optically thin LTE limit by more than a factor of 10. In fact, the rapid increase in temperature above the mesopause is attributable largely to the rapid decrease in radiative cooling efficiency above that level. The non-LTE behavior of CO_2 influences mesopause temperature structure on Venus and Mars as well as on Earth. In this section, we develop the non-LTE formulation in terms of the Einstein coefficients and consider two specific non-LTE models.

2.6.1 *The Einstein Coefficients*

The interaction between radiation and matter can be described in terms of three fundamental processes: *spontaneous emission*, *absorption*, and *induced emission* (Fig. 2.22). The last, the process responsible for lasing, yields induced photons identical in phase, polarization, and direction of

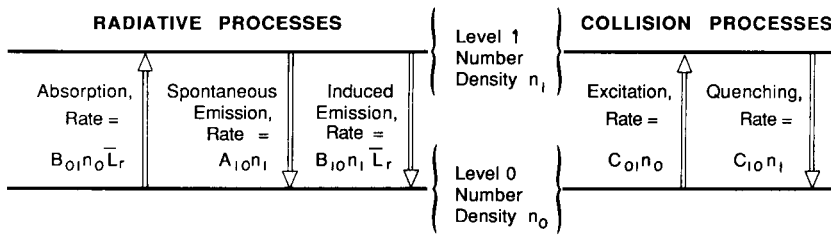

Fig. 2.22. Radiative and collisional transitions connecting the ground state and lowest vibrational level of a molecule.

travel to the incident photons. Consider a vibration–rotation transition with upper vibrational level 1, molecular population n_1, and ground-state level 0, population n_0, for an absorbing gas whose total number density is n_a. The rates of photon emission and absorption per unit volume are proportional to n_1 and n_0, and in the cases of absorption and induced emission, they are also proportional to the band and angular average radiance,

$$\bar{L}_r = \frac{1}{4\pi S_r}\int_{4\pi}\int_{\Delta\nu_r} \sigma_\nu L_\nu \, d\nu \, d\Omega \equiv \frac{1}{4\pi}\int_{4\pi}\int_{\Delta\nu_r} \tilde{f}(\nu) L_\nu \, d\nu \, d\Omega, \quad (2.6.1)$$

where $\tilde{f}(\nu)$ is a generalized "band-shape factor," which takes into account rotational structure as well as line shape. The proportionality constants are the *Einstein coefficients* A_{10}, B_{01}, and B_{10}, defined such that

$$\begin{aligned} A_{10}n_1 &= \text{rate of spontaneous emission,} \\ B_{01}n_0\bar{L}_r &= \text{rate of absorption,} \\ B_{10}n_1\bar{L}_r &= \text{rate of induced emission,} \end{aligned} \quad (2.6.2)$$

with each of these terms expressed in units of photons $m^{-3}\,s^{-1}$. Thus, A_{10} is the spontaneous emission probability per molecule. Each of these coefficients depends on the quantum-mechanical details of the transition but is independent of the properties of the radiation field or the thermodynamic state of the gas.

The volume heating rate for the band is equal to the rate of decrease of monochromatic radiance with distance, $-dL_\nu/ds$, integrated over all frequencies in the band and all solid angles. This can readily be shown from the definition of h_r or from the heating-rate equation in the form of Eq. (2.5.3). Hence, applying the radiative transfer equation [Eq. (2.2.5)], the heating rate per unit volume is

$$\rho h_r = -\int_{4\pi}\int_{\Delta\nu_r} \frac{dL_\nu}{ds} \, d\nu \, d\Omega = 4\pi S_r n_a(\bar{L}_r - J_r). \quad (2.6.3)$$

For the spectrally narrow bands of interest, frequency in the band can be approximated by the constant value ν_r. Then ρh_r can also be expressed in terms of the Einstein coefficients,

$$\rho h_r = h\nu_r(B_{01}n_0\bar{L}_r - A_{10}n_1 - B_{10}n_1\bar{L}_r). \quad (2.6.4)$$

If the gas is in complete thermodynamic equilibrium, then $h_r = 0$, $\bar{L}_r$ is the Planck function, and the ratio n_1/n_0 corresponds to the Boltzmann distribution,

$$n_1/n_0 = g_{10}e^{-h\nu_r/k_bT} \quad (2.6.5)$$

where $g_{10} \equiv g_1/g_0$, the degeneracy ratio. For the ν_2 fundamental of CO_2, $g_{10} = 2$. It follows from Eq. (2.6.4) that

$$B_{01}/B_{10} = g_{10}$$

and

$$A_{10} = \frac{2h\nu_r^3}{c^2} B_{10} = \frac{2h\nu_r^3}{c^2 g_{10}} B_{01}. \tag{2.6.6}$$

These relations hold under nonequilibrium as well as equilibrium conditions, since the Einstein coefficients are independent of the state of the gas or the radiation field. This is an application of the *principle of detailed balance.*

Comparison of Eqs. (2.6.3) and (2.6.4) shows that

$$S_r = \frac{h\nu_r}{4\pi} B_{01}(n_0/n_a)[1 - g_{10}^{-1}(n_1/n_0)] \simeq \frac{h\nu_r}{4\pi} B_{01}, \tag{2.6.7}$$

under nonequilibrium as well as equilibrium conditions, or, from Eq. (2.6.6),

$$A_{10} \approx \frac{8\pi\nu_r^2}{g_{10}c^2}\left(\frac{n_a}{n_0}\right)[1 - g_{10}^{-1}(n_1/n_0)]^{-1} S_r \approx \frac{8\pi\nu_r^2}{g_{10}c^2} S_r. \tag{2.6.8}$$

Moreover, with the aid of Eqs. (2.2.10) and (2.6.6),

$$J_r = \left(\frac{h\nu_r A_{10} n_1}{4\pi S_r n_a}\right)\frac{[1 - e^{-h\nu_r/k_b T}]}{[1 - g_{10}^{-1}(n_1/n_0)]} B_r\left[\left(\frac{n_1}{n_0}\right)\left(\frac{n_{0eq}}{n_{1eq}}\right)\right] \simeq B_r\left(\frac{n_1}{n_{1eq}}\right), \tag{2.6.9}$$

where n_{1eq} and n_{0eq} are thermal equilibrium number densities. In Eqs. (2.6.7), (2.6.8) and (2.6.9), S_r, A_{10}, and J_r have been approximated by dropping terms of order $\exp(-h\nu_r/k_b T)$. For the ν_2 fundamental of CO_2 these terms are smaller than the retained terms by a factor of order 100 under normal atmospheric conditions. Neglect of these terms is equivalent to ignoring induced emission, and they will be neglected throughout the subsequent development. Note that Eq. (2.6.8) shows how the emission probability per molecule, A_{10}, is related to the measured band strength.

Equation (2.6.9) shows that the source function for the band is proportional to the ratio of the actual number density in the excited state to the equilibrium number density. Under LTE conditions, $n_1 = n_{1eq}$, and Kirchhoff's Law holds. In the more general case, the problem of determining the source function reduces to that of determining n_1.

2.6.2 *The Two-Level Model*

Under LTE conditions, the rate of population of level 1 by collisions that convert translational kinetic energy to vibrational energy (excitation) is exactly balanced by the reverse process (quenching), collisional conversion of level-1 vibrational energy to translational kinetic energy (see Fig. 2.22). These rates can be represented by $C_{01}n_0$ for the first process and $C_{10}n_1$ for the second. The kinetic coefficients C_{01} and C_{10} are both proportional to molecular number densities, and their ratio can be determined from application of the detailed balance principle by setting $(n_1/n_0) = (n_{1eq}/n_{0eq})$. At equilibrium,

$$C_{01} = C_{10}g_{10}e^{-h\nu_r/k_bT}, \tag{2.6.10}$$

where the collision parameter C_{10} is

$$C_{10} = k_0\eta n, \tag{2.6.11}$$

with k_0 the molecular collision frequency, η the fraction of collisions responsible for vibrational–translational (V-T) energy conversion, and n the total number density of all gas molecules. Equation (2.6.10) holds under nonequilibrium as well as equilibrium conditions, but C_{10} is a function of temperature.

The simplest non-LTE model is the *two-level model*, in which only collisional and radiative interactions between level 1 and the ground state are considered. Under LTE conditions, the collisional rates are much faster than the radiative rates, so that the collisional rates are very nearly in steady-state balance. Under non-LTE conditions this is no longer the case, but a very close balance exists between the sum of radiative and collisional rates tending to populate and depopulate level 1. As shown in Fig. 2.22, this balance is

$$(A_{10} + C_{10})n_1 \approx (B_{01}\bar{L}_r + C_{01})n_0. \tag{2.6.12}$$

Solving for (n_1/n_0), making use of Eqs. (2.6.5), (2.6.6), (2.6.9), and (2.2.10), and neglecting terms of order $\exp(-h\nu_r/k_bT)$ gives

$$J_r = \frac{\bar{L}_r + C_{01}/B_{01}}{1 + C_{10}/A_{10}} = \frac{\bar{L}_r + \phi B_r}{1 + \phi}, \qquad \phi \equiv C_{10}/A_{10}. \tag{2.6.13}$$

The behavior of the source function is controlled by the ratio of the time constant for radiative deexcitation of level 1, A_{10}^{-1}, to the time constant for collisional deexcitation, C_{10}^{-1}. For large ϕ, $J_r \to B_r$ and Kirchhoff's Law applies, but for $\phi \to 0$, $J_r \to \bar{L}_r$; the source function reduces to the source function for isotropic conservative scattering.

For the ν_2 fundamental of CO_2, $A_{10} = 1.51\ s^{-1}$. Because conversion between kinetic and vibrational energy is an improbable event, only about one collision in 10^5 is effective in deexciting level 1, that is, $\eta \approx 10^{-5}$. Since $k_0 \approx 2 \times 10^{-16}\ m^3\ s^{-1}$, this gives

$$\phi \approx \frac{2 \times 10^{-21} n}{1.51}$$

(with n in molecules m^{-3}), so that the transition between LTE and non-LTE regimes centers around the level at which $n \approx 0.75 \times 10^{21}\ m^{-3}$, or 75 km. This is the *vibrational relaxation level* in the earth's atmosphere.

The effect of vibrational relaxation on the heating rate can be made clear by substituting Eq. (2.6.13) into Eq. (2.6.3):

$$\rho h_r = 4\pi S_r n_a (\bar{L}_r - J_r) = \frac{4\pi S_r n_a \phi}{(1+\phi)} (\bar{L}_r - B_r). \tag{2.6.14}$$

For large ϕ (LTE), h_r is proportional to $(\bar{L}_r - B_r)$, but as $\phi \to 0$, $h_r \to 0$. The decoupling between the radiation field and the kinetic energy of the gas is responsible for the vanishing infrared cooling rate at altitudes far above the vibrational relaxation level.

To see this behavior more clearly, assume that the radiation-to-space approximation applies. Then

$$\rho h_r(z) = -2\pi S_r n_a(z) J_r(z) \Gamma_r(z, \infty).$$

But eliminating $\bar{L}_r$ between Eqs. (2.6.13) and (2.6.14) gives

$$J_r = B_r + \frac{\rho h_r}{4\pi S_r n_a \phi}, \tag{2.6.15}$$

so that

$$J_r = B_r / [1 + \tfrac{1}{2}\Gamma_r(z, \infty)\phi^{-1}], \tag{2.6.16}$$

and

$$h_r = -\frac{2\pi S_r \rho^{-1} n_a \Gamma_r(z, \infty) B_r}{1 + \tfrac{1}{2}\Gamma_r(z, \infty)\phi^{-1}}. \tag{2.6.17}$$

Thus, in the radiation-to-space approximation, vibrational relaxation is controlled not by ϕ^{-1}, but by $\frac{1}{2}\Gamma_r(z, \infty)\phi^{-1}$. If the atmosphere is sufficiently opaque, $\Gamma_r(z, \infty)$ is small and excited-state populations can be maintained near their equilibrium values by radiation even if ϕ is small. For the ν_2 fundamental of CO_2, the level at which $\frac{1}{2}\Gamma_r(z, \infty)\phi^{-1} \approx 1$ occurs about 10 km above the level at which $\phi^{-1} \approx 1$, so that, for this band, the source function tends to equal the Planck function up to about 80–85 km (Fig. 2.23). At

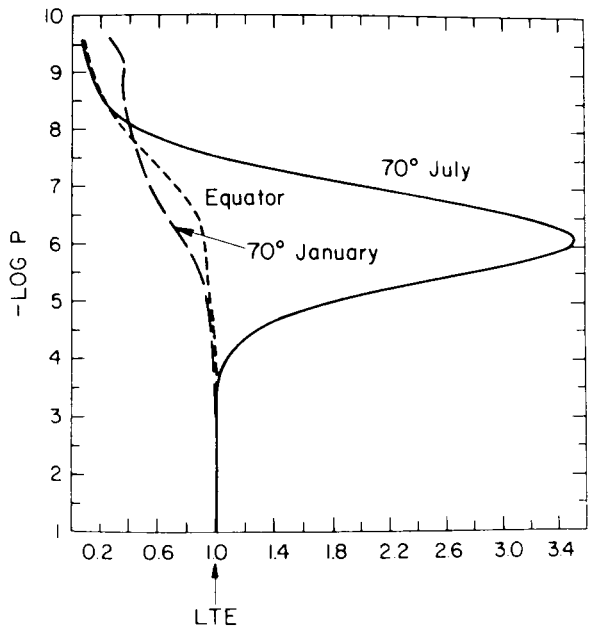

Fig. 2.23. Non-LTE source function normalized by the Planck function for the transition 01^10-000 of $^{12}C^{16}O_2$ for three combinations of latitude and season. The ordinate is $-\log$(pressure in mb) and has the following approximate relationship to altitude: 0, 47 km; 2, 63 km; 4, 76 km; 6, 87 km; 8, 98 km. [From Dickinson (1984), with permission.]

very high altitudes, the gas becomes transparent, $\Gamma_r(z, \infty) \to 1$, and $\frac{1}{2}\Gamma_r(z, \infty)\phi^{-1}$ becomes large. Then

$$h_r \to -4\pi S_r \rho^{-1} n_a \phi B_r = -\tfrac{1}{2} g_{10} \frac{c^2}{\nu_r^2} \rho^{-1} n_a C_{10} B_r$$

$$\approx -h\nu_r \rho^{-1} C_{10} g_{10} n_0 e^{-h\nu_r/k_b T} = -h\nu_r C_{01} n_0. \qquad (2.6.18)$$

In this limit, the rate of cooling is just $h\nu_r$ times the rate of collisional excitation of level 1. Both the volume heating rate and the heating rate per unit mass vanish as $z \to \infty$.

The two-level non-LTE problem can be posed in the form of an integral equation. As described by Houghton (1977), this integral equation can be solved for the source function by expressing the heating rate integral in the Curtis matrix forms derived from Eq. (2.5.13),

$$h_r(z_i) = \sum_j R_{ij} J_r(z_i),$$

which can be expressed in the matrix form,

$$\mathbf{h}_r = \mathbf{R}\mathbf{J}. \qquad (2.6.19)$$

In matrix notation Eq. (2.6.15) is

$$\mathbf{J}_r = \mathbf{B}_r + \mathbf{E}\mathbf{h}_r, \tag{2.6.20}$$

where $\mathbf{E}$ is a diagonal matrix of dimension equal to the number of columns in $\mathbf{R}$. The elements of $\mathbf{E}$ are

$$E_{ij} = [4\pi S_r n_a(z_i)\phi(z_i)]^{-1}\rho\delta_{ij}. \tag{2.6.21}$$

Combining Eqs. (2.6.19) and (2.6.20) gives

$$\mathbf{J}_r = [\mathbf{I} - \mathbf{E}\mathbf{R}]^{-1}\mathbf{B}_r, \tag{2.6.22}$$

or

$$\mathbf{h}_r = [\mathbf{I} - \mathbf{R}\mathbf{E}]^{-1}\mathbf{R}\mathbf{B}_r. \tag{2.6.23}$$

Equation (2.6.23) has been widely used to calculate heating rates under non-LTE conditions. In these applications, the cooling rate has been calculated for the entire 15-μm band system so that it is implicitly assumed that the hot and isotopic bands in this spectral region have the same source function as the fundamental. The source functions for these relatively weak bands are imperfectly coupled to the fundamental, however, so that contributions from the hot and isotopic bands are not accurately calculated by this method. In the region above the mesopause where CO_2 is transparent even in the strong line centers of the ν_2 fundamental, the cooling rate due to the fundamental dominates the total cooling, and the resulting error is not serious. Just below the mesopause, where non-LTE effects are important, the contributions of the hot and isotopic bands are large and the error can be significant. A model more complex than the two-level model is needed for this region. Such a model will be discussed in the next section.

Before leaving the two-level model, a comment on the role of rotational fine structure is needed. Throughout the preceding discussion, it has been implicitly assumed that the rotational-level populations are not affected by the interplay of radiative and kinetic processes that produce non-LTE conditions. As a consequence, Einstein coefficients were needed only for the vibrational transition as a whole, not for the individual rotational transitions comprising the fine structure. The fine structure of the band was assumed to be determined by the kinetic temperature of the gas alone. This major simplification was possible because collisional exchange between translational and rotational energy is very efficient, occurring at nearly every collision. As a consequence, the rotational energy levels remain in thermal equilibrium up to a level at which the density is $\sim 10^{-5}$ times the vibrational relaxation density, well above the level where cooling by CO_2 infrared emission ceases to play a significant role.

2.6.3 *Dickinson's Multilevel Model*

The processes considered in the last section can be summarized in the following energy-transfer steps:

$$CO_2(v_2 = 1) \leftrightarrows CO_2(\text{ground state}) + h\nu\,(15\ \mu\text{m}), \tag{2.6.24}$$

the fundamental radiative transitions, and

$$\text{Air} + CO_2(v_2 = 1) \leftrightarrows CO_2(\text{ground state}) + \text{air} + \text{KE}, \tag{2.6.25}$$

the fundamental V-T transitions, where KE is kinetic energy.

Adequate treatment of the hot bands requires at a minimum that the radiative and kinetic transitions involving the 100, 02^00, and 02^20 levels be taken into account. These levels are so closely spaced that collisional equilibration between them must be very rapid, as it is for the rotational levels. Consequently, they can be treated as a single level, $v_2 = 2$, with degeneracy 4. The most important transitions affecting the population of this level are the vibration-vibration (V-V) transitions

$$CO_2(v_2 = 2) + CO_2(\text{ground state}) \leftrightarrows 2CO_2(v_2 = 1), \tag{2.6.26}$$

the V-T transitions

$$\text{Air} + CO_2(v_2 = 2) \leftrightarrows CO_2(v_2 = 1) + \text{air} + \text{KE}, \tag{2.6.27}$$

and the radiative transition

$$CO_2(v_2 = 2) \leftrightarrows CO_2(v_2 = 1) + h\nu\,(15\ \mu\text{m}). \tag{2.6.28}$$

Because 15-μm band Doppler lines are well separated, the spectrum of this radiative transition is well separated from that of the fundamental, even though both occupy the same broad spectral interval. Additional interactions involving higher vibrational levels occur but are usually of minor importance.[2] Because little energy exchange is involved, the V-V transitions are rapid and the forward and backward transitions have nearly the same bimolecular rate constant, K_{VV}. On the other hand, the V-T exchanges involve large energy transfers and are very slow. The rate for the forward reaction of Eq. (2.6.27), K_{VT2}, is $\sim 10^{-5} k_0$, comparable with the rate K_{VT1} of the forward reaction of Eq. (2.6.25).

The fundamental isotopic bands are coupled to the fundamental of the principal isotope by V-V reaction of the type

$$\begin{aligned} &CO_2(v_2 = 1, \text{ main isotope}) + CO_2(\text{ground state, minor isotope}) \\ &\quad \leftrightarrows CO_2(\text{ground state, main isotope}) \\ &\qquad + CO_2(v_2 = 1, \text{ minor isotope}). \end{aligned} \tag{2.6.29}$$

Because the energy changes are again small, these reaction rates are also

[2] Excitation of higher vibrational levels by transformation of absorbed solar radiation may sometimes render these interactions important, however.

fast, and forward and backward reaction rates are nearly equal. In addition, the isotopic fundamental radiative transitions [Eq. (2.6.24)] and lowest-level V-T transitions [Eq. (2.6.25)] must be separately treated for each isotope. Isotopic hot bands are not important.

Dickinson (1984) has extended the two-level model to account for these additional processes. This involves the solution of a coupled set of integral equations that are generalizations of Eq. (2.6.12) and involve the number densities of the first two excited vibrational levels of $^{12}C^{16}O^{16}O$ and the first excited level of $^{13}C^{16}O^{16}O$ and $^{12}C^{16}O^{18}O$. For the collisional interaction between level 1 and the ground state, he considered the additional effect of atomic oxygen, which appears to exchange energy efficiently with vibrationally excited CO_2 and could be important above the mesopause.

Dickinson's calculated source functions for three latitudes for the ν_2 fundamental of $^{12}C^{16}O_2$ are shown in Fig. 2.23. In each case the source function is shown normalized by the local value of the Planck function. Throughout the winter hemisphere and in the tropics, these normalized source functions decrease with height above the level at which $\frac{1}{2}\Gamma_r(z, \infty)\phi^{-1} \approx 1$, in accordance with the radiation to space approximation [Eq. (2.6.16)]. At high latitudes in the summer hemisphere, the normalized source functions increase to a strong maximum near the mesopause before decreasing at still higher levels. This is a consequence of the extremely steep lapse rate in this region and the corresponding dominance of upwelling radiation from the warm stratopause region. This effect is more pronounced for the hot and isotopic bands than for the fundamental. The effect of this upwelling radiance on heating is illustrated in Fig. 2.24. The upwelling radiance is sufficient to produce net heating near the summer mesopause. Figure 2.25 shows the altitude–latitude distribution of CO_2 infrared cooling for the solstices as calculated by Dickinson. Cooling maxima occur near the stratopause and in the lower thermosphere, with the calculated magnitude of the latter dependent on the uncertain rate of V-T exchange with atomic oxygen, so these values are somewhat uncertain. Weak mesopause warming extends from the summer polar region into the tropics. This feature is sensitive to details of the vertical temperature profile.

Absorption of solar photons in near-infrared bands can result in a cascading of quanta into the $v_2 = 2$ level and from there into $v_2 = 1$ quanta or thermal energy via the processes represented by Eqs. (2.6.24)–(2.6.27). The efficiency with which these quanta can cascade to the $v_2 = 1$ level depends on rates of V-V transfer to N_2, O_2, and H_2O, as well as "leakage" via emission in the 4.3-μm band of CO_2 and the 6.3-μm band of H_2O. These processes were first decribed in detail by Houghton (1969). Williams (1971) has calculated that solar absorption by CO_2 produces heating of as much as 1 K day^{-1} near the mesopause.

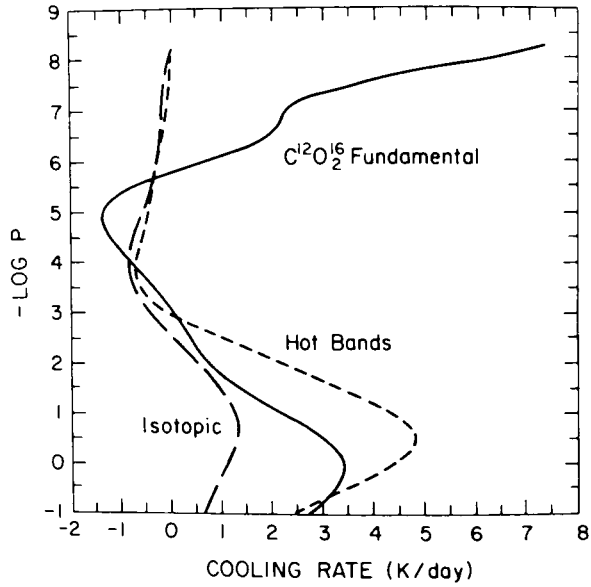

Fig. 2.24. Contributions of the $^{12}C^{16}O_2$ fundamental and the hot and isotopic bands to cooling rate for July at 70°N latitude. The ordinate scale is the same as in Fig. 2.23. [From Dickinson (1984), with permission.]

2.7 Absorption of Solar Radiation

So far, this chapter has emphasized emission, absorption and transfer of thermal infrared radiation, the process responsible for cooling the middle atmosphere. In the global mean, this is approximately balanced at each level by absorption of solar radiation.

From the direct solar beam, the rate of energy absorption per unit volume for a spectral interval $\Delta\nu_r$, $\rho h_r(z^*)$, follows from Eq. (2.2.16),

$$\rho h_r(z^*) = -\mu_0 \int_{\Delta\nu_r} S_{0\nu} \frac{d}{dz^*} e^{-\tau_\nu(z^*)/\mu_0}\, d\nu$$

$$= n_a(z^*) \int_{\Delta\nu_r} \sigma_\nu S_{0\nu} e^{-\tau_\nu(z^*)/\mu_0}\, d\nu. \tag{2.7.1}$$

This is closely related to the direct beam photodissociation rate per molecule,

$$P(z^*) = \int_{\nu > \nu_{diss}} e_\nu \sigma_\nu \tilde{S}_{0\nu} e^{-\tau_\nu(z^*)/\mu_0}\, d\nu, \tag{2.7.2}$$

where ν_{diss} is the dissociation threshold, e_ν is the quantum efficiency for photodissociation (frequently $e_\nu \approx 1$ for $\nu > \nu_{diss}$), and $\tilde{S}_{0\nu} \equiv S_{0\nu}/h\nu$ is the

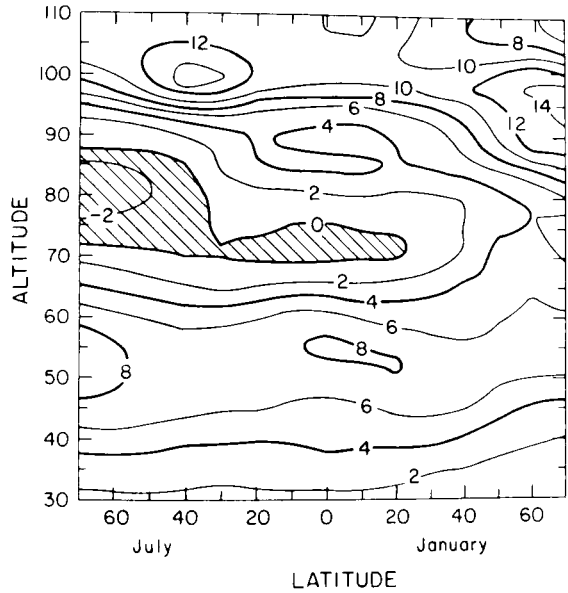

Fig. 2.25. Numbers on contours give total CO_2 15-μm band cooling rate in degrees Kelvin per day for the January and July 1972 COSPAR International Reference Atmospheres. [From Dickinson (1984), with permission.]

monochromatic solar flux density expressed in photons rather than energy units. If more than one gas absorbs in a spectral interval,

$$\rho h_r(z^*) = \sum_i n_{a,i} \int_{\Delta\nu_r} \sigma_{\nu,i} S_{0\nu} e^{-\tau_\nu(z^*)/\mu_0}\, d\nu, \tag{2.7.3}$$

where, in both Eqs. (2.7.2) and (2.7.3), τ_ν includes contributions from all absorbing gases (number densities $n_{a,i}$),

$$\tau_\nu(z^*) = \sum_i \int_{z^*}^{\infty} \sigma_{\nu,i} n_{a,i}\, dz^{*\prime}. \tag{2.7.4}$$

In order to see how heating per unit volume depends on frequency and height, consider the monochromatic version of Eq. (2.7.1) in an atmosphere whose scale height is constant and equal to H so that $z^* = z$ (see Section 1.1.1). The monochromatic volume heating rate ρh_ν is

$$\rho h_\nu(z) \equiv \frac{\rho\, dh_r}{d\nu} = n_a(z)\sigma_\nu S_{0\nu} e^{-\tau_\nu(z)/\mu_0}$$

$$= \sigma_\nu S_{0\nu} n_a(0) \exp[-z/H - H\sigma_\nu n_a(0)\mu_0^{-1} e^{-z/H}]. \tag{2.7.5}$$

This vertical distribution was first pointed out by Sydney Chapman, who first applied it in the explanation of ionized layers. We shall refer to it as *Chapman layer structure.* The monochromatic volume heating rate has a single maximum at the altitude at which $H\sigma_\nu n_a(z)/\mu_0 = 1$, that is, the altitude at which the slant optical path from outside the atmosphere reaches unity. The monochromatic heating rate at that level is

$$h_\nu(z_{max}) = \rho^{-1}\sigma_\nu S_{0\nu} n_a(z_{max}) e^{-1}. \tag{2.7.6}$$

It falls off as $e^{-z/H}$ above z_{max} due to the upward decrease of n_a, and it falls off below z_{max} at a much more rapid rate due to the exponential absorption. The altitude of the maximum increases with increasing zenith angle (decreasing μ_0), so both $n_a(z_{max})$ and $h_\nu(z_{max})$ decrease with increasing zenith angle.

According to Eq. (2.7.5), most of the absorption of solar radiation takes place within one or two scale heights of the layer maximum, z_{max}. Thus, a plot of z_{max} versus frequency (Fig. 2.26) illustrates the influence of different absorption processes on different regions of the atmosphere. It also illustrates the influence of solar photon frequency on different regions of the atmosphere. Since the emission altitude of photons in the solar atmosphere and the processes responsible for photon emission depend on frequency, there is a direct link between altitudes and processes in the solar atmosphere and altitudes and processes in the earth's atmosphere.

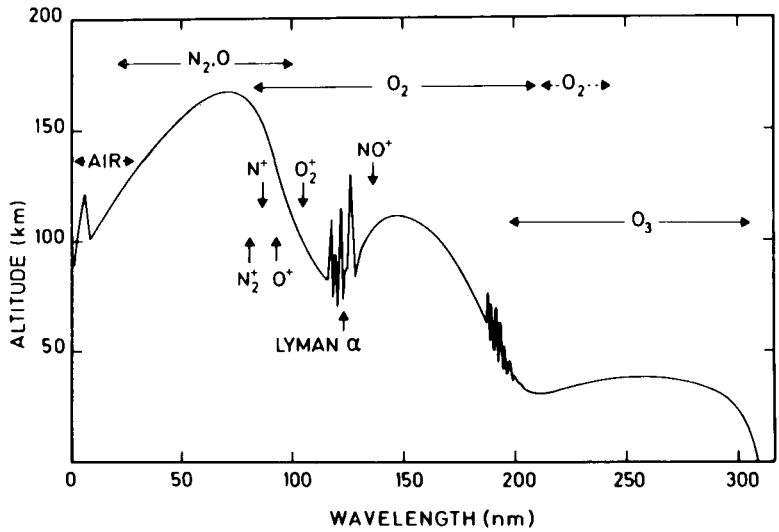

Fig. 2.26. Altitude of unit optical depth for normal incidence solar radiation. Principal absorbers and ionization thresholds are indicated. [From Herzberg (1965), with permission.]

At visible wavelengths ($\lambda > 310$ nm) solar radiation penetrates to the surface, but below about 310 nm in the ultraviolet, ozone absorption of solar radiation in a photodissociation continuum begins to shield the surface. This continuum absorbs most strongly at about 40 km and 250 nm, and it is responsible for shielding the surface from the biologically damaging radiation below 300 nm. Molecular oxygen absorbs in the Herzberg dissociation continuum below 240 nm, and oxygen becomes the dominant absorber below about 200 nm. The rate of absorption and consequent O_2 photodissociation near 200 nm is strongly dependent on the opacity due to ozone in the same spectral region. Between 175 and 200 nm, the Schumann-Runge bands are responsible for most absorption, and their complicated structure influences solar photon penetration in the mesosphere and upper stratosphere. The Schumann-Runge continuum controls solar photon penetration between 135 and 175 nm in the lower thermosphere and mesopause region.

Complex O_2 spectral features between 115 and 135 nm allow some solar radiation to penetrate to the upper mesosphere. A most important gap occurs at 121.6 nm, precisely the wavelength of hydrogen Lyman α, the strongest solar emission line. Because NO and alkali metals, which are present in trace amounts near the mesopause, ionize at wavelengths longer than 121.6 nm, this penetrating radiation is largely responsible for the formation of the D and lower E ionization layers in the upper mesosphere and lower thermosphere. X-rays and cosmic rays, which can also penetrate into the mesopause region, are responsible for the remainder of the ionization there. The bulk of the ionization in the earth's atmosphere is formed higher in the thermosphere, however, and is due to the ionization of the major gases at wavelengths between 10 and 100 nm.

2.7.1 Solar Radiation Flux

The information needed to calculate solar heating rates and photodissociation and ionization rates includes the spectral distribution of solar flux and its time variability, the molecular absorption cross sections, and the dissociation and ionization efficiencies. The relationship between the solar spectrum and the structure of the sun is well described by Brasseur and Solomon (1984), so only a brief account will be given here.

Figure 2.27 depicts the solar spectrum. Most solar radiant energy flux is emitted from the visible surface of the sun, the photosphere, at an effective blackbody temperature of about 6000 K. The solar spectrum at wavelengths longer than about 300 nm corresponds closely to a blackbody at this temperature. Temperature decreases upward through the photosphere to a minimum of about 4600 K at the base of the chromosphere, then rises to

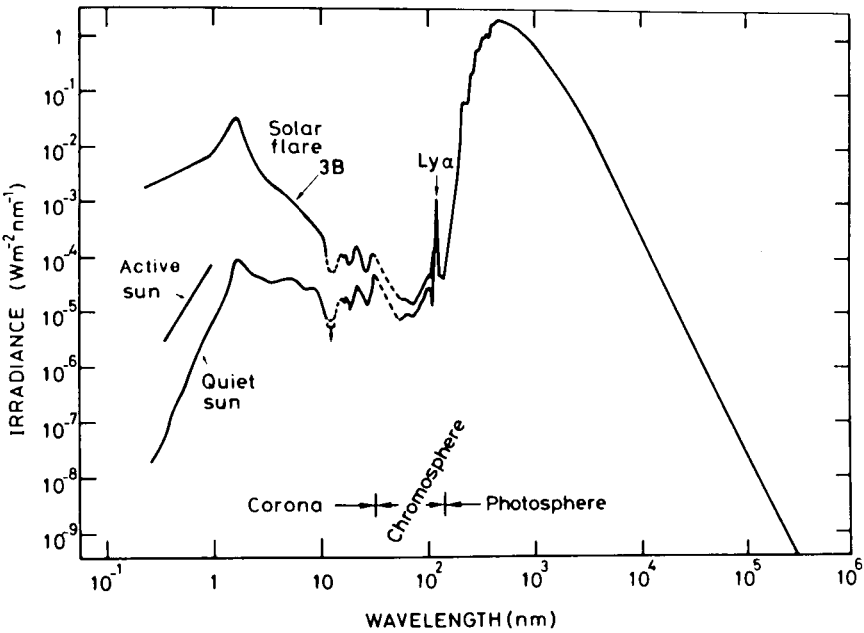

Fig. 2.27. Solar spectrum under quiet and active conditions and spectrum of an intense solar flare. [From Smith and Gottlieb (1974), with permission.]

10^6 K or more in the corona. Between 121.6 and 300 nm, the effective blackbody temperature of the solar spectrum reflects these lower temperatures between the photosphere and the base of the chromosphere. At 121.6 nm, the wavelength of Lyman α, and at shorter ultraviolet wavelengths, the solar spectrum is dominated by emission lines originating in the chromosphere and corona.

The variability of the solar atmosphere increases with increasing height, and as a result, the variability of the solar spectrum increases with decreasing wavelength. This is illustrated schematically in Fig. 2.27. Variability occurs on the time scales of the 26-day solar rotation, the 11-year sunspot cycle, and with a variety of short-lived solar disturbances, particularly flares. In the past, solar variability at ultraviolet wavelengths has been estimated from its correlation with solar flux at the radio wavelength 10.7 cm, which can be measured at the Earth's surface, but more recently ultraviolet variability has been monitored directly by satellites. At wavelengths affecting the thermal structure of the middle atmosphere (~160–700 nm), measured peak-to-peak variations in solar flux range from about 10% at 160 nm to about 5% at 200 nm. At wavelengths longer than 200 nm, measured solar variability drops rapidly and is less than 1% at 300 nm. However, the

variability may be somewhat greater than this, since available measurements do not yet cover a full solar cycle.

2.7.2 Absorption of Solar Radiation by Gases

Molecular oxygen absorption was discussed in Section 2.3.1, and absorption cross sections are shown in Figs. 2.7 and 2.8. Because of the complex structure of the Schumann-Runge bands and their temperature dependence, constant broadband absorption cross sections are not suitable. The World Meteorological Organization has provided tables of broadband transmission functions for this spectral region for the standard atmosphere temperature distribution. These nonexponential transmission functions take into account the spectral complexity of the bands. Photodissociation rates of several minor constituents in the upper stratosphere are sensitive to transmission in the Schumann-Runge spectral region, so it is important to have an accurate broadband description of this transmission. The photodissociation efficiency of O_2 is nearly unity at wavelengths shorter than the dissociation threshold at 242 nm.

Ozone absorption takes place in three dissociation continua in which dissociation efficiency is close to unity: the Hartley band from 200 to 310 nm, the Huggins bands, which blend with the Hartley band near 310 nm and extend to 350 nm, and the much weaker Chappuis bands extending from 440 to 800 nm (Fig. 2.28). The Hartley and Chappuis bands are smooth continua whose cross sections are independent of temperature and pressure. The Huggins bands have a diffuse banded structure (not shown in Fig. 2.28)

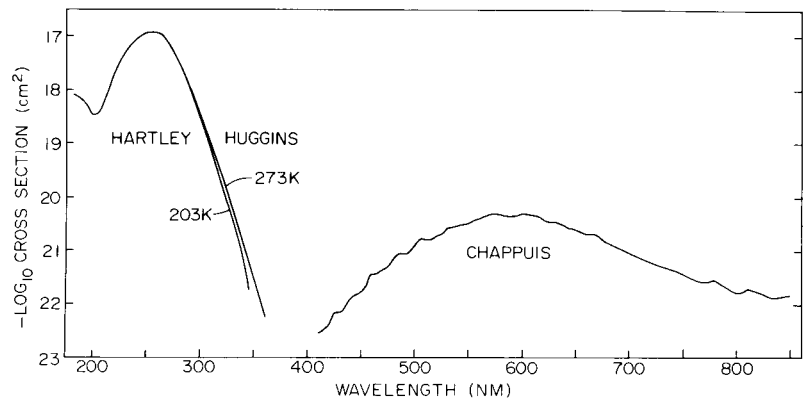

Fig. 2.28. Absorption spectrum of ozone. Note the temperature dependence in the Huggins bands. Weak band structure in this 310 to 350-nm spectral region has been suppressed in this presentation. Data from World Meteorological Organization (WMO, 1986).

with some temperature dependence. Band maxima are insensitive to temperature, but the minima show variations of up to 30% over the temperature range 200–290 K, with lower values at low temperatures. Despite the small absorption cross sections, the Chappuis bands are of great importance because they occur at the peak of the solar spectrum and absorb in the lower stratosphere and troposphere. Shorter wavelength radiation is nearly absent at these levels because of absorption higher up. Because of the Chappuis bands, ozone in sunlight is subject to rapid photodissociation right down to the surface.

Ultraviolet absorption by H_2O, NO_2, HNO_3, and many other gases is vital to the chemistry of the middle atmosphere but does not contribute significantly to heating, so these absorption cross sections will not be discussed in detail here. Readers are referred to Brasseur and Solomon and the report by the World Meteorological Organization (WMO, 1986). In general, gases with dissociation thresholds at wavelengths longer than about 300 nm are dissociated by the intense portion of the solar spectrum and are not shielded by overlying O_3 and O_2, so they dissociate rapidly in sunlight at all altitudes; lifetimes of individual molecules against dissociation are $\lesssim 10^3$ s. In addition to O_3, examples of species which dissociate rapidly in sunlight are NO_2, NO_3, and HOCl. On the other hand, molecules with dissociation thresholds at shorter wavelengths have relatively long dissociation lifetimes at all levels. Their dissociation rates decrease rapidly below the ozone layer and are also sensitive to zenith angle. Examples are H_2O, HNO_3, HCl, and O_2 (see Chapter 10).

If scattering is neglected, Eq. (2.7.1) can be used to calculate heating rates due to solar absorption by O_3 or O_2. However, this straightforward approach requires a spectral integration; for this reason, approximations involving only simple algebraic expressions have been worked out by Lindzen and Will (1973), Lacis and Hansen (1974), and Schoeberl and Strobel (1978). Errors in the approximation of Lacis and Hansen are $\lesssim 1\%$.

Absorption of solar radiation in the near infrared bands of CO_2 and water vapor makes a small but significant contribution to heating in the stratosphere. The most important bands of CO_2 are centered at 4.3, 2.7, and 2.0 μm. Water vapor has bands centered at 2.7, 1.9, 1.6, and 1.1 μm, together with a series of very weak bands extending to 0.55 μm in the visible. Because of its low concentration, water vapor absorbs much less solar radiation in the stratosphere than does CO_2. Heating rates for these gases can be calculated from the expression

$$h_r(z^*) = -\rho^{-1} S_{0,r} \frac{dW_r}{dz^*}(z^*, \mu_0), \tag{2.7.7}$$

where $W_r(z^*, \mu_0)$ is the band equivalent width for the direct solar path from

level z^* to space, and $S_{0,r}$ is the solar flux averaged over band r. The value of $W_r(z^*, \mu_0)$ can be calculated using band models and tabulated spectroscopic data as described in Section 2.4. Allowance must be made for overlap between CO_2 and water-vapor bands and for the transition to the Voigt line shape in the upper stratosphere.

Although daily mean values of solar heating rate can be approximated by using a suitable daily mean value of μ_0 together with a heating-rate multiplier corresponding to the illuminated fraction of the day, calculations of high accuracy are carried out by numerical integration of the solar heating rate over the illuminated period.

2.7.3 Effects of Scattering

For the middle atmosphere, three scattering processes play a role: reflection and scattering from the underlying surface and troposphere, including clouds and aerosols; *in situ* molecular scattering (Rayleigh scattering); and *in situ* scattering by aerosols, particularly volcanic aerosols. Of these, the first is by far the most important. It is relatively easy to incorporate in calculations, but because the heating rate between the tropopause and 30 km is very sensitive to this upwelling solar flux, it is also sensitive to the distribution of clouds and aerosols.

The method of Lacis and Hansen is illustrated in Fig. 2.29. The stratosphere is divided into layers, and the solar heating is calculated by taking the difference between the direct solar radiation incident at the top of each layer and that emergent at the bottom of the layer, and adding the difference between the upwelling reflected solar flux incident at the bottom and emergent at the top. The solar flux at any interface depends on the total ozone amount along the path, as specified by the algebraic approximations derived by Lacis and Hansen. For the direct solar flux, the total ozone amount is the product of the vertical ozone column above the interface and the effective zenith angle, with the latter corrected appropriately for sphericity. The total ozone amount for upwelling radiation is the sum of two components, that due to the path for direct solar radiation reaching the underlying surface (clouds or ground) and that due to the diffusely reflected path from the surface to the interface. For the latter, Lacis and Hansen use an effective "diffuse flux approximation" factor 1.9. The upwelling flux is proportional to the reflectivity of the underlying surface, whose prescription depends on cloud cover. For clear conditions, the reflectivity is assumed to be the average over all reflection angles of the reflectivity of a surface of known albedo overlain by a Rayleigh scattering atmosphere. For cloudy conditions, the reflectivity is that of a diffusely reflecting cloud alone, and is assumed to depend on the optical depth of the cloud in the visible.

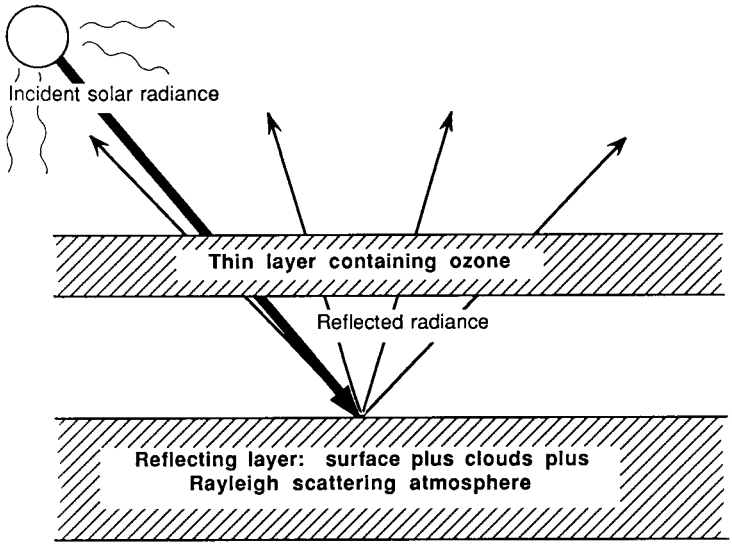

Fig. 2.29. Illustration of the Lacis and Hansen (1974) scheme for calculating ozone absorption. Solar energy deposited in the thin sublayer of the ozone layer is calculated by differencing the incident direct solar flux between the bottom and top of the layer, and differencing the upwelling diffuse flux between the top and bottom of the layer. The upwelling flux is assumed to come from an underlying reflecting layer whose albedo depends on surface properties, solar zenith angle, and the occurrence and properties of clouds.

This method provides an efficient and reasonably accurate calculation of ozone heating rate, accounting for upwelling solar radiation in the stratosphere. It does not account for scattering in the stratosphere or the interaction between scattering and absorption by ozone in the troposphere. As an alternative to the use of prescribed underlying surface and atmosphere reflectivities, Earth's reflectivity as measured by satellites can be used. The reflectivity seen by a satellite at wavelengths longer than about 340 nm is almost the same as the reflectivity seen looking downward from the stratosphere.

Background aerosol concentrations are not large enough to have a signicant effect on the energy balance of the stratosphere, but the aerosol effect can be important following major eruptions such as that of El Chichon in 1982 (see Section 12.5.2). The volcanic aerosols consist mainly of small sulfuric acid particles (radius $\sim 1\ \mu m$) whose single scattering albedo is high, ~0.98–1.00. Because they absorb infrared radiation emitted by underlying ground or cloud, and because they increase the effective path of sunlight through the ozone layer, they tend to warm the lower stratospheric region in which they reside. If the volcanic cloud contains significant

numbers of relatively absorptive soil particles, direct absorption of sunlight also contributes to heating.

Polar stratospheric water ice clouds and noctilucent clouds forming in the upper mesosphere may also have a small influence on heating in the middle atmosphere. Polar stratospheric clouds occur frequently in the southern hemisphere winter polar vortex and more rarely in the northern hemisphere winter polar vortex in the 15- to 25-km layer. The influence of these clouds on the radiation budget has been studied by Pollack and McKay (1985), who showed it to be generally unimportant except possibly in the southern winter polar vortex. Noctilucent clouds occur during summer near the polar mesopause. Though of great interest as an indicator of water-vapor condensation in the upper mesosphere, these clouds probably have only a minor effect on the radiation balance. Not only are the clouds extremely thin, but at these altitudes gas-particle heat exchange is inefficient in much the same way that translation-to-vibration energy exchange in CO_2 is inefficient.

2.8 Radiative Equilibrium Temperature and Heating-Rate Distributions

In the preceding sections the components of the radiative energy balance of the middle atmosphere have been considered. In this section, we consider the contributions of these components to the net heating rate and the radiative equilibrium temperature distribution that these contributions would produce in the absence of dynamical processes.

2.8.1 Net Heating and Its Components

The earliest detailed calculation of net heating rate in the middle atmosphere was carried out by Murgatroyd and Goody (1957) and included absorption of solar radiation by O_2 and O_3 and emission and exchange of longwave radiation by CO_2 and O_3. A number of calculations have been carried out since the pioneering work of Murgatroyd and Goody and have refined but not greatly altered the original conclusions. Most of the middle atmosphere is quite close to radiative equilibrium, such that there is near cancellation between large heating and cooling terms. Except in the polar regions, net heating-rate magnitudes rarely exceed 2 K day^{-1}, but there is a strong net cooling (up to 10–15 K day^{-1}) in the winter polar region between the stratopause and mesopause, and somewhat weaker net heating (up to $\sim$5 K day^{-1}) in the summer polar lower mesosphere. These substantial

imbalances in polar regions exert a strong control on the seasonally varying temperatures and zonal winds.

A recent calculation by Kiehl and Solomon (1986) illustrates these points (Fig. 2.30). This calculation made use of detailed global distributions of temperature and O_3 concentration measured by an instrument on board a

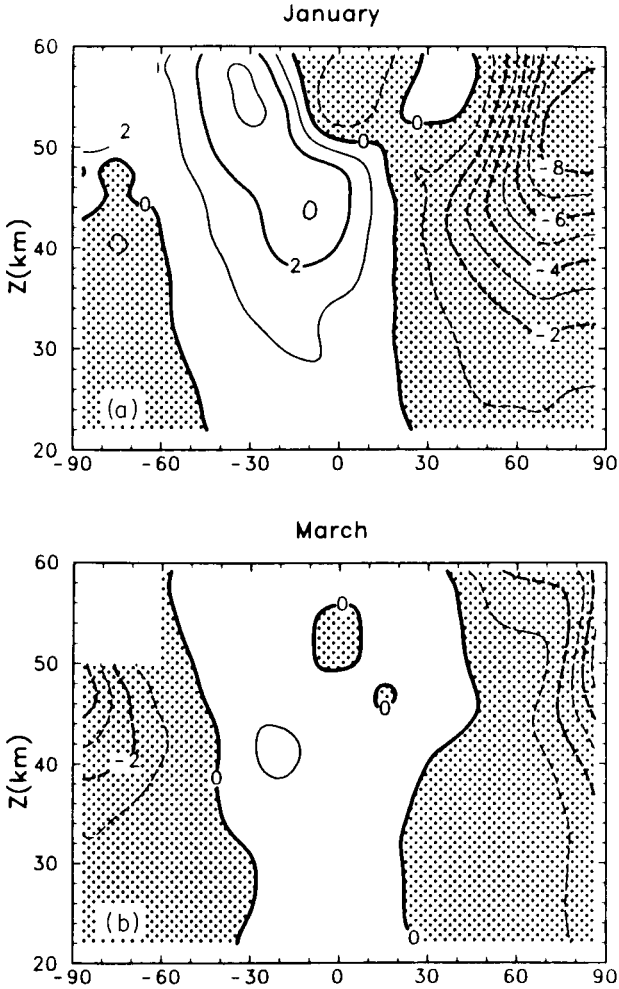

Fig. 2.30. Net heating rates (K day^{-1}) calculated for January and March. Temperatures and ozone concentrations used in the calculation were obtained from the Limb Infrared Monitor of the Stratosphere (LIMS) on the *Nimbus* 7 spacecraft during 1979. Due to lack of LIMS data, climatological temperatures and ozone concentrations were used south of 60°S, and there are no calculations above 50 km south of 60°S. [From Kiehl and Solomon (1986), with permission.]

polar orbiting satellite, the Limb Infrared Monitor of the Stratosphere (LIMS) instrument on board the *Nimbus* 7 satellite (see Section 2.9.3). Calculations were not made above 60 km or, in the south polar region, above 50 km due to lack of data. During January and May this calculation shows strong net cooling in the winter polar region, moderate net heating in the summer lower mesosphere, and very weak net heating elsewhere. During March there is strong cooling in both polar regions. There is considerable structure in the heating distribution above the stratopause in low latitudes, especially in January. This structure is real and is associated with the strong semiannual temperature cycle at low latitudes.

Figure 2.31 shows long-wavelength contributions to the balance by CO_2, O_3, and H_2O during January 1979. The patterns of the three contributions are similar, with maximum cooling near the stratopause, except that the 9.6-μm band of ozone contributes strong warming in the lower equatorial stratosphere. This feature is due to absorption of upwelling long-wavelength radiation, and it is sensitive to the distribution of tropospheric cloudiness. Water vapor and O_3 make negligible contributions to long-wavelength cooling above 60 km, and the upward extension of the CO_2 long-wavelength cooling into the upper mesosphere according to Dickinson is shown in Fig. 2.25. Note the good agreement between the calculations of Dickinson and Kiehl and Solomon in the region of overlap, despite the use of different temperature data sets.

Heating due to absorption of solar radiation by O_3, NO_2, and O_2 calculated by Kiehl and Solomon is shown in Fig. 2.32. In the region shown, O_2 and NO_2 heating rates are negligible but O_2 heating becomes important in the upper mesosphere due to strong heating in the Schumann–Runge bands. Figure 2.33 shows heating rates from London that extend the heating due to absorption of solar radiation by O_3 and O_2 above the mesopause. Absorption by O_2 is responsible for the strong high level heating maximum. Note, however, that London's heating rates are significantly greater than those calculated by Kiehl and Solomon in the region of overlap.

Experimental verification of the heating rates shown in Figs. 2.25 and 2.29–2.32 is not currently feasible because the flux divergences are so small. However, an indirect check of the validity of these calculations is possible. In the stratosphere and lower mesosphere, dynamical contributions to global mean heating at any level are small, so that global mean net radiative heating should be small throughout this region. In the middle and upper mesosphere, dynamical contributions to global mean net heating may be larger, but a small value of calculated global mean net radiative heating should still provide a rough check on calculations. Table 2.2 gives global mean net heating rates at various levels from the calculations of Kiehl and Solomon and Dickinson.

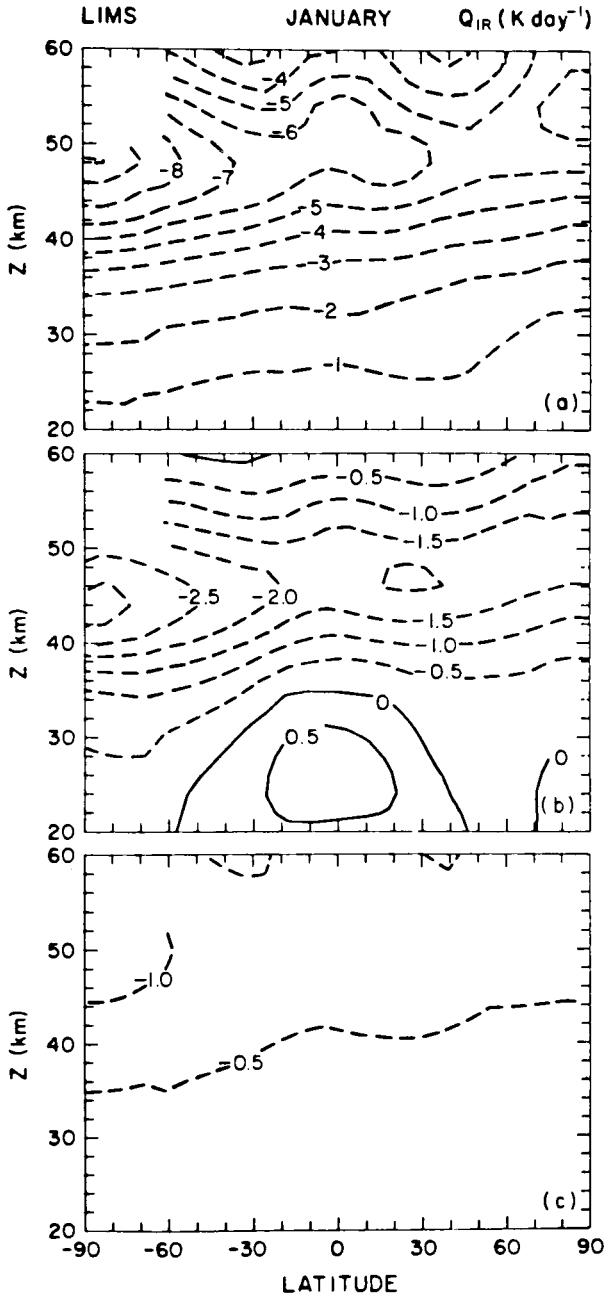

Fig. 2.31. Contributions of (a) CO_2, (b) O_3, and (c) H_2O to the total long-wave cooling during January 1979. [From Kiehl and Solomon (1986), with permission.]

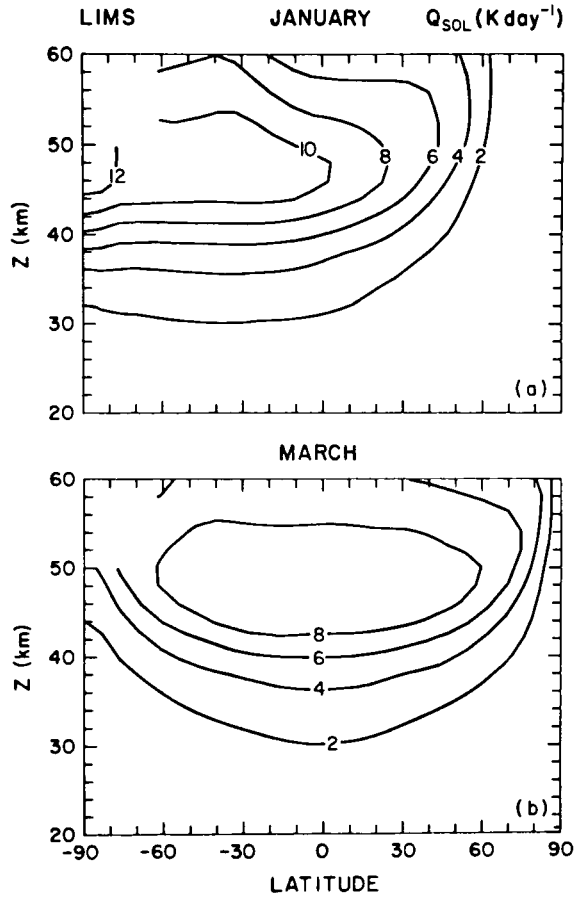

Fig. 2.32. Contributions of O_3, O_2, and NO_2 to heating rate during January and March 1979. [From Kiehl and Solomon (1986), with permission.]

The small values of calculated global mean net heating in Table 2.2 support the validity of the components of the calculations. The discrepancy in the lower mesosphere in the calculation of Kiehl and Solomon (1986) may be due largely to errors in the input ozone and temperature data. Solomon *et al.* (1986) have shown that the LIMS ozone measurements may be in error in this region for the following reason. Energy of solar ultraviolet radiation used to dissociate O_3 will be released when O_3 reforms during recombination. A fraction of this energy will appear as vibrational excitation of O_3, and some will cascade from high vibrational levels into the upper levels of transitions in the 9.6-μm spectral region. The resulting enhanced

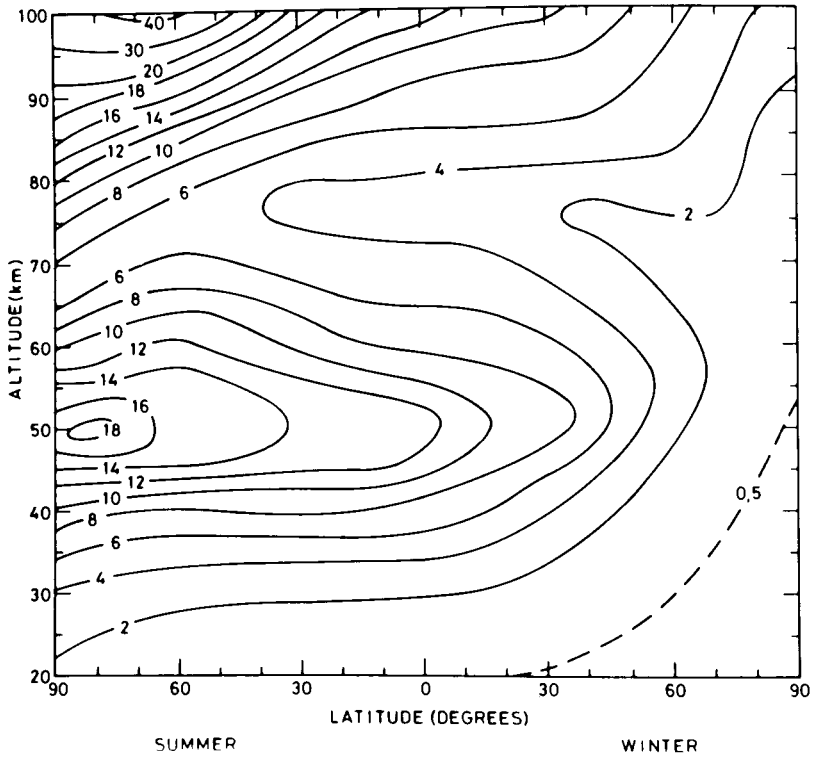

Fig. 2.33. Solar absorption by O_3, O_2, NO_2, and CO_2 during summer and winter, from London (1980). Differences between these values and those in Fig. 2.32 are largely due to differences in the ozone distributions used in the calculations. [From London (1980), with permission.]

Table 2.2

Calculated Globally Averaged Net Heating Rate

Altitude (km)	Net heating (K/day)[a]	Altitude (km)	Net heating (K/day)[b]
65	+0.2	25	−0.3
70	+0.8	30	−0.6
75	+0.6	35	−0.7
80	+0.7	40	−0.9
85	+1.7	45	−0.6
90	+4.7	50	−0.7
95	+2.4	55	+0.3
100	+1.5	60	+1.4

[a] Dickinson (1984).
[b] January mean, Kiehl and Solomon (1986).

9.6-μm band radiation would have been interpreted as a spurious O_3 excess in the analysis of the LIMS measurements.

2.8.2 *Radiative Equilibrium*

The radiative equilibrium temperature distribution is of interest as an indicator of the amount of temperature change that must be effected by the circulation. It can be calculated from

$$\frac{\partial T}{\partial t} = \frac{1}{\rho c_p}\left(\sum h_{r,ir} + \sum h_{r,uvv}\right), \tag{2.8.1}$$

where $\sum_r h_{r,ir}$ and $\sum_r h_{r,uvv}$ are the volume heating-rate contributions due to infrared and ultraviolet-plus-visible bands, respectively. Equation (2.8.1) is integrated from arbitrary initial conditions until a steady state is achieved.

Figure 2.34 shows the results of such a calculation. In the tropics and subtropics the radiative equilibrium temperature distribution is close to that observed. At high latitudes, particularly in the winter hemisphere, radiative equilibrium temperatures are far from observed temperatures. In the winter polar cap region, only infrared radiation transferred from the troposphere maintains nonzero temperatures. In radiative equilibrium, temperature decreases continuously from the summer to winter pole at all levels, in marked contrast to the observed temperature gradients in the upper mesosphere and lower stratosphere. Notice that this temperature distribution is very similar to that obtained from the time-marched radiative calculation shown in Fig. 1.2.

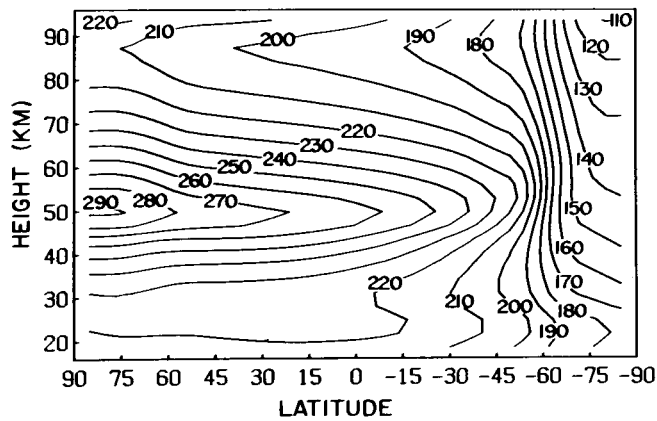

Fig. 2.34. Radiative equilibrium temperature distribution for northern (left) summer solstice. [From Wehrbein and Leovy (1982), with permission.]

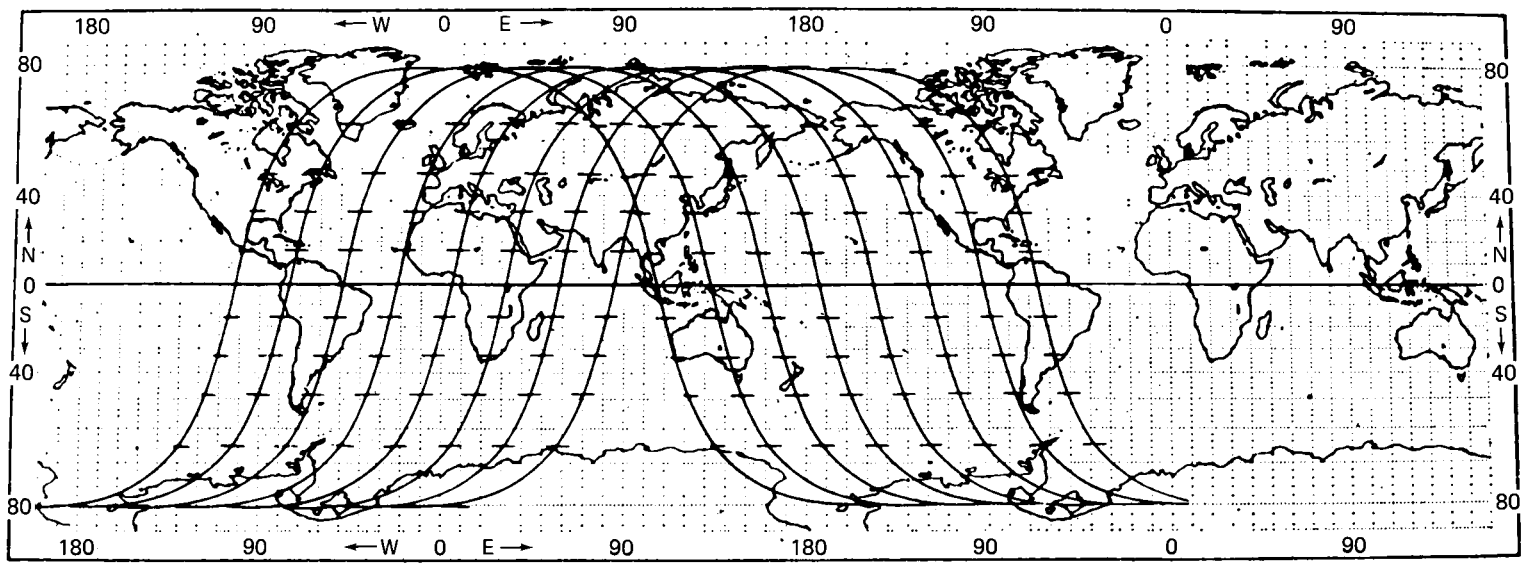

Fig. 2.35. Ground tracks for several orbits of a typical sun-synchronous polar orbiting satellite. [From Houghton *et al.* (1984), with permission.]

2.9 Remote Sounding

Until relatively recently, our knowledge of the distributions of temperature, winds, and such important trace gases as ozone and water vapor was limited to data from the worldwide radiosonde network, extending no higher than about 30 km, from a limited number of rocket profiles, and from some balloon and aircraft measurements obtained in connection with special experiments. None of these provided truly global coverage. This situation underwent a radical change beginning in the late 1960s with the advent of satellites carrying sensors capable of sounding the middle atmosphere. Examples of temperature and constituent distributions derived from satellite sounding are shown throughout this book.

The most useful satellite data sets for the middle atmosphere have so far been generated by polar orbiting satellites in the *Nimbus*, *NOAA*, and *Explorer* series. These satellites operate in sun-synchronous circular orbits near an altitude of 1000 km. The characteristic period of these orbits is slightly more than 100 min, so that there are typically 13–14 orbits per day. Because the earth is spinning beneath the satellite orbit, the subsatellite track slips westward by about 30° longitude from one orbit to the next. Sun-synchronous orbits maintain a constant angle between the earth–sun line and the line joining the earth's center and the satellite at the point where the satellite orbit crosses the ecliptic plane.

The satellite orbit slowly precesses to maintain constant-local-time satellite crossings of each latitude. The precession rate is accomplished by inclining the satellite orbit about 7° from the earth's polar axis. The lowest-order non-spherically symmetric component of the earth's gravity field provides the torque necessary to maintain the proper precession rate. The satellite orbit crosses each latitude circle twice each orbit, once ascending in latitude and once descending in latitude. Because the orbital period is not ordinarily commensurate with the earth's rotation period, orbits on successive days do not overlay. Instead, the spaces between adjacent orbital ground tracks on a given day are gradually filled in on succeeding days. A typical segment of the subspacecraft track of a sun-synchronous satellite is shown in Fig. 2.35.

A brief discussion of the use of radiance data acquired by satellites to infer properties of the middle atmosphere is given in this section.

2.9.1 Nadir Sounding of Temperature

The spectral distribution of upwelling radiance contains information about the vertical distribution of temperature and gaseous constituent concentrations. Since atmospheric opacity varies with wavelength and the depth

from which emergent radiation is emitted varies with opacity, different depths in the atmosphere are sensed by measurements at different wavelengths.

The upwelling radiance L_r in spectral band r sensed on a nadir viewing satellite is given by

$$L_r = \int_{0_-}^{\infty} \int_{\Delta\nu_r} \hat{I}(\nu) B_\nu(z) \frac{dT_\nu(z,\infty)}{dz}\, d\nu\, dz$$

$$= \int_{0_-}^{\infty} B_r(z) w_r(z)\, dz \tag{2.9.1}$$

where

$$w_r(z) \equiv \int_{\Delta\nu_r} \hat{I}(\nu) \frac{dT_\nu(z,\infty)}{dz}\, d\nu,$$

and $\hat{I}_\nu$ is the instrument spectral response function, normalized such that

$$\int_{\Delta\nu_r} \hat{I}(\nu)\, d\nu = 1,$$

and the transmission function is for the vertical viewing path. The notation 0_- is used to denote inclusion of the lower boundary in the integration. The quantity $w_r(z)$, called the "weighting function," determines the contribution of different atmospheric levels to L_r.

In order to examine the properties of w_r, consider a hypothetical instrument capable of sensing monochromatic radiance at frequency ν that is used to measure radiance emitted by a uniformly mixed absorbing gas with basic absorber density (scaled to reference temperature T_s) $\rho_{a0}(z) = \rho_{a0}(0)e^{-z/H} = \rho_{a0}(0)(p/p_0)$ and a constant absorption coefficient k_ν. The transmission function is

$$T_\nu(z,\infty) = \exp[-k_\nu H \rho_{a0}(0)(p/p_0)],$$

where p_0 is the pressure at the level at which $\rho_{a0} = \rho_{a0}(0)$ (e.g., the ground), and

$$w_r(z) = \frac{dT_\nu(z,\infty)}{dz} = -\frac{p}{H}\frac{dT_\nu}{dp}$$

$$= k_\nu \rho_{a0}(0)(p/p_0) \exp[-k_\nu H \rho_{a0}(0)(p/p_0)]. \tag{2.9.2}$$

This function has the pressure dependence of the Chapman layer structure for normal incidence radiance. Like the Chapman layer, it has a single maximum where the optical depth, $\tau_\nu = k_\nu H \rho_{a0}(z)$, is equal to 1. The upwelling radiance is determined primarily by the Planck function near this

level. Most importantly, this function has a characteristic width of about two scale heights, and this is the characteristic thickness of the region sensed at the instrument frequency ν.

It might seem that any real weighting function for a uniformly mixed gas would have a characteristic width of at least two scale heights, since in general w_r would be a superposition of monochromatic weighting functions, each corresponding to a different value of k_ν. This is not quite true, however, since k_ν is pressure-dependent. If k_ν corresponds to the wings of pressure broadened Lorentz lines,

$$k_\nu = S\alpha_L \pi^{-1}(\nu - \nu_0)^{-2} = k_{\nu 0}(p/p_0)$$

where

$$k_{\nu 0} \equiv S\alpha_{L0}\pi^{-1}(\nu - \nu_0)^{-2}$$

[using Eqs. (2.3.5) and (2.3.6) with p_s replaced by p_0], so that

$$w_r(z) = k_{\nu 0}\rho_{a0}(0)(p/p_0)^2 \exp[-\tfrac{1}{2}k_{\nu 0}H\rho_{a0}(0)(p/p_0)^2]. \qquad (2.9.3)$$

This weighting function has a shape similar to that of Eq. (2.9.2), but it is only half as broad. This is the narrowest physically realizable weighting function for nadir sounding of the Planck function.

An approximate representation of the vertical temperature profile can be obtained from multichannel satellite radiometer measurements in the 15-μm CO_2 band. The set of equations, one for each channel in the form of Eqs. (2.9.1), can be inverted to obtain a set of temperatures defining the approximate profile. The large width of the weighting functions severely limits the vertical resolution of these temperature profiles. In principle, resolution might be increased by using measurements from a large number of channels with closely spaced weighting functions. However, when there is strong overlap between the weighting functions, inversion of radiances to yield temperatures is unstable in the presence of any instrumental noise. Small radiance errors in one channel will be compensated by magnified errors in the temperatures retrieved for levels corresponding to the centers of weighting functions for adjacent overlapping channels. These errors in turn will propagate still further from the initial level. For realistic instrumental noise levels, the best resolution that can be achieved is comparable to the vertical width of the weighting functions.

Three nadir-viewing satellite instruments that have provided useful data on stratospheric temperature distributions are the Satellite Infrared Spectrometer (SIRS), a grating spectrometer flown on the *Nimbus* 3 and 4 satellites during the early 1970s, the Infrared Interferometer Spectrometer (IRIS), a Michelson interferometer flown on *Nimbus* 3 and on the *Mariner*

9 and *Voyager* planetary missions, and the High Resolution Infrared Radiation Sounder (HIRS), a multichannel filter radiometer flown on the *Nimbus* 6 and *TIROS-N* satellites in the late 1970s. Similar instrumentation has been flown by the Soviet Union on the *Meteor* satellite series during the same period. All of the weighting functions for these instruments peak at or below the 10-mb level, so they provide useful temperature data only for the middle and lower stratosphere.

In order to reach higher levels with nadir-viewing thermal infrared sensors, the technique of correlation spectrometry has been used. The first correlation spectrometers flown on a satellite were the Selective Chopper Radiometers (SCR) flown on *Nimbus* 4 and 5, and these have provided useful data from 1970 to 1978. In this technique, radiance from the underlying atmosphere first passes through filters to isolate broad regions in the 15-μm band, and the beam is rapidly cycled by means of a chopper between a direct path and path through an absorption cell containing a fixed amount of CO_2. By subtracting the two signals for the same location, a viewing path passing through the CO_2 cell and a path avoiding the cell, it is possible to isolate the component of terrestrial radiation emitted in the strong lines of the Q branch of the CO_2 fundamental. Since this radiation is emitted from relatively high altitude, the corresponding weighting function peaks at high altitude. By using a second cell with a larger CO_2 path, it is also possible to partially isolate the contribution to terrestrial radiance from the wings of the Lorentz lines in the P and R branches of the 15-μm fundamental. This produces a relatively narrow weighting function, approaching in width the theoretical limit discussed earlier in this section. Thus, the SCR instruments have produced a valuable data set covering the entire region from the ground to the stratopause.

A second type of gas-cell correlation spectrometer is the Pressure-Modulator Radiometer (PMR), first flown on *Nimbus* 6. A second-generation version of this instrument, the Stratospheric and Mesospheric Sounder (SAMS), was flown on *Nimbus* 7, providing data beginning in 1978. In the PMR technique, a CO_2 absorption cell is also used, but the pressure in the cell is varied by means of an oscillating piston. As the pressure in the cell varies, different 15-μm-band terrestrial radiance contributions are isolated. For example, at the lowest cell pressure (0.5 mb), the Doppler cores of the Q-branch lines of the fundamental are isolated. This gives a weighting function peaked in the upper mesosphere. Weighting functions for the SCR and PMR instruments are shown in Figs. 2.36 and 2.37. It can be seen that the entire region from tropopause to mesopause is covered by these instruments, but the coverage between 55 and 75 km in the mesosphere is sparse, so vertical resolution of temperature retrievals is poor in this region. In the case of SAMS, this situation was improved by operating the instrument in

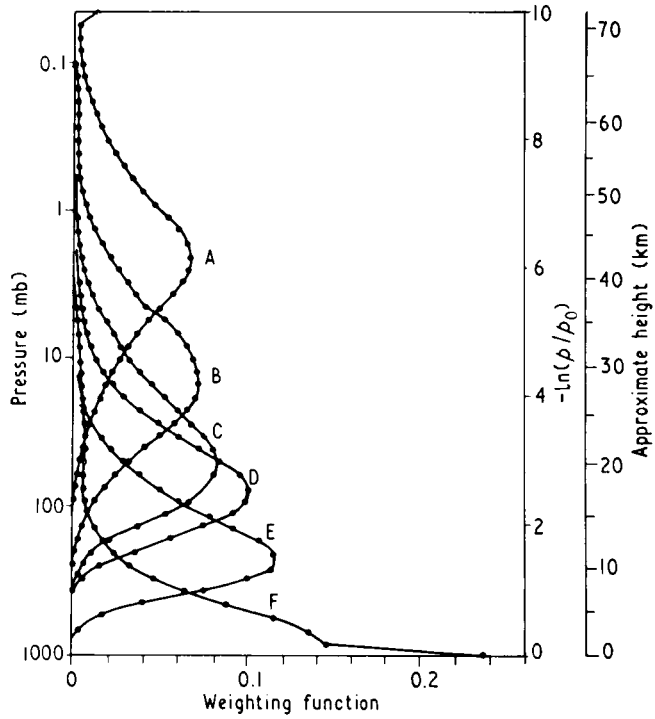

Fig. 2.36. Weighting functions for the Selective Chopper Radiometer on *Nimbus* 4. [From Abel *et al.* (1970), with permission.]

a limb-scanning mode (see Section 2.9.3). However, the main purpose of SAMS was to provide composition information. PMR cells are also used in the *TIROS-N* Operational Vertical Sounder (TOVS). Three cells, which have weighting functions that can be used to retrieve temperature from about 30 mb to 0.4 mb, comprise the Stratospheric Sounding Unit (SSU) of TOVS.

2.9.2 Geopotential and Wind

Temperatures retrieved from satellites are asynoptic: new observations are added continuously as the satellite moves in its orbit. However, a number of techniques are available to convert these evolving data sets into synoptic temperature distributions at specified times. A convenient practical method for doing this utilizes the Kalman filter as described by Rodgers (1976b).

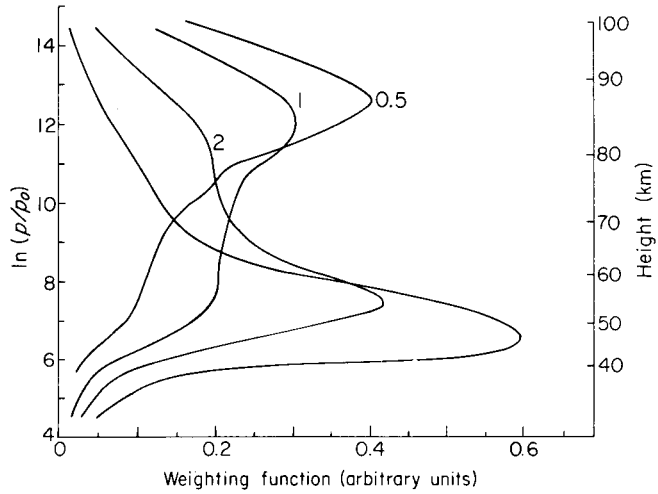

Fig. 2.37. Weighting functions for the Pressure Modulator Radiometer on *Nimbus* 5. [From Curtis *et al.* (1974), with permission.]

New observations of temperature along latitude circles are used to update the coefficients in a Fourier-series representation of temperature around the latitude circle in a quasi-continuous fashion. Inherent to this process is a smoothing operation of the Kalman filter, which can be tuned to match the precision of the observations, so that noise is suppressed.

Once the global distribution of temperature has been mapped, the distribution of geopotential on constant pressure surfaces can be obtained by integrating the hydrostatic equation from a base pressure level on which the geopotential is known from analysis of radiosonde observations. This base level is usually chosen to be 100 or 50 mb.

Instead of temperature, thickness of deep layers, typically spanning an order of magnitude range in pressure, can be retrieved. These retrievals can be carried out with good accuracy by linear regression, in which observed radiance is regressed against thickness derived from rocket measurements. Nadir satellite data with their broad weighting functions are well suited to this simple retrieval technique. The resulting geopotential surfaces have provided a sound basis for diagnoses of middle atmosphere circulation, although the vertical resolution is very limited.

Once the distribution of geopotential on middle atmosphere pressure surfaces has been deduced, geostrophic or gradient winds can be readily calculated, as can a variety of diagnostic quantities relevant to momentum and energy balances and wave propagation. Gradient or higher-order approximations to the rotational wind generally provide better estimates of

diagnostic quantities than geostrophic winds in the middle atmosphere (Elson, 1986). Despite the numerous approximations and limitations of the nadir-viewing satellite data, the time variations and relationships between these derived quantities have given a remarkably consistent picture of dynamical processes in the stratosphere in a number of studies, the results of which are discussed elsewhere in this volume.

In the future, we may look for direct satellite determinations of winds in the middle atmosphere based on advanced optical techniques. These will resolve the Doppler shifts of spectral lines resulting from winds averaged over domains whose dimensions are several hundred kilometers in the horizontal and a few kilometers in the vertical. An instrument capable of this type of measurement is to be flown on the Upper Atmosphere Research Satellite (*UARS*).

2.9.3 Limb Sounding of Temperature

As an alternative to nadir sounding, temperature profiles can be derived from a radiometer with a narrow field of view scanning vertically through the limb of the planet and measuring radiance in the 15-μm band (Fig. 2.38). This limb-sounding technique has several advantages over nadir sounding. The most important of these is that the weighting functions are determined primarily by the instrument field of view, and their width is therefore limited more by signal-to-noise considerations than by funda-

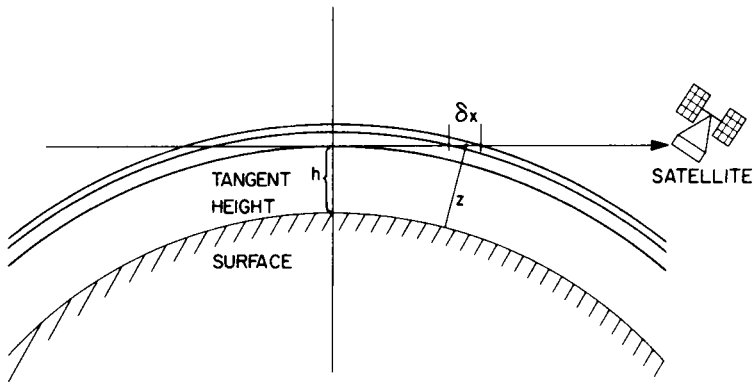

Fig. 2.38. Limb viewing geometry. The satellite instrument scans through the atmosphere on the limb at tangent height h. Radiance is received from elements of length δx at height z along the tangent path. [From Houghton *et al.* (1984), with permission.]

mental physical principles (Fig. 2.39). Since the instrument views a long atmospheric optical path (typically about 40 times the length of the nadir optical path to the altitude of the tangent point), and views it against the background of cold space, the sensitivity is high, and measurements can be easily extended well into the mesosphere. An additional advantage is that an "onion-peeling" technique, working from the top down, can be used to retrieve temperature, so that retrieval errors at one level do not propagate upward, although they do propagate downward.

The technique has some disadvantages. It is relatively sensitive to the presence of aerosols in the lower stratosphere, which can produce serious errors, and it cannot be consistently used to probe below the tropopause. It requires very precise knowledge of field of view and is sensitive to stray light. It also requires precise knowledge of spacecraft attitude and attitude change rates so that instrument pointing can be determined. If attitude change rates vary slowly compared with the limb-scan time, this rate can be nearly eliminated by combining data from adjacent upward and downward scans. If spacecraft attitude is not accurately known so that the absolute height scale on the limb is uncertain, a "two-color" technique, suggested by Gille and House (1971), can be used to locate a reference pressure level on each limb profile. Temperatures can then be associated with pressures at all other profile levels by working upward or downward from the reference

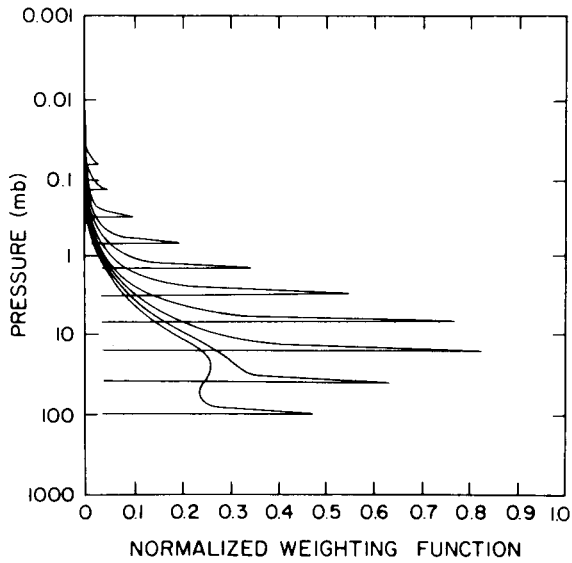

Fig. 2.39. Weighting functions for one of the 15-μm band channels of the Limb Infrared Monitor of the Stratosphere (LIMS). [From Bailey and Gille (1986), with permission.]

pressure level, using the hydrostatic equation and the retrieved temperatures. In this technique, simultaneous colocated observations in two 15-μm channels, one wide band and one narrow band, are used. Temperature–pressure profiles are retrieved using data from each channel starting from an assumed reference pressure at the same height on each profile. The two temperature–pressure retrievals will show systematic disagreement unless the assumed reference pressure corresponds to the actual pressure at that height. Thus, the true reference pressure can be deduced through an iterative correction procedure.

Thus far, limb-scanning instruments have viewed the horizon at a fixed angle with respect to the spacecraft track. As a result, sampling in longitude has been limited to the longitudinal sampling frequency of the spacecraft orbit. In contrast, nadir sampling has incorporated scanning across the spacecraft track with slightly off-nadir viewing, and this is done with the TOVS instrument to give complete longitudinal sampling at the resolution of the TOVS footprint.

The vertical resolution and sensitivity to high-altitude signals available in limb sounding are responsible for a considerable advance in quality of the global middle atmosphere data sets. In addition to SAMS, two limb-scanning radiometers have flown in *Nimbus* satellites, the Limb-Sounding Infrared Radiometer (LRIR) on *Nimbus* 6, and the Limb Infrared Monitor of the Stratosphere (LIMS) on *Nimbus* 7.

2.9.4 Sounding of Composition

A complete understanding of the chemistry of the middle atmosphere requires information on the distributions of nearly 50 minor gaseous species. The role played by some of these is discussed briefly in Chapter 10. Among the more important are O_3, O, H_2O, HNO_3, NO, NO_2, CH_4, CO, HCl, N_2O, $CFCl_3$, and CF_2Cl_2. Equation (2.9.1) can be inverted to retrieve $dT_\nu(z, \infty)/dz$, from which the vertical distribution of absorbing gas can be derived, provided that $B_\nu(z)$ is known independently and the atmosphere is in LTE. In practice this approach is very difficult from nadir-sounding observations, because of the low concentrations and resulting weak absorptions for most of the gases of interest. Even in principle, the information content of upwelling radiance for composition determination is strongly dependent on the vertical temperature profile. If the atmosphere is isothermal, no vertical structure information can be derived from low-resolution upwelling radiances.

A high degree of overlap between the spectral features of many of the gases of interest is another complication. As a result of these difficulties, useful retrievals of thermal radiance from nadir viewing have been restricted

to total column water vapor, total column O_3, and some constraints on the vertical profile of water vapor.

In contrast, the long viewing path, cold space background, and dependence of weighting functions on viewing geometry that characterize limb emission measurements have made it possible to infer near-global distributions of several important gases in the middle atmosphere. These include O_3 and H_2O (LRIR), O_3, H_2O, HNO_3, and NO_2 (LIMS), and CH_4, N_2O, CO, and NO (SAMS). Additional global measurements of NO_2, H_2O, and O_3 have been made with limb-viewing radiation sensors on the *Solar Mesosphere Explorer* (*SME*) satellite. Global distributions of several additional species are expected to be obtained from *UARS* limb measurements of thermal radiance.

Ozone is the most important variable species in the middle atmosphere, and its prominent ultraviolet spectrum lends itself to distribution determinations from measurements of backscattered solar radiance. Since the radiance source is Rayleigh-scattered sunlight for which the scattering cross section is strongly wavelength-dependent, the pressure range of the atmospheric layer from which the radiance is scattered depends strongly on wavelength. On the other hand, attenuation of the scattered radiation, and hence the radiance received at the satellite, depends on the amount of overlying O_3. As a consequence, the ultraviolet spectrum of the earth shows a broad deep minimum centered near 250 nm. The signature of this feature in backscattered solar irradiance has been widely used to retrieve O_3 vertical profiles. The most recent instruments to be used for this purpose are the Backscatter Ultraviolet Spectrometer (BUV) used on *Nimbus* 4 and on *Atmospheric Explorer* 5, and the Solar Backscatter Ultraviolet Spectrometer (SBUV) used on *Nimbus* 7 and on current operational satellites. Weighting functions for the SBUV instrument are shown in Fig. 2.40.

The total column amount of ozone has been measured globally since 1978 with the Total Ozone Mapping Spectrometer (TOMS) flown on several satellites. This technique uses differential absorption in reflected near-ultraviolet radiance to infer the total mass of ozone along the viewing path. The TOMS is a scanning instrument, so that measurements are available globally at high spatial resolution. Total ozone variations are dominated by variations in ozone amount in the lower stratosphere and by variations in tropopause height, so these data are especially useful for assessing the behavior of the tropopause at high spatial resolution and in regions that are poorly sampled by radiosondes.

Ozone vertical distribution below the level of the concentration maximum, about 25 km, is difficult to retrieve by either the ultraviolet backscatter technique or the thermal limb emission technique. Measurements of direct absorption of radiance along the path from the rising or setting sun (i.e.,

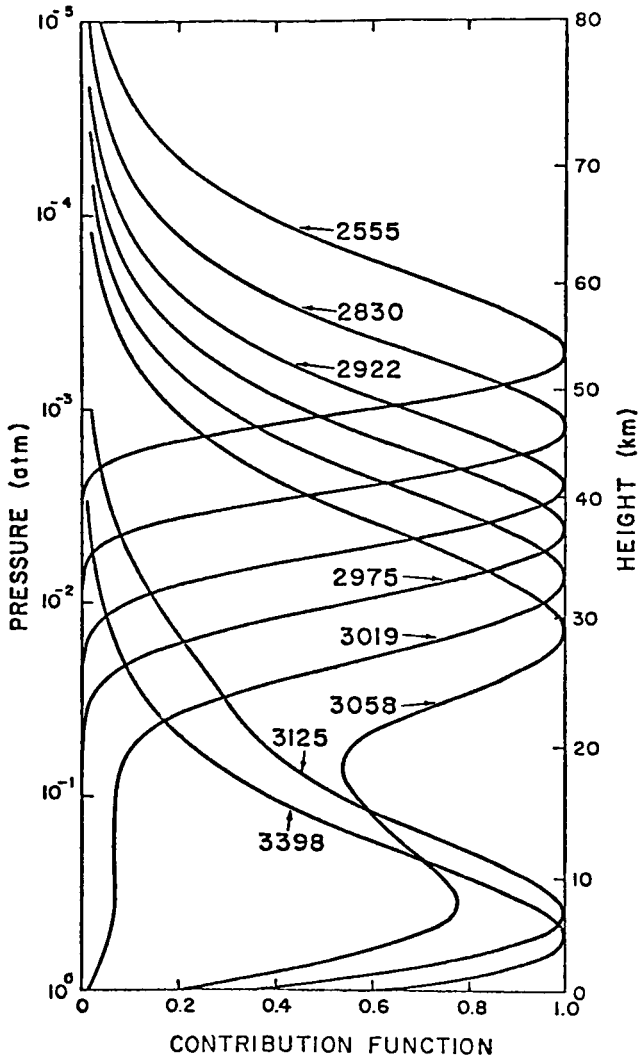

Fig. 2.40. Weighting functions for the Solar Backscatter Ultraviolet Spectrometer (SBUV) on the *Nimbus* 7 satellite. Note the absence of weighting functions peaked in the lower stratosphere. [From Yarger and Mateer (1976), with permission.]

measurements of radiance during *solar occultations*) can provide fairly precise estimates of the concentrations of many species over a broad altitude range, including O_3 in the difficult region between the tropopause and 25 km (Fig. 2.41). This *solar occultation* technique has also been used extensively to infer vertical distributions of stratospheric aerosols. The spatial distribu-

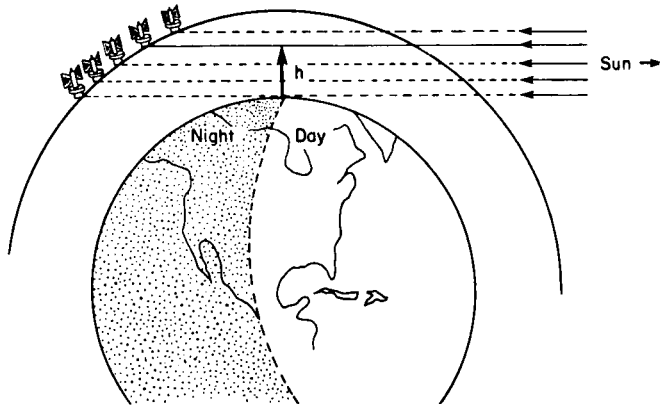

Fig. 2.41. Geometry for solar occultation measurements of atmospheric composition. [From McCormick *et al.* (1979), with permission.]

tion of solar occultation measurements is severely constrained by the sun-satellite viewing geometry. This limitation can be partially alleviated by using lunar or stellar occultations, but without the advantage of the very strong solar occultation signal.

Atmospheric sounding at microwave frequencies can also yield composition as well as temperature in the middle atmosphere. High-spectral-resolution measurements in the vicinity of an O_2 magnetic dipole transition centered near 60 GHz are widely used for temperature sounding and have provided useful information on global temperature variations in the lower stratosphere. Passive microwave sounding looking upward from the ground has yielded profiles of H_2O in the upper stratosphere and lower mesosphere and profiles of CO in the upper mesosphere. Additional species that are important for the chemistry of the middle atmosphere, including ClO, O_3, and H_2O_2, can be measured by microwave techniques. Future microwave measurements by *UARS* are expected to yield global distributions of these species.

References

2.1. An excellent overview of radiation in the middle atmosphere is given by Brasseur and Solomon (1984). Contributions of various gases to radiative heating and cooling are reviewed by London (1980). Applications of satellite remote sensing to the middle atmosphere are reviewed by Houghton *et al.* (1984).

2.2. Radiative transfer formalism is developed in the texts of Chandrasekhar (1950), Goody (1964), and Liou (1978). Chandrasekhar develops general methods for solving the radiative transfer equation in multiply scattering atmospheres; Goody emphasizes radiative transfer in atmospheres with absorption and emission by

molecular gases; Liou provides a clear development of the theory of scattering by spherical particles and presents a variety of methods for solving the radiative transfer equation. Spherical atmosphere effects and the Chapman function are discussed by Swider and Gardner (1957).

2.3. Physical processes responsible for molecular absorption, the structure of vibration–rotation bands and line shape are given in Goody (1964), and Brasseur and Solomon (1984). A good basic reference for this topic is Levine (1974). The semi-classical theory of transition strength is given in Houghton and Smith (1974). Molecular oxygen absorption is discussed by Frederick *et al.* (1983), and the Schumann–Runge bands in particular are discussed by Kockarts (1976), and by Allen and Frederick (1982). A recent tabulation of molecular oxygen absorption coefficients is given in WMO (1986). Infrared spectral data for CO_2, H_2O, O_3, and several other relevant gases are discussed by Drayson *et al.* (1984). Tabulations of positions, strengths, and temperature dependent line widths in the infrared and microwave regions are available in the AFGL Absorption Line Compilation as described by Rothman and Young (1981), and Rothman *et al.* (1983), and detailed discussion of spectroscopic data sets is given in Appendix B of WMO (1986).

2.4. Transmission functions are discussed in Goody (1964), Kondratyev (1969), Paltridge and Platt (1976), and Houghton (1977). The random models presented here were given by Goody (1952a), and Malkmus (1967). Whole band models are given by Ramanathan (1976), and Lacis and Hansen (1974). The Curtis–Godson approximation was suggested by Curtis (1952) and Godson (1953). Angular integration and errors of approximate approaches are discussed by Rodgers and Walshaw (1966). Approximations to the Voigt lines shape are given by Goldman (1968).

2.5. The exchange integral formulation of radiative transfer presented in this section was first given by Curtis (1956) and applied by Curtis and Goody (1956). The concept of the escape function was introduced by Dickinson (1972), and a simple parameterization of radiative exchange suitable for the stratosphere was suggested by Dickinson (1973). The spectral approach to radiative damping is discussed by Fels (1985).

2.6. The effects of departures from local thermodynamic equilibrium are quantitatively discussed by Goody (1964), Murgatroyd and Goody (1957), Kuhn and London (1969), Dickinson (1972), Kutepov and Shved (1978), Apruzese, Strobel, and Schoeberl (1984), and Fomichev *et al.* (1986). The most complete non-LTE model and calculation for the mesopause region published to date is that of Dickinson (1984).

2.7. The description of the vertical absorption profile for incident radiation originates with Chapman (1931). Deposition of solar radiation and its effects are discussed by Whitten and Poppoff (1971) and Brasseur and Solomon (1984). WMO (1986) is an excellent source of data on solar flux and its variability and on the ultraviolet absorption spectra of oxygen and ozone. Effects of scattered radiation in the stratosphere have been analyzed by Meier *et al.* (1982), Nicolet *et al.* (1982), and Herman and Mentall (1982). Approximate treatments of solar absorption have been given by Cogley and Borucki (1976) and Strobel (1978). Pollack and Ackerman (1983) have investigated the radiative effects of the El Chichon aerosol on the stratosphere.

2.8. Plass (1956a,b) carried out early studies of middle atmosphere cooling rates due to the 9.6-μm ozone and 15-μm CO_2 bands. Calculations of net heating rate for the middle atmosphere have been carried out by Murgatroyd and Goody (1957), Kuhn and London (1969), Wehrbein and Leovy (1982), Rosenfield *et al.* (1986), and Gille and Lyjak (1986). Drayson (1967) and Fomichev *et al.* (1986) have carried out a valuable assessment of the long wave contribution. Akmaev and Shved (1982) and Fomichev and Shved (1985) have provided accurate simplified treatments of long wave cooling by the CO_2 15-μm band and the O_3 9.6-μm band. Dopplick (1972, 1979) has presented a valuable calculation of net heating in the troposphere and stratosphere. Radiative equilibrium is discussed by Goody (1952), Leovy (1964a), and Apruzese *et al.* (1984).

2.9. Houghton *et al.* (1984) provide a valuable review of the principles and applications of remote sounding from satellites. The discussion of weighting functions in this section follows Houghton and Smith (1970). Hanel *et al.* (1971) discuss the IRIS instrument and display informative infrared spectra of Earth. The PMR is discussed by Taylor *et al.* (1972). Limb scanning infrared radiometer measurements of temperature, ozone, and water vapor are described in Gille and Russell (1984), Gille *et al.* (1984), Remsberg *et al.* (1984a,b), and Russell *et al.* (1984); SAMS measurements of CH_4 and N_2O are described by Jones and Pyle (1984). SBUV ozone measurements are described by McPeters *et al.* (1984), and TOMS measurements of total ozone are described by Bhartia *et al.* (1984). McCormick *et al.* (1984) present solar occultation measurement results for ozone, and McCormick *et al.* (1979) describe solar occultation measurements of stratospheric aerosol. The use of microwave radiances to infer temperature variations in the lower stratosphere has been described by Newman and Stanford (1985); microwave measurements of water vapor have been presented by Bevilacqua *et al.* (1983), and Waters *et al.* (1981) have discussed microwave measurements of ClO, O_3, and H_2O_2.